Artificial micro-nano structured materials based phononic crystals for Love waves manipulation

Yuxin Liu

N° d'ordre : 380

CENTRALE LILLE

THESE

Présentée en vue
d'obtenir le grade de

DOCTEUR

En

Spécialité : Micro et Nanotechnologies, Acoustique et Télécommunications

Par

Yuxin LIU

DOCTORAT DELIVRE PAR CENTRALE LILLE

Titre de la thèse :

Etude de cristaux phononiques à base des matériaux micro/nano structurés pour la manipulation des ondes de Love

Soutenue le 12 juillet 2019 devant le jury d'examen :

Président	Bahram DJAFARI-ROUHANI	professeur à l'Université de Lille
Rapporteur	Corinne DEJOUS	professeur à l'Université Bordeaux I
Rapporteur	Bernard BONELLO	directeur de recherche au CNRS
Examinateur	Bahram DJAFARI-ROUHANI	professeur à l'Université de Lille
Examinateur	Virginie BLONDEAU-PATISSIER	MCF HDR à L'Université de Franche-Comté
Examinateur	El Houssaine EL BOUDOUTI	professeur à l'Université Mohammed I
Invité	Vladimir PREOBRAZHENSKY	Professeur à l'Ecole Centrale de Lille
Directeur de thèse	Abdelkrim TALBI	Professeur à l'Ecole Centrale de Lille
Co-directeur de thèse	Philippe PERNOD	Professeur à l'Ecole Centrale de Lille
Co-directeur de thèse	Olivier BOU MATAR	Professeur à l'Ecole Centrale de Lille

Thèse préparée dans le Laboratoire International Associé LICS/LEMAC
Institut d'Electronique de Microélectronique et de Nanotechnologies
(IEMN, UMR CNRS 8520, France)
Ecole Doctorale SPI 072 (Lille I, Lille III, Artois, ULCO, UVHC, Centrale Lille)

Remerciements

Ce travail a été effectué pendant trois ans au sein du laboratoire international AIMAN-FILM de l'IEMN à Lille.

Je tiens à remercier en premier lieu M. Abdelkrim Talbi, mon directeur de thèse, pour avoir accepté d'encadrer ce travail de recherche. Je le remercie pour le temps qu'il m'a consacré, pour les connaissances scientifiques qu'il a partagées, pour tous les conseils prodigués tout au long de ce travail afin de diriger mes recherches. Je remercie également M. Philippe Pernod et M. Olivier Bou Matar, mes co-encadrants, pour m'avoir donné des conseils sur la présentation des travaux et sur la rédaction des articles.

Je veux également remercier vivement M. Bahram Djafari-Rouhani et M. El Houssaine El Boudouti qui m'ont accompagné dans ce travail de recherche. Je tiens à leur remercier particulièrement pour leur disponibilité, leurs compétences, leur confiance qu'ils m'ont témoignée tout au long des discussions et coopération fructueuses. Je les remercie tous les deux pour la patience et la compréhension dont ils ont fait preuve ensemble durant toutes les échanges.

Je remercie les membres du jury pour m'avoir fait l'honneur d'y participer : Mme. Corinne Dejous et M. Bonello Bernard pour avoir accepté de juger ce travail en tant que rapporteurs et Mme. Virginie Blondeau-Patissier pour l'intérêt qu'ils ont porté à ce travail en étant examinateur.

Je tiens à remercier tous les membres de l'équipe AIMAN-FILM qui m'ont soutenu tout au long de ce travail. Au cours de cette thèse, j'ai pu rencontrer de nombreuses personnes au laboratoire.

Enfin, je remercie ma famille et mes amis qui m'ont soutenu toutes ces années. Comme tous les membres ne connaissent pas le français, je leur remercie donc en anglais :

I thank my family and my friends who have supported me to study in France. I also thank the China Scholarship Council that funded me for my study and my life abroad.

Contents

Liste des tableaux

Table des figures

Résumé en français

Ce travail porte sur l'étude de l'ingénierie de la structure de bande ainsi que de l'interaction des résonateurs pour les ondes élastiques à base de matériaux micro et nano structurés déposés sur un substrat piézoélectrique recouvert d'une couche guidante. En particulier, nous nous intéressons à l'interaction des ondes acoustiques de surface polarisées transversalement (ondes de Love) avec des structures périodiques composées de micro-trous ou/et de micro-piliers disposés en réseau carré.

Introduction

Les cristaux phononiques (CPns) sont des matériaux synthétiques formés par des variations périodiques des propriétés acoustiques, comme l'élasticité et la masse. [50, 52]. Ils suscitent depuis une vingtaine d'années un intérêt de plus en plus croissant. Ces matériaux artificiels présentent des bandes interdites, c'est-à-dire des plages de longueur d'onde ou de fréquence dans lesquelles les ondes élastiques ne peuvent pas se propager à travers la structure. Ce qui est à l'origine de multiples applications pour contrôler la propagation des ondes.

Les bandes interdites des CPns sont généralement classées en deux types : l'un est dû à la diffraction de Bragg, l'autre à la résonance locale. Le mécanisme de Bragg existe dans les systèmes périodiques et repose sur l'interférence destructive des ondes diffusées par les inclusions. Pour la bande interdite de type résonance locale, ou bande interdite d'hybridation, qui découle du croisement évité de deux modes couplées (mode

de résonance propre d'un résonateur et mode qui se propage dans la structure) dans la bande de fréquences inférieure, la résonance d'un seul résonateur joue le rôle principal.

Les CPns ont été principalement étudié en intéragissant avec les ondes de volume, les ondes de Rayleigh, les ondes de Lamb et les ondes de Love. Cependant, les ondes de volume et les ondes de Rayleigh sont facilement diffusées. En plus, les dispositifs des ondes de volume à haute fréquence sont difficile à réaliser [98]. Les ondes de Lamb quant à lui se propagent dans une couche fine d'epaisseur de longueur d'onde ou sous-longueur d'onde. Ce qui rend ses dispositifs fragiles difficile à manipuler [154]. Les ondes de Love sont considérées comme une compromise entre les ondes de Rayleigh et les onde de Lamb. Ils sont confinées à la surface comme ils se propagent dans une fine couche guidante. Ses dispositifs sont solides parce que la couche guidante est déposée sur un substrat semi-unfini. En outre, les ondes de Love sont compatibles avec l'environnement liquide [15, 16], ce qui en fait un candidat idéal pour les applications de biocapteurs.

Ces dernières années, le contrôle des vibrations mécaniques en tant que élément constitutif de la recherche sur les effets liés aux quantiques a suscité un intérêt considérable [116, 136, 158, 161, 163, 164, 166–171]. Le contrôle cohérent des propriétés de vibration[166, 167], effets de couplage[160, 171, 172], dissipatif[173] et caractéristiques non linéaires[174] des résonateurs mécaniques donne lieu à une grande variété d'applications dans les capteurs[175–177] et traitement de signal[178–180]. Différents modes dans un seul résonateur mécanique peuvent être couplés en ajustant les paramètres[166, 174, 181, 182], alors que différents résonateurs mécaniques peuvent être couplés à travers divers milieux[159, 160, 169, 171, 183, 184] ou par interaction directe.[185, 186]. En acoustique, des résonateurs couplés ont été rapportés dans des systèmes tels que des cavités[171], guides d'ondes[169], cavités/guides d'ondes [116] ou résonateurs locaux[170, 187]. L'interaction entre différents résonateurs permet aux mécanismes correspondants d'être mis à l'échelle au réseau de résonateurs afin de gérer des systèmes avec une finesse supérieure [133, 136, 171, 180, 188, 189].

L'objectif de cette thèse est d'étudier numériquement le mécanisme d'interaction des ondes de Love avec les modes de résonances des microstructures sous forme de trous et/ou de plots déposés périodiquement à la surface d'un matériau piézoélectrique. Le but est de comprendre les méchanismes des bandes interdites, de concevoir et d'optimiser de nouveaux résonateurs à forte résonance, et d'étudier l'interaction entre différents résonateurs pour le développement des fonctions avancées de traitement du signal.

Interaction des ondes de Love avec cristaux phononiques parfaits

les modèles théoriques sont implémentés dans le logiciel COMSOL Multiphysics afin d'étudier les structures de bande et les spectres de transmission de différents CPns en interaction avec les ondes de Love. La profondeur d'énergie normalisée (PEN) est calculée pour sélectionner les ondes de surface, ainsi que le rapport de composante de déplacement transversal horizontal (TH) afin de distinguer les ondes de Love.

Nous avons d'abord étudié les structures de bandes pour les CPns à trous et/ou à Ni plots en réseau carré sur une couche guidante en SiO_2 construite sur un substrat de quartz coupe-90ST. Les ondes de Love se propagent suivant l'axe x (l'axe y du quartz coupe-ST). La surface est perpendiculaire à l'axe z. La constante du réseau pour les CPns à trous et/ou à plots est a=4μm, le rayon des trous (ou des plots) est r_h=0,2a (ou r_p), l'épaisseur de la couche guidante (= la profondeur des trous) est H=0,6a, la hauteur des plots est h.

Un example de diagrammes de bandes est montré sur la Fig 1 pour les réseaux (a) à trous et (b) à plots. Les paramètres géométriques pour les plots sont r_p=0.2a et h=0.6a. Les lignes noires pleines / en pointillés indiquent la vitesse des ondes TH dans le substrat / la couche guidante. Les couleurs rouge-jaune indiquent le rapport de composant TH. Les lignes grises sont les modes se propageant dans le volume. Un mode en rouge est un mode TH au surface. La zone bleue indique la bande interdite partielle ou absolue des modes de Love. On voit que le CPn à trous donne lieu à une

grande bande interdite partielle de Bragg suivant l'axe x. Le CPn à plots quant à lui est capable de générer des modes de résonances locaux au-dessous des fréquence d'un petite bande interdite partielle de Bragg. Grâce à la génération exclusive d'ondes TH dans notre structure (SiO2 / 90ST quartz) suivant la direction x, nous ne présentons à droite de chaque diagramme que les modes TH (rapport TH> 0,5) dans la région ΓX. Les déplacements, déformations des modes de surface ont été fournis et expliquées. Les polarisations correspondantes se sont révélées cohérentes avec les calculs. Ensuite, nous

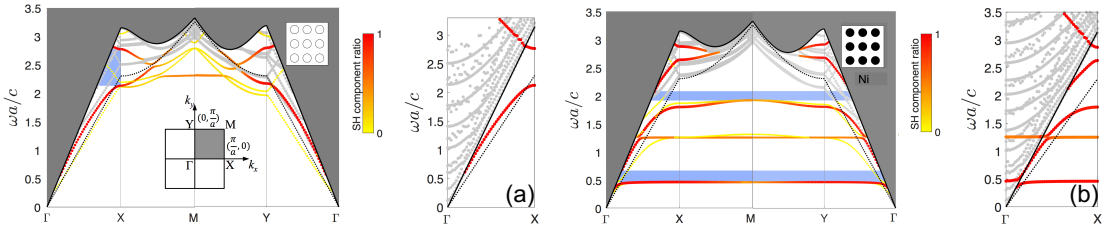

FIGURE 1 – Structures de bandes complètes au sein des réseaux carrés (a) à trous et (b) à plots. C est la vitesse des ondes TH se propageant suivant l'axe x dans le substrat. La structure de bande des modes TH dans la région ΓX sont affichées à droite de chaque diagramme.

avons proposé et étudié les influences des paramètres géometriques (le rayon du trou et plot, l'épaisseur de la couche guidante et la hauteur du plot) sur les bandes interdites. En comparant différents matériaux des plots (diamant, silicium et or), on a montré que plus la vitesse acoustique est faible, plus les fréquences propres des modes sont basses.

Et puis, pour comprendre comment le structure de bande se traduit sur une transmission, nous avons développé et implémenté un modèle sous COMSOL. Un exemple de résultat est illustré sur la Fig 2. Il présente la transmission des ondes de Love à travers le réseau à plots. On observe clairement que les bandes interdites (Bragg ou de résonances locaux) se traduisent par les intervals d'absorption sur la transmission.

Nous avons également mené une série de simulation en combinant et réglant les CPns à trous et à plots. nous avons démontré que les CPns mélangés ont les capacités d'élargir le bande interdite ou de générer un mode isolé dans la bande interdite.

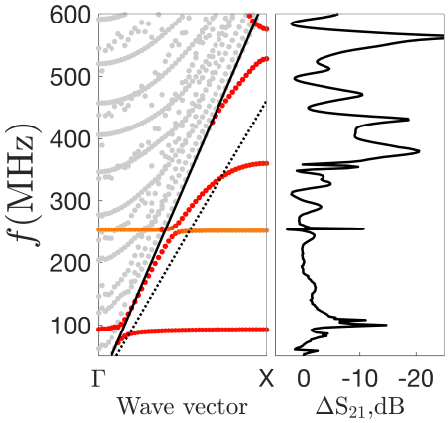

FIGURE 2 – (gauche) Structure de bande des modes TH pour le CPn à plots dans la direction ΓX. (droite) Spectre de transmission relative ΔS_{21} des ondes de Love se propageant suivant l'axe x à travers le CPn à plots. $r_p = 0,2a, h = 0,6a, H = 0,6a, a = 4\mu$m. Le nombre de plots suivant l'axe x est $N_{CPn} = 10$.

Résonateurs locaux de surface

L'interaction des résonateurs locaux (piliers) avec les ondes Love ont été étudiée pour la première fois sur les méta-surfaces à un ou deux lignes de piliers suivant l'axe y (perpendiculaires à la direction de propagation x). La périodicité suivant la direction y est a_p=2μm. La taille du plot est r_p=0,2a_p et h=0,6a_p. L'epaisseur de la couche guidante est H=2,4μm.

Premièrement, on a démontré que le mode de torsion intrinsèque des piliers est bien excité par les ondes de Love. Une ligne de piliers identiques peut provoquer une forte absorption de transmission dû à une interférence destructive.

Deuxièmement, l'analogue acoustique de Autler-Townes Splitting (ATS) et de la resonance Fabry-Perot (FP) des ondes de Love sont démontrés dans deux lignes de piliers identiques en faisant varier la distance entre les lignes de piliers. L'ATS apparaît lorsque la distance est inférieure à la demi-longueur d'onde et qu'un fort couplage est généré entre les lignes des piliers, ce qui provoque la division du creux de transmission induit par le mode de pilier en deux creux avec une fenêtre de transparence au milieu. La

résonance FP existe aux positions où la distance entre les lignes des piliers est un multiple de la demi-longueur d'onde. La proximité de la résonance FP avec le mode intrinsèque de pilier donne naissance aux modes de cavité avec amélioration de la transmission sur les deux bords du creux unique. Nous avons évité de confondre les résonances FP avec les modes de cavité en présentant les différentes variations de fréquence par rapport à la distance entre les piliers. Troisièmement, le rayon d'une ligne de pilier est modifié pour désaccorder la fréquence de résonance des piliers. Dans la région de couplage des piliers, l'effet de couplage décroît avec l'augmentation de la différence des rayons (see Fig 3(a) et (b)).Lorsque la distance entre les lignes des piliers est un multiple de la moitié de la longueur d'onde, la résonance FP ainsi que les résonances des deux piliers différents donnent lieu à la transparence induite acoustiquement (AIT), see Fig 3(c) et (f). Les phénomènes ATS et AIT sont ensuite ajustés respectivement avec les modèles de formule correspondants, montrant de bons accords. Les paramètres d'ajustement sont présentés comme fonctions du paramètre géométrique. Le critère d'information d'Akaike (AIC) est ensuite utilisé pour la première fois dans un système acoustique pour évaluer quantitativement la qualité des modèles d'ajustement, ce qui illustre le passage de l'ATS à l'AIT ainsi que la périodicité de l'AIT en augmentant la distance entre les lignes des piliers. Nous avons montré que La différenciation théorique et analytique de l'ATS et de l'AIT devrait être utilisée conjointement pour discriminer l'attribution du spectre observé à l'un ou l'autre des mécanismes physiques.

Ensuite, on a démontré que deux piliers différents qui s'alternent sur une même ligne soulèvent deux creux avec un pic au milieu. Le premier creux avec le pic donne lieu à une résonance Fano lorsque les deux piliers présentent un petit décalage géométrique et que le couplage entre les piliers est assez fort que les creux désaccordent avec les fréquences de mode de chaque pilier. Cette résonance peut être de plus en plus confineée en réduisant la périodicité le long de la direction y, avec un facteur de qualité allant jusqu'à $3{,}33\times10^5$. Les phénomènes ci-dessus peuvent également être obtenus en désaccordant

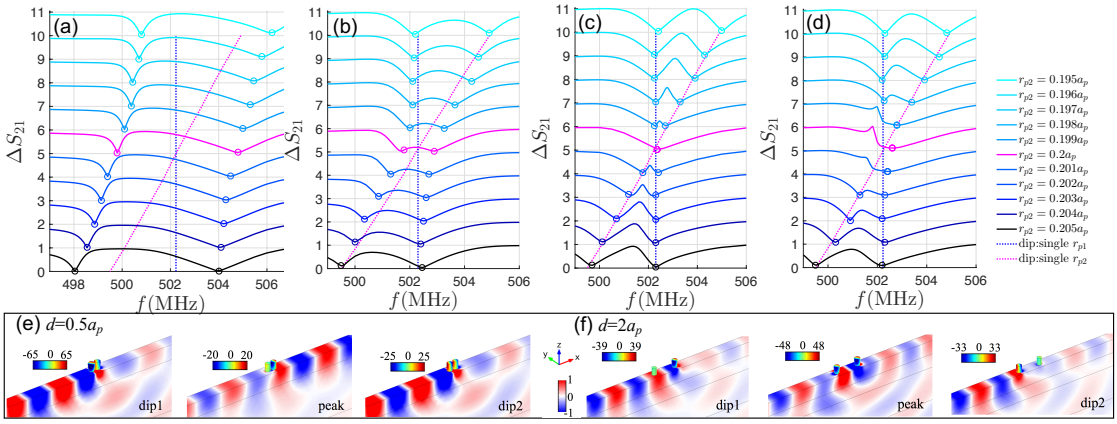

FIGURE 3 – Spectre de transmission relative des ondes de Love avec d= (a)0,5a_p, (b)a_p, (c)2a_p, (d)2,4a_p lors du changement progressif du rayon du deuxième pilier r_{p2} de 0.195a_p à 0.205a_p. Le rayon du premier pilier est r_{p1}=0.2a_p, a_p = 2μm. (e) Champs de déplacement u_y aux creux et au pic pour l'ATS avec d=0,5a_p et r_{p1}=r_{p2}=0,2a_p. (f) est les mêmes que (e) mais pour l'AIT avec d=2a_p, r_{p1}=0,2a_p et r_{p2}=0,202a_p. La résonance FP tombe à d=2a_p.

la hauteur des piliers.

Modes de defaut couplés avec les résonateurs locaux

Les modes de cavité dans la bande interdite pour les ondes de Love sont démontrés pour la première fois en supprimant des lignes de trous dans la couche guidante du CPn à trous. Les pics de transmission des modes de cavité dans la bande interdite originale du CPn à tous sont attribués à l'apparition de nouveaux modes plats dans la structure de bande, see Fig 4(a). Les spectres de transmission sont en accord avec les prévisions de structure de bande. On a montré que le rayon des trous a un effet important sur le confinement des ondes et les performances de transmission. Les fréquences de résonance des modes de cavité sont liées à la largeur de cavité. Les modes de cavité symétriques et asymétriques apparaissent alternativement avec l'augmentation de la largeur de la cavité. Le facteur de qualité peut être amélioré en augmentant la taille du cristal. Toutefois, la transmission sera réduite en raison d'une perte d'énergie. Des modes de cavité ont également été démontrés dans des CPns à piliers et mélangés.

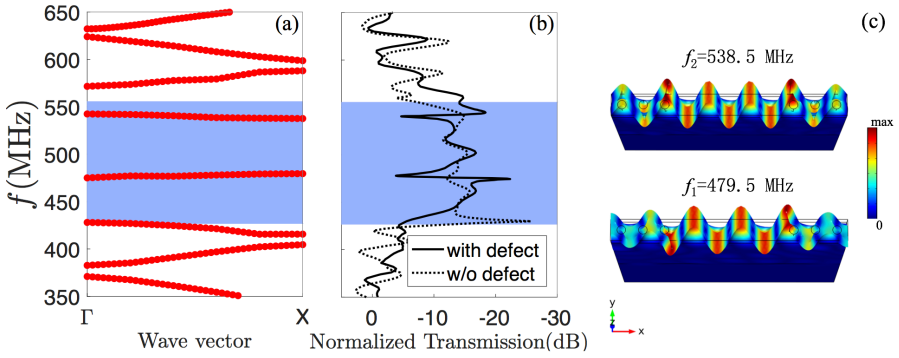

FIGURE 4 – (a) Structure de bande des modes de Love pour le CPn à trous contenant une cavité dans la direction ΓX. La région bleu est la bande interdite originale du CPn à trous. La largeur de cavité est W=5a. (b) Spectre de transmission relative des ondes de Love avec et sans défaut (cavité). Le nombre de trous à chaque côté est N_{CPn}=4. (c) Champs de déplacement totals et déformations dans la supercellule pour les deux modes de cavité. Conditions périodiques sont appliqués suivant la direction y. r_h=0,2a, H=0,6a, a=4μm.

Une cavité de taille optimale est ensuite choisie pour coïncider avec la fréquence du mode de torsion du pilier. La cavité contenant des piliers pour les ondes de Love est démontrée pour la première fois en introduisant les piliers dans la cavité. En divisant la cavité en deux parties (N / M) en fonction de l'amplitude du déplacement, nous avons systématiquement étudié l'effet de couplage entre le pilier et le mode cavité. Le pilier en position N (au nœud) peut être excité et est couplé au mode cavité, amenant le pic du mode cavité à se scinder en deux pics. Tandis que le pilier en position M (anti-nœud) n'est pas couplé au mode cavité mais peut encore donner lieu à un pic en émettant une onde supplémentaire. L'effet de division des pics est expliqué comme un croisement évité lorsque le mode de la cavité est couplé au mode intrinsèque du pilier, see Fig 5.

L'efficacité du mode cavité peut être améliorée lorsqu'il est couplé au mode pilier. L'augmentation du nombre de piliers permet d'améliorer les performances de résonance du pilier et l'efficacité de la cavité, see Fig 6. Le pic de transmission le plus confiné créé à la fréquence du mode cavité d'origine présente un facteur de qualité 240 fois supérieur. Par rapport à l'augmentation de la taille du cristal de cavité nue (sans pilier), la cavité

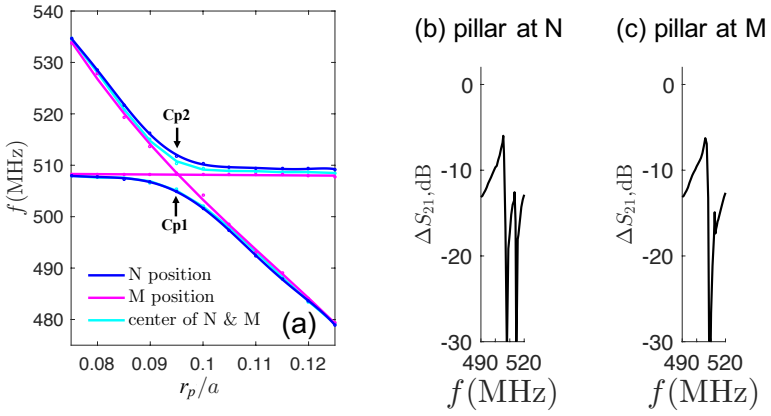

FIGURE 5 – (a) Fréquences propres des modes de Love comme une function du rayon du pilier losque un pilier est mis au différentes positions de la cavité. N (M) position indique que le pilier est au nœud (anti-nœud) du mode de cavité. La largeur de cavité est W=4,5a. (b) et (c) sont les spectres de transmission des modes cavité lorsqu'un pilier de rayon r_p=0,1a est mis respectivement au nœud et anti-nœud de la cavité. r_h=0,2a, H=0.6a, h=0.3a, a=4μm.

couplée fournit une méthode pour améliorer de manière significative le facteur Q tout en maintenant un niveau de transmission élevé.

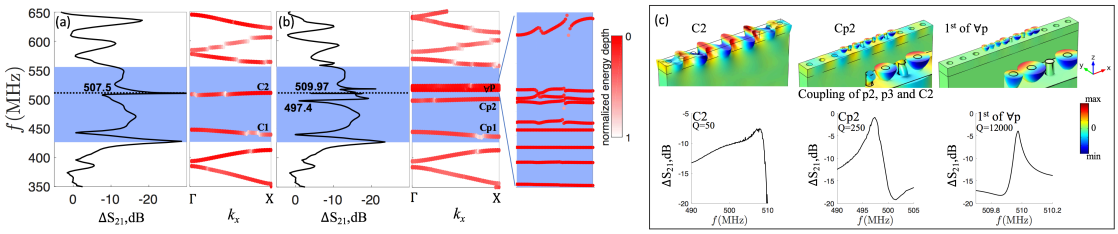

FIGURE 6 – Spectre de transmission et structures de bande des modes TH de surface pour les CPn à trous contenant la cavité (a) sans et (b) avec piliers. Les zones bleues sont la région de la bande interdite d'origine du CPn à trous. La ligne pointillée représente la fréquence du mode de torsion des piliers. La périodicité des piliers suivant la direction x est a_p. (c) Champs de déplacement u_y et des pics de transmission élargis de modes C2 (mode cavité nue), Cp2 (mode de cavité couplé aux piliers) et 1^{er} mode des piliers. W=4,5a, r_h=0,2a, r_p=0.2a_p, H=0.6a, h=0.6a_p, a=4μm, a_p=2μm.

Conclusion

Dans ce travail, l'étude des matériaux micro et nano structurés pour l'ingénierie des bandes interdites acoustiques dans les dispositifs électro-acoustiques a été présentée, en particulier pour l'étude des CPns 2D à trous et / ou à Ni piliers interagissant avec les ondes de Love et de l'interaction entre les différents résonateurs.

En étudiant les CPns infinis à trous et à piliers, on a compris les méchanismes des bandes interdites et l'influence des paramètres géométriques et élastiques sur celles-ci. En combinant et en ajustant la position et la taille des trous et des piliers, nous avons étudié le couplage entre la bande interdite de Bragg (du CPn à trous) et la résonance locale (du CPn à piliers).

On a ensuite étudié l'interaction entre les ondes de Love et les méta-surfaces à piliers. Les couplages entre les piliers identiques et différents ont donné lieu aux phénomènes divers comme ATS, résonance FP, modes de cavité, AIT et résonance Fano. Les distinctions théorique et analytique de l'ATS et l'AIT se sont révélées méthodologiquement complémentaires.

Par la suite, on a créé un défaut linéaire dans le CPn à trous et a observé des modes de défaut (cavité). En insérant les piliers dans la cavité, on a étudié l'interaction entre les modes cavité et la résonance local d'un seul pilier ou des piliers collectifs, ce qui donne lieu à un effet de division des pics et peut considérablement améliorer le facteur de qualité des modes cavité sans augmenter la taille des cristaux.

Les résultats présentés dans cette étude pourraient être utilisés pour des applications acoustiques potentielles telles que le traitement du signal, le contrôle des ondes, les méta-matériaux et les biocapteurs.

Introduction

Phononic crystals

phononic crystals (PnCs) have received increasing attention in the last two decades and are widely investigated for their potential applications in various areas, including RF communications[1–7], acoustic isolators[8–13], sensors[14–19], thermoelectric materials[20–23] and meta-materials[24–32].

The PnCs are synthetic materials formed by periodic variations of acoustic properties, such as elasticity and density. They are used primarily to control the acoustic waves propagation. From the point of view of the wave propagation, the wavelengths that can propagate in the structure are called modes. The groups of modes are the passing bands. The frequency ranges where the waves can not propagate are the band gaps. The dispersion diagram can be used to predict passing bands, band gaps, negative group velocity branches, flat branches, and so on. The concept of band gap is the key element for the manipulation and control of wave propagation. PnCs is an elastic analog of the photonic crystals (PtCs) that interact with electromagnetic waves, as well as the atomic lattices that interact with the electronic waves. The periodic dielectric & magnetic constants/atoms are replaced by the periodic elastic parameters & density, and the generated photonic/energy band gaps are replaced by acoustic band gaps.

Band gaps of PnCs are generally classified into two types : One is due to Bragg

diffraction, the other is due to local resonance. The Bragg mechanism exists in the periodic systems and is based on the destructive interference of the scattered waves by the inclusions. The central frequency of the first Bragg band gap is anti-proportional with the lattice constant, with the wavelength of the same order of magnitude as the lattice constant. The use of periodic structures for the manipulation of elastic waves in piezoelectric materials was proposed in 1965 by White and Voltmer by the invention of the concept of inter-digital transducers (IDTs). These metal structures deposited on the surface of a piezoelectric material that can excite, detect waves and also implement advanced functions of signal processing (filtering, compression, delay lines for color TV receivers). By analogy with optics and crystallography, these structures were used to make Bragg reflectors and other structures in the fields of electronics, signal processing and telecoms. At the beginning of the 90s, physicists introduced phononic crystal terminology by analogy with optics and electronics to design a periodic medium, which result in the passage of nano-metric, micro-metric, milli-metric or even metric wavelengths. The designs were then extended to all materials with inhomogeneity or contrast of physical properties. The local resonance type band gap, or hybridization band gap, comes from the avoided crossing of two coupled bands in the lower frequency range. This band gap depends mainly on the intrinsic vibration of the individual particle, but nearly not on the periodicity of PnC. That is, the hybridization gaps persist even with structural disorder. The central frequency of the hybridization band is anti-proportional with the individual particle size, which is at a scale smaller than the wavelength. In 2000, local resonant PnC was first demonstrated by Liu et al. They showed that their PnC behaves as a medium with a negative effective elastic constant, which integrate into the category of acoustic meta-materials.

Since the 2000s, research has focused on engineering the physical properties of phononic crystals and meta-materials. The scientists have shown that band gaps are determined by several factors, such as the physical properties of each constituent of the

artificial material, the geometric parameters, and the symmetry of the lattice [33–49]. In general, for a given lattice constant, a wider band gap means that PnC devices can be made more compact. In the case of meta-materials, a larger ratio between the wavelength of interest and the characteristic dimension of the unit cell implies a lightweight artificial material. As a result, many studies have been conducted to achieve these goals and can be summarized in three different strategies : the inherent Bragg scattering in the periodic structure [33, 34], the local resonance of the unit cell [35–43], and the coupling between the two approaches [43, 44]. Many original topologies have been proposed and optimized to widen the band gap [45–49]. The study of PnCs / Meta-materials has thus become one of the most active and rapidly growing disciplines in physics (condensed matter physics, propagation of waves in heterogeneous and periodic media) and in engineering (telecoms, acoustics , ultrasound, mechanical engineering, geophysics).

PnCs are no doubt one of the most promising approaches to the manipulation and control of acoustic and elastic wave propagation [50–52]. Cavities and waveguides based on PnCs, for example, offer the possibility of advanced engineering of the scattering properties and can potentially provide modes with greatly reduced group speeds (near-flat modes). These have been theoretically and experimentally demonstrated for different acoustic waves (such as bulk waves [1, 2], Rayleigh waves [53, 54] and Lamb waves [3, 55]) in the solid/solid or solid/fluid PnCs. In recent years, much work has been done on PnCs and meta-materials to control elastic waves in micro-electromechanical system (MEMS) resonators to reduce energy losses via supports and anchors, and sensitivity to noise disturbances from sources of environmental vibration [56–58]. However, researchers still face the challenge that concepts are both original and compatible with MEMS technologies. Robustness is a point that is not often taken into account, since the performance of PnCs integrated MEMS imposes strict restrictions on the area and volume of structures. Establishing robust topologies and optimizing PnCs performance and meeting the requirements of MEMS applications remains a major problem.

Objectives

This work is interested in the resonators periodically deposited on a substrate operating in hypersonic regimes. The idea in this thesis is to design and characterize new concepts and structures of artificial materials by theoretical and numerical approaches, for optimally isolating or confining an acoustic wave. The objective of this thesis is divided into two main lines : 1) Investigate the interaction of elastic Love waves with holey or pillared PnCs and propose new resonators for the development of advanced functions for signal processing. 2) Study the interaction of Love waves with pillared meta-surface to explore the coupling between adjacent pillars for potential applications in wave control. The detailed goals of our work are listed below :

•Study the Interaction of Love waves with periodic structures like PnCs and meta-surface. Understand the mechanisms of phononic band gaps, which refer to Bragg scattering and local resonance.

•Build theoretical models to study band structures and transmission spectra of two dimensional holey and/or pillared PnCs by the finite element method. Highlight the existence of band gaps and local resonances.

•Discuss the geometrical and elastic parameters influences on the resonances.

•Design and characterize new resonators with strong resonances, which refer to isolated modes or interaction of adjacent surface resonators. Study and optimize their performance.

•Propose solutions to exploit the mechanisms of new resonators for the development of advanced functions for signal processing.

Thesis organisation

Besides the current introduction, the content of this thesis is divided into 6 chapters :

Chapter 1 brings up the history of phononic crystals and gives the bibliography of materials with periodic structures, the experimental methods and technologies, the waves involved to interact with PnCs, and the interaction between different acoustic resonators. Applications of PnCs are also presented.

Chapter 2 reviews the fundamental theories of PnCs used in this work, including essential elastic theory, the propagation of different surface acoustic waves (SAW), lattice and band structure theories as well as the mechanisms of band gaps.

Chapter 3 describes the theoretical models built with the Finite Element Method (FEM) using COMSOL software in order to study the band structures and transmission spectra of different PnCs interacting with Love waves. Energy depth is calculated to select the surface waves, as well as the shear horizontal polarization ratio to distinguish Love waves from SAW. Displacements and polarizations of surface eigenmodes are provided. Different geometrical parameters are discussed as well as the consideration of material composition.

Chapter 4 studies the local resonance of the pillared PnC. The relation between hybridization band and the periodicity is provided. Acoustic analogue of Autler-Townes Splitting, cavity modes and acoustically induced transparency are observed for two lines of pillars that are perpendicular to the direction of waves propagation. The distance between the two lines of pillars plays a main role on the pillars performance. Fano resonances are observed for the geometrically different pillars which is alternate in a line that is perpendicular to the waves propagation direction. The coupling between the different pillars become more strong when their geometrical difference or the periodicity decreases. By combing these two simple structures, a passing band with tunable width

and frequency can be realized.

Chapter 5 introduces defect states into the holey PnC by removing lines of holes from the guiding film perpendicularly to the propagation direction. New flat cavity modes are observed in the band gap of the perfect PnC and give rise to transmission peaks isolated from outside band. Geometrical parameters such as holes radius, cavity width and crystal size are discussed. Cavity modes in pillared and mixed PnCs are also observed. By introducing lines of pillars into the cavity, we studied the coupling between the pillars mode and the cavity modes. Single pillar line in the cavity is investigated by modifying the position of the pillar. Collective pillars give rise to extremely flat modes that lead to sharp transmission peak. When pillar mode frequency approaches the cavity mode, peak splitting effect is observed on the original cavity mode. The pillars are found to be able to significantly improve the quality factor and transmission of the cavity mode.

The last chapter summaries all works and gives some perspectives.

Chapitre 1

States of the Art

This Chapter brings up the context of phononic crystals (PnCs) and meta-materials. The presentation is divided into three lines : the first line reviews the history and advances of materials with periodic structures, as well as the experimental methods and technologies. The second line is about the involved waves that interact with PnCs. The third line presents the interaction between different acoustic resonators. Finally, the applications of PnCs are given in the last part.

1.1 History and context of phononic crystals and meta-materials

The theory of PnCs is based on the elastic waves propagation in periodic structures. Corresponding investigations can go back to Floquet's research on the unidimensional Mathieu equation in 1883 [59]. Then, Rayleigh initiated the study on the propagation characteristics of elastic waves in continuous periodic structures in 1887 [60], where he predicted the existence of certain frequency ranges in which the waves can not propagate. In 1953, Brillouin conducted a comprehensive systematic study of the propagation properties of periodic materials [61]. In 1965, acoustic Bragg mirrors were introduced as an idea of unidimensional periodic organizations to reflect waves [62].

Initially inspired by an analogy with the quantum mechanical band theory of solids in which electronic waves interact with a periodically arranged atomic lattice to form energy bands separated by band gaps, photonic crystals (PtC) were proposed by E. Yablonovitch [63] et S. John [64] in 1987, where they proved that the systems composed of periodic structures of dielectric materials for dispersive components of electromagnetic waves can provide frequency bands in which the electromagnetic waves are completely reflected.

Time comes to 90 decades. In 1992, inspired by PtCs studies, M. M. Sigalas and E. N. Economou have theoretically demonstrated the existence of band gaps for elastic waves propagating in periodic structures [50]. The term "phononic crystals" was first proposed by Kushwaha, Halevi, Dobrizynski and Djafari-Rouhani [52] in 1993 when studied out of plane waves in a periodic array of nickel alloy cylinder in an aluminum alloy matrix. Then in 1994, they proposed several basic rules about two-dimensional (2D) structures involving metal cylinders in a solid matrix [65]. Two-dimension denotes that the periodicity of PnC is two dimensional. In 1995, the first manifestation with a band gap in a 2D PnC was presented by Martinez-Sala [66] using a minimalist sculpture of Eusebio Sempere exposed in Madrid that can be seen in the figure 1.1. The sound attenuation is measured in outdoor conditions for sound-wave vectors perpendicular to the cylinders' vertical axis. The observed attenuation peak frequency, the volume fraction occupied by the scatterers and the velocity ratio are all compatible with theoretical predictions. The existence of band gap in PnCs was first confirmed. Since then, the PnCs investigation has caused a great deal of concern.

Before 2000, all PnCs were designed on the theoretical basis of Bragg scattering, which requires lattice constants corresponding to wavelengths. This is the limit of the construction of PnCs. In 2000, Liu et al.[35] designed a matrix of silicon-coated lead spheres embedded in epoxy, as shown in figure 1.2, which has a much smaller periodicity than propagating wavelengths and is capable of opening band gaps in the sonic regime.

Figure 1.1 – First demonstration of phononic band gap by the sculpture of Eusebio Sempere.[66]

This PnC is called locally resonant phonon crystal (LRPnC), since the band gap results from the relative motions of the individual constituents of the crystal. They showed that their PnC behaves as a medium with a negative effective elastic constant, which integrate into the category of acoustic meta-materials. This discovery has developed another search domain for PnCs.

In addition to these most important discoveries that we have mentioned above, in the whole research process of PnCs, there are also many great achievements in this domain, which have made tremendous contributions to the subsequent research. The first bi-dimensional PnC in the laboratory was realized simultaneously by Vasseur et al. [67] and Sanchez-Perez et al. [68] in 1998. In the same year, Sprik et al. [69] proposed the idea of transfer from 2D PnC to 3D PnC. Two years later, the first demonstration of a 3D PnC was realized [35]. By the mid-2000s, many practical demonstrations had been performed, but all were in macroscopic scales (single inclusion diameter >1 mm) [1, 2,

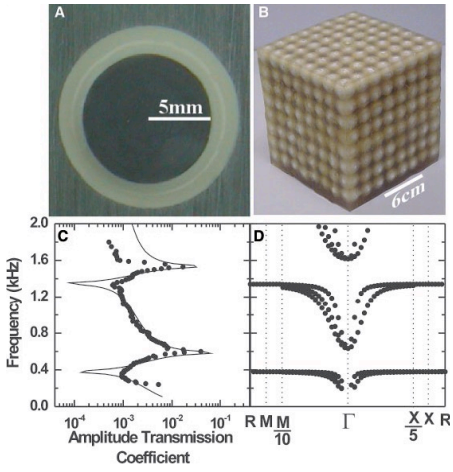

FIGURE 1.2 – First demonstration of LRPnC. (A) Cross section of a coated lead sphere that forms the basic structure unit (B) for an 8×8×8 sonic crystal. (C) Calculated (solid line) and measured (circles) amplitude transmission coefficient along the [100] direction as a function of frequency. (D) Band structure of a simple cubic structure of coated spheres. [110] direction is on the left of Γ point while [100] direction is on the right [35].

68, 70–79]. This results in large structures limited to frequencies below 1 MHz. These hand-assembled devices were expensive, inherently lossy, time consuming and difficult to replicate [10]. With the development of micro-fabrication techniques, the research of PnCs was transferred from macroscopic scales to microscopic scales (single inclusion diameter < 100 μm). PnC-based devices could be miniaturized and experimentally verified at very high frequencies (VHF :30-300MHz) and ultra-high frequencies (UHF : 300-3000MHz) [80–83].

Two-dimensional (2D) PnCs attracted the most attention because of the abundant physical connotation. 2D PnC are generally constructed on a semi-infinite substrate or a plate, where the periodic arrays of the inclusions are on or in the host matrix. Wu et al. [81] presented the first realization of a microscopic 2D PnC with a lattice constant of 10μm, as shown in figure 1.3. 2D PnC Band gaps have been observed in several material systems,including Si / air [20, 55, 81, 84–86], SiC / air [11], AlN-TiN / air [87], LiNbO3 / air [88–90], Si / W [91] and SiO_2 / W [4, 10, 92–96]. Solid/solid PnCs demonstrated

lower sensitivity to lithography compared with solid/air PnCs [97], allowing higher operating frequency for radio frequency (RF) and thermal applications. Some devices, such as cavities, requiring very low material damping have been better achieved in solid/air systems by using materials with a high quality factor of resonance (high Q materials) such as Si [55] et SiC [11].

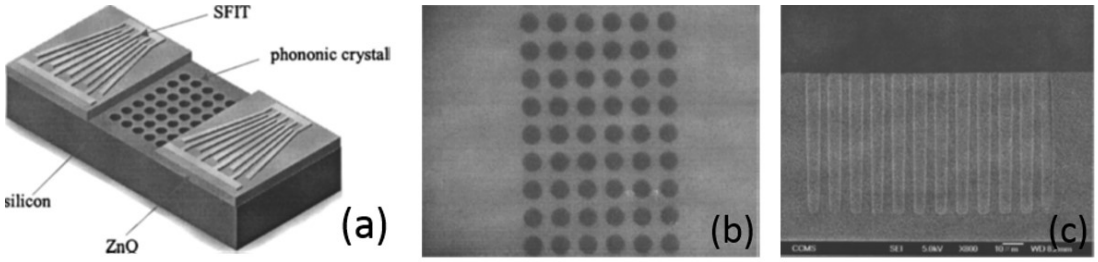

Figure 1.3 – (a) Schematic of air/Si PnC and slanted-finger inter-digital transducers (SFITs); (b) a microscopic picture of the 2D PnC; (c) Cross section of the 2D PnC.[81]

Early investigations of PnCs use bulk acoustic waves (BAW). However, the utilization of BAW is limited in the microscopic experimental aspects because it is really hard to obtain spaced holes with a diameter of 1µm in a material that has a thickness of several hundred micrometers [98]. As a result, surface acoustic waves (SAW)-based PnC have broader application prospects [8, 99, 100]. SAW are guided along the surface, and are confined in the direction perpendicular to the surface. The SAW-interacted PnCs had always been based on periodic holes [25, 101, 102] in the previous investigations before the pillar-based PnCs [103–106] were proposed. In comparison to holes-based PnCs, pillar-based PnCs can avoid the limitation of the host materials thickness. In addition, pillar-based PnCs have a new geometrical parameter (the height of pillars) which can adjust the frequency of acoustic mode and the position of band gaps, along with other parameters [104, 107], resulting in more complex propagation physics and waves confinement [108]. Pillar-based PnCs exhibit Bragg band gap as well as complete local resonant band gap that was proved to be independent of the periodicity [104, 109].

Different forms of inclusions have been discussed to modify the properties of PnCs.

A. C. Hladky-Hennion et al. [110] studied the foam-like PnC consisting of a single metallic phase. It is represented, theoretically and experimentally, to display a perfect adaptation of the negative refractive index and a focusing capacity when it is surrounded by water. S. Hemon et al. [87] presented the PnC based on conical holes drilled in a two-layer plate. The composite plate is formed with a layer of aluminum nitride (AlN) deposited on a thin metal film made of titanium nitride (TiN). The introduction of the TiN plate contributes to slowly widening the band gap which becomes narrow when the holes become conical and which close when the radius of a face of the cone exceeds 15% the radius of the other face. C.-N. Tsai and L.-W. Chen [111] presented the PnC with rectangular pillars. As the length-width ratio of the stud can change the straightness of the equi-frequency curves in the band structure, the waveguide without defect, the application of self-collimation, can be realized with the rectangular pillars . The propagation direction of a self-collimated beam can be manipulated effectively by varying the orientation angle of the inclusions. The coaxial tubes are made by H. Larabi et al. [112]. The inner cylinder (core) is made of steel. This core is covered by alternating shells constituted, respectively, by a thin layer of elastically soft material and a thin layer of a hard material (steel). This coaxial tube is embedded in a water matrix. At very low frequency, strong dips appear in the transmission spectrum. The number of dips evolves in relation to the number of shells. Oral Oltulu et al. [15] proposed the PnC in elliptic section of BaTiO3 pillars in a polar liquid (water). The band structure and the width of the band gap are the functions of the orientation angle. The largest standardized band gap was found at two different angles, $\theta = 0°$ and $\theta = 90°$. The appearance and disappearance of the band gap implies a rotational anisotropy for angles of $\pm 45°$. The hierarchical structure is proposed by Y. Chen and L. Wang [113] as a class of honeycombs, shown in Fig 1.4. The composition of regular honeycombs and hierarchical honeycombs is a vitreous polymer, SU-8. Hierarchical honeycombs have large and multiple acoustic band gaps. The mechanisms responsible for these band gaps depend on the geometric

characteristics of hierarchical honeycombs rather than their composition.

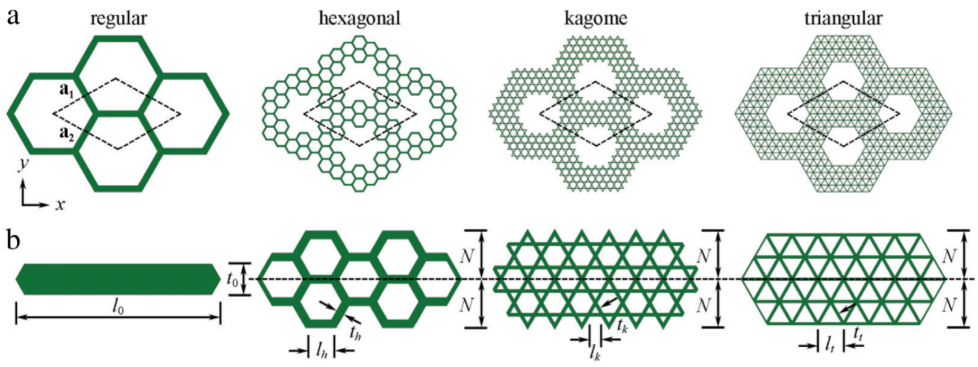

FIGURE 1.4 – (a) Diagram of a classic honeycomb and hierarchical honeycombs. l0 and t0 are the length and thickness of the cell walls. Dashed lines indicate supercells. (b) Diagram of the cell walls of classical honeycombs, hexagonal, kagome and triangular hierarchical honeycombs, respectively. [113]

By removing a subset of the diffusers, defects can be created in the PnCs. The defects can introduce small passing band into the initial band gap [1], giving rise to applications such as waveguide [2, 93, 114], cavity [1, 55, 115], filter [5, 75] and multiplexer [116]. An example was given by the group of R. H. Olsson III [10]. Figure 1.5 shows the waveguide made in the PnC based on the W inclusions in a SiO2 matrix. In the center of each tungsten inclusion is a release hole. Aluminum nitride (AIN) transducers were utilized on each side of the PnC for electrical characterization. The idea of defect is not limited to removing inclusions. Any irregularity in the crystals can be regarded as a defect. Tube in a pillared PnC were developed by Yabin Jin et al. [115].The tubes and pillars are made of silicon, as well as the plate on which they are built. Lamb waves were generated. A small bandwidth appears in the forbidden band due to the whispering-gallery mode of the tube. By changing the inner radius of the tube, these modes can exist both within Bragg band and low frequency band. The quality factor can be greatly improved by introducing an additional cylinder between the tube and the plate.

Based on the idea of defect, A. Salman et al. [18] digitally realized a Mach-Zehnder interferometer (MZI) formed by fluid-filled linear-defect waveguides in a 2D PnC, shown

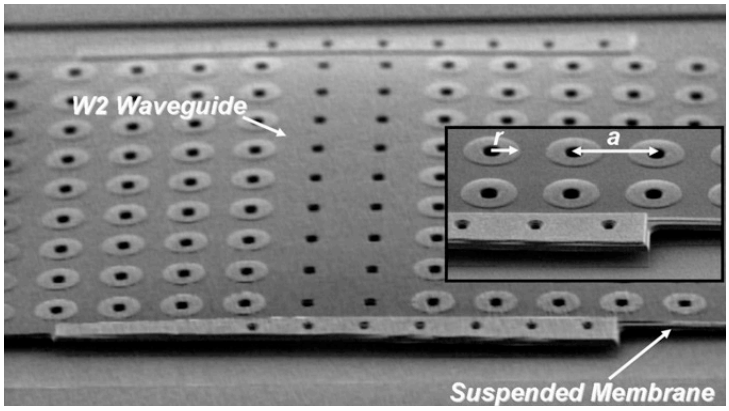

FIGURE 1.5 – SEM image of a waveguide made by removing 2 rows of W scatterers from a phononic crystal square lattice plate. Inset shows the suspended plate and an AIN transducer[10]

in Figure 1.6, to detect low concentrations of a analyte. PnC is composed of a square array of empty steel cylinders. The detection of low concentrations of ethanol in the order of 0.1 % in a binary mixture with water is achieved by replacing the contents of a number of waveguide cells in an arm of the interferometer with the analyte.

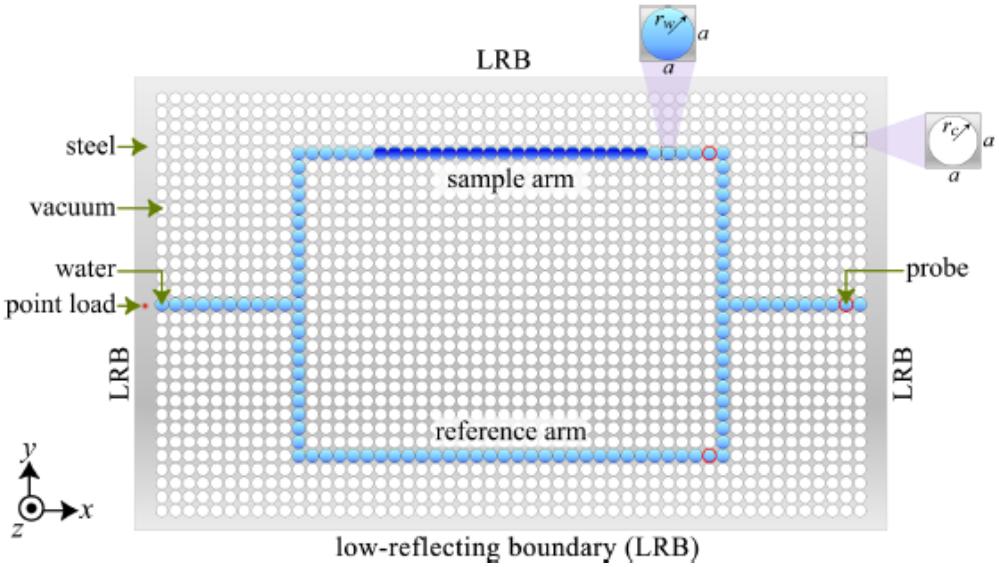

FIGURE 1.6 – Schematic of the MZI incorporating waveguides with linear defects and their T branches in the PnC [18].

A new emerging topic is the research for periodic dual phononic and photonic

materials in which the phonon-photon interaction can be considerably improved with the simultaneous confinement of electromagnetic and acoustic waves [117–119]. Called phoxonic crystals, they have been proved to exhibit phononic as well as photonic band gaps, and to be capable of sensing separately the sound and light velocity with defect states [120, 121].

Besides the topics related to the existence of band gap, there is a continuing increasing interest in the refraction properties of phononic crystals, in particular : negative refraction phenomena and their applications in imaging and focusing (see Fig 1.7) of the sub-wavelength in PnCs [14, 24, 122–124], auto-collimation and beam-splitting with respect to the shape of the equi-frequency surfaces [125] , control of sound propagation with meta-materials focusing on cloaking phenomena [126] ,hyper-lenses [24] and gradient index (GRIN) crystals (see Fig 1.8) [127, 128].

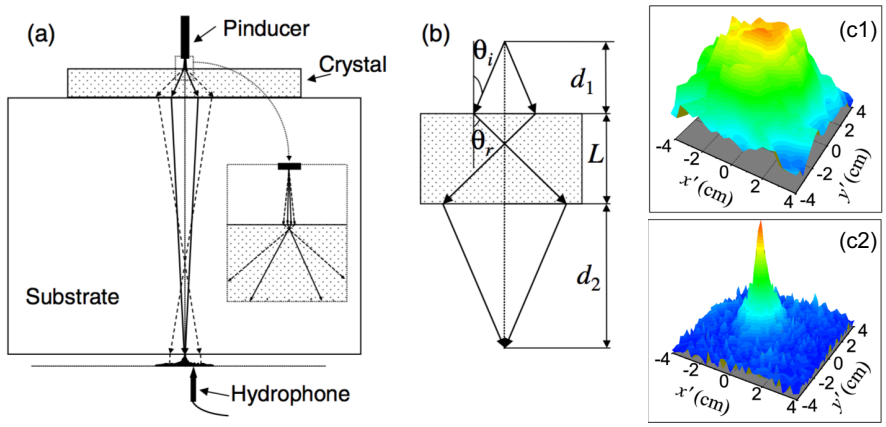

Figure 1.7 – Waves focusing based on negative refraction phenomena in PnC consisting of 0.8-mm-diameter tungsten carbide beads surrounded by water. The beads are arranged in a face centered cubic structure. (a) Experimental setup with rays indicating the predicted directions of group velocity. (b) Diagram showing the focusing condition in the PnC with negative refraction. Filed patterns measured without (c1) and with (c2) the crystal in place. x' and y' axes are in the plane parallel to the sample surface. [78]

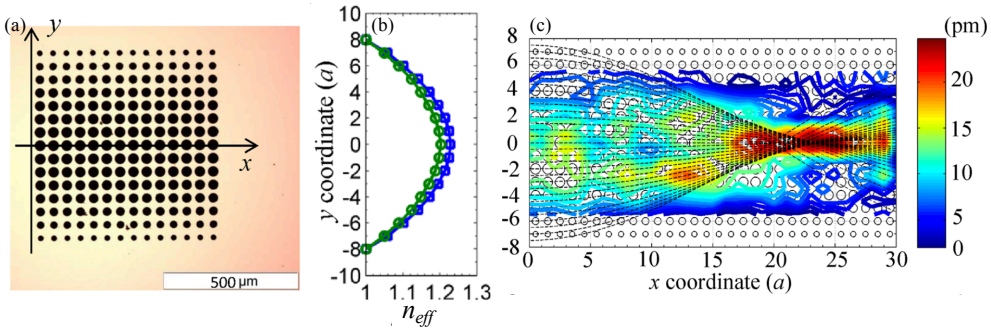

FIGURE 1.8 – PnC with gradient (positive) refraction index by modifying the inclusion radius. (a) Optical image of air holes in a silicon plate. (b) Designed (blue line) and experimental (green line) profiles of the effective refraction index n_{eff}. (c) Experimental maximum of u_z in the acoustic lens with 30 columns of air inclusions. Ray trajectories (thin dashed lines) were obtained by using the experimental wave numbers. [127, 128]

1.2 Involved waves

Nowadays, the potential application of elastic wave devices is the field of mobile communications. The field of sensors is also concerned but in a reduced way for the moment. They are mainly used to filter signals transmitted / received by mobile transceivers. In current systems there are two types of devices : surface acoustic waves (SAW) and bulk acoustic waves (BAW) devices that have been and continue to be the subject of massive scientific production in recent decades. Therefore, most concerning research of PnCs is based on the bulk waves [1, 5, 35, 66, 70, 74], Rayleigh waves [9, 53, 80, 81, 104] and Lamb waves [84, 87, 129]. Many efforts have been made to reduce the number of SAW / BAW devices, or even completely remove them. However, no competitive technology can offer the same performance at the same size and cost today. The trend is therefore in the opposite direction, motivated by the demand for ever higher data rates and the desire to use the same transmitters / receivers in all regions of the world. The number of elastic wave devices in a mobile phone increases with each new generation for mobile communications. The end of this trend is not yet predictable. For the sensor applications, including bio-sensors, the design of resonators is based on surface waves,

typically Love waves and shear horizontal plate waves, since they are compatible with the liquid environment [15, 16] due to a lack of shear motion in liquid [130]. In recent years, the exploitation of Love waves interacting with PnCs has been presented [12, 131–133] and demonstrated to have great application potential.

1.2.1 Bulk waves

Bulk waves propagating in space are frequently used in the PnCs research [35, 66, 70, 74]. Bulk waves devices in vacuum and isolated from the substrate can confine the energy in a 2D acoustic band gap [94]. However, in general, the energy of the bulk waves dissipates faster than that of the surface waves. Substrate insulation is therefore commonly used to confine the waves to the surface [10], as shown in Fig 1.9. High reflectivity is achieved by the Bragg mirror, a 1D PnC, for longitudinal waves propagating normal to the mirror. The reflection of off-axis waves and transverse waves is degraded, which limits the isolation of the substrate and the quality factor (Q). In contrast, 3D PnCs reflect acoustic waves incident at any angle and the band gap covers a wide frequency range to reflect longitudinal and transverse waves.

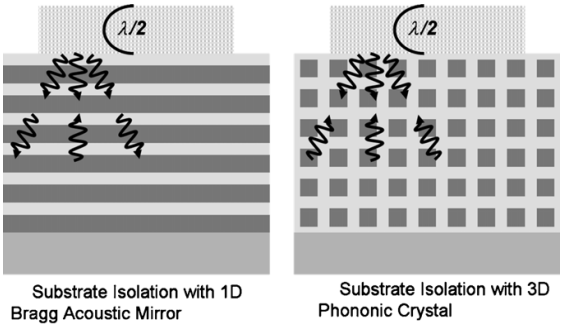

Figure 1.9 – (a) Substrate isolation by a 1D Bragg mirror of ¼ wavelength thick of each layer ; (b) Substrate isolation by a 3D PnC. [10]

Khelif et al. [1, 2] presented a square array of steel cylinders dipped in water, and observed a complete band gap, shown in Fig 1.10. After adding a point defect, they observed a peak in the band gap region, due to a resonance mode caused within the

defect. The number of resonance modes corresponds to the number of peaks. The continuous defect points, i.e. a linear defect, gives rise to a passing band in the band gap. The wave is thus guided by the defect. The appearance of passing band is due to the appearance of new resonance modes, or defect modes, in the band structure. Some other examples of defect based application designs were also proposed by their group and are shown in Fig 1.11 [5, 75, 116, 134]. In addition to the removal of a point or a line, multiple processes are used to create defects : to drill a hole on a cylinder, i.e. the substitution of a tube for a cylinder [75, 115] ; to discard two lines of pillars or to vary the height of a pillar[5], etc. The idea is to provoke an irregularity in the system.

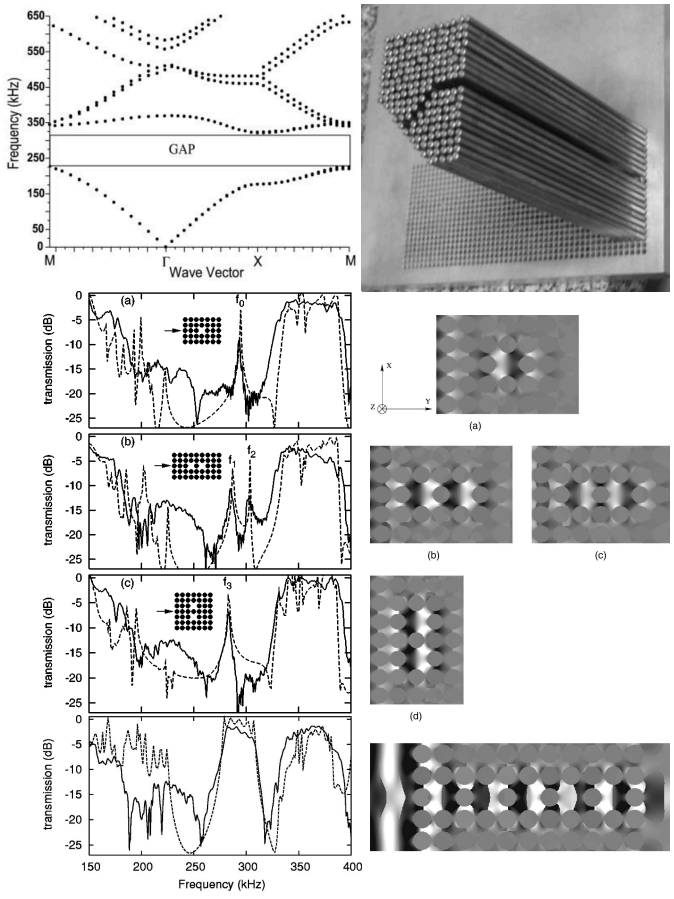

FIGURE 1.10 – (a) Band structure of the perfect PnC ; (b) Steel cylinders with linear defect or waveguide ; (c) Transmission curves for different point defects in PnC ; (d) Corresponding resonant modes or defect modes in PnC. [1, 2]

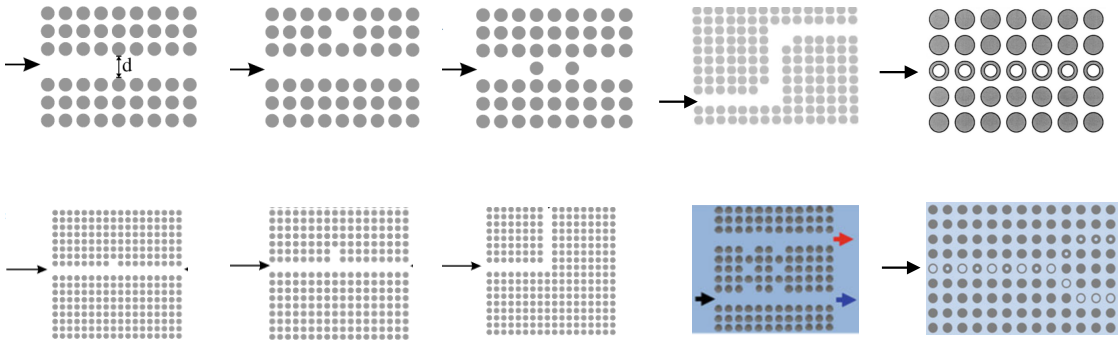

FIGURE 1.11 – Different defect based application designs for 2D PnCs. [5, 75, 116, 134]

Bulk waves are used in many PnCs applications, including communications radio frequency (RF) (waveguides [2], cavities [1], filters [75], multiplexers [116], the acoustic diodes [6]) and isolators [10], the control of sound propagation [83], the liquid captors [18], the thermoelectric materials [22], meta-materials (including hyperlens [24], imaging [26, 79], focalization [31, 78, 110], auto-collimation [30], beam-splitting [29], interferometer [32], cloaking [126]), etc. Given its incompatibility with the use in liquid medium, applications like bio-sensor are few.

1.2.2 Rayleigh waves

Rayleigh waves propagating on the surface of a semi-infinite substrate are widely investigated [9, 80, 81, 101, 104, 135]. They have two components : the longitudinal waves and the vertical transverse waves. Wu et al. [9] presented a holey PnC on a substrate composed of Si/ZnO. Figure 1.12 shows the two-port SAW device, surrounded by two PnCs as reflective grating to isolate the acoustic waves.

Benchabana et al. [53, 54] etched a square array of holes on a $LiNbO_3$ substrate. Transmission attenuations were observed, with the peak value at -37dB, shown at Fig 1.13. Then they added a linear defect, a waveguide. Nevertheless, the transmission was also attenuated, with the peak value at -35dB. This means that the transmission curves of the two cases are not very different. The effect of defects has not been proven

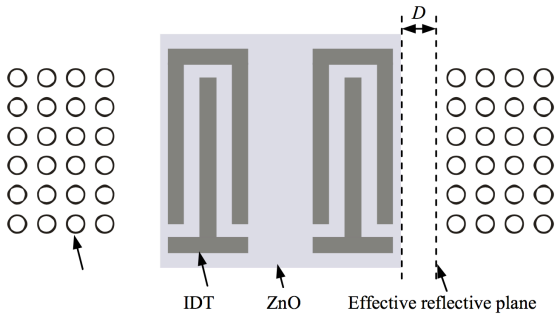

FIGURE 1.12 – Schematic of two-port SAW device using holey PnC as reflective grating. [9]

on the Rayleigh waves. We think that it is because Rayleigh waves are easily diffused in volume, so that the defect modes on the surface are difficult to produce.

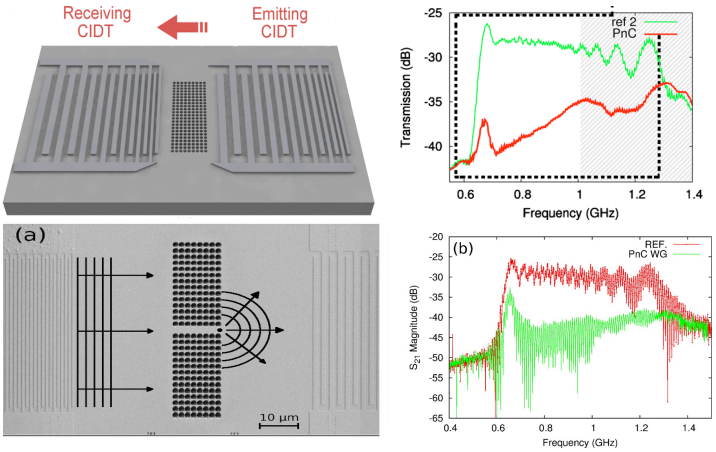

FIGURE 1.13 – (a) Schematic of the experimental setup used to study the Rayleigh wave propagation in a square array of holes on a semi-infinite $LiNbO_3$ substrate; (b) Transmission of Rayleigh waves through the perfect PnC. The green line indicates the transmission without PnC; (c) Schematic of PnC with linear defect; (d) Transmission of Rayleigh waves through the waveguide. The red line indicates the transmission without PnC. [53, 54]

The interaction of Rayleigh waves with pillar based PnCs has also been investigated. Since pillared PnCs can give rise to both Bragg and local resonant band gaps, investigation on the effect of lattice symmetry and pillar form has become the main subjects of many studies. In 2011, Achaoui et al. [103] experimentally validated this principle

by using a square array of nickel pillars on a lithium niobate substrate (Fig 1.14(A)). In their later work, they investigated the nickel pillars arranged in different lattice symmetries [104], see Fig 1.14(C), and demonstrated that locally resonant band gap in the low frequency range is almost independent of periodicity. However, it has been shown that Rayleigh waves interacting with pillared PnCs is easily diffracted because they are not well confined at the surface. Oudich et al. [136] proposed the multi-layered pillars constructed by alternating layers of silicon and PMMA, see Fig 1.14(D). This structure has been shown to be capable of well confining Rayleigh waves to the surface of the substrate. The group of G.R. Nash reported the interaction of Rayleigh waves with annual holes consisting of 128°YX-$LiNbO_3$, shown in Fig 1.15. These annual holes support locally resonant band gaps, analogous to pillar-based geometries, but improve upon them in a potentially transformative way and give rise to enormous band gap attenuation of up to an order-of-magnitude larger than that achieved with the pillars of the same size.

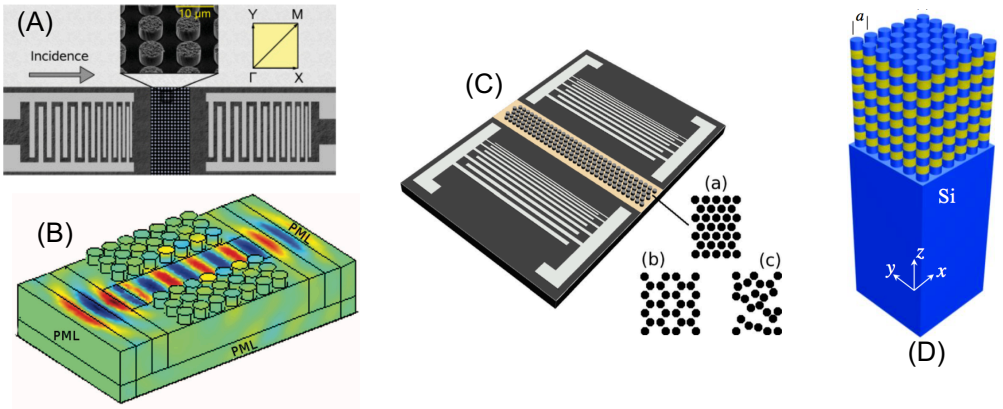

Figure 1.14 – Examples of pillar based PnCs interacting with Rayleigh waves. (A) [103], (B) [137], (C) [104], (D) [136].

Rayleigh waves-based PnCs could be used in the acoustic isolators [8, 9], focalization [127], auto-collimation [25], sensor [14], etc. Note that Rayleigh wave scattering has limited its applications.

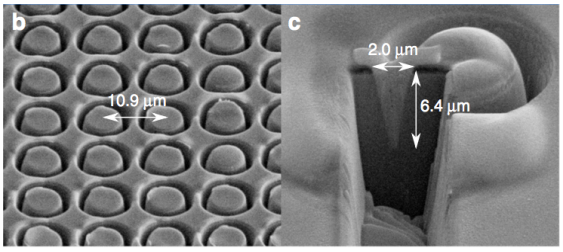

FIGURE 1.15 – (left) Section of a square array of annular holes made of 128°YX-$LiNbO_3$. (right) Cross section depth profile of an individual annular hole [138].

1.2.3 Lamb waves

On the other hand, Lamb waves are confined in a very thin plate, on the order of wavelength or sub-wavelength. It is like two Rayleigh waves propagating on the two surfaces of the plate respectively, and interacting with each other. These structures make it possible to confine mechanical energy in 3D with a fabrication process compatible with microelectronics technologies. The investigation of Lamb waves is also widespread [39, 72, 84, 87, 92, 129].

In the case of membrane-based PnCs, modifying the properties of the crystal requires acting on the geometric shape of the holes and the thickness of the membrane as well as on the choice of material in the case of inclusions based on a material differing from that of the membrane. Several studies have been carried out in this direction during the last decade to show the existence of band gaps, in particular for the engineering of the quality factor in MEMS resonators to minimize leakage of mechanical energy [87, 139–141]. Fig 1.16 illustrates some examples of membrane-based PnCs.

Mohammadi et al. [55] presented the hexagonal lattice PnC of holes on a silicon plate. A band gap between 115 et 150 MHz was observed, shown in Fig 1.17. After removing 4 rows (one period) of holes, surrounded by 12 rows (3 periods) of holes on both sides, a resonance frequency in the middle of the band gap caused a peak with a large quality factor (up to 6300), promoting sensor performance.

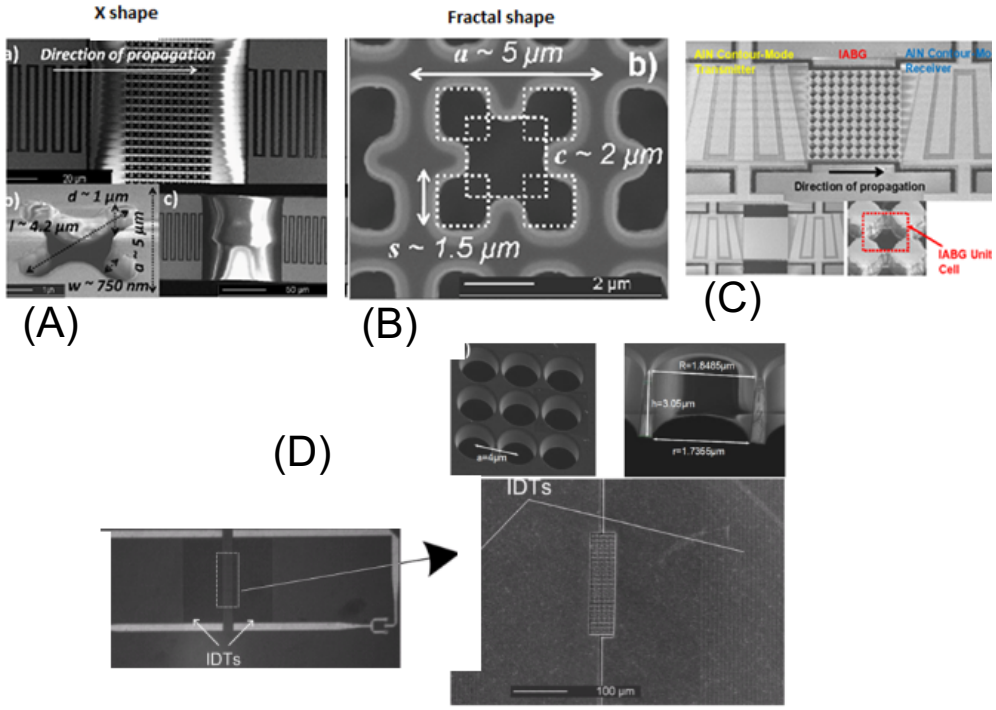

Figure 1.16 – Examples of recently proposed designs of Lamb waves based MEMS resonators for quality factor engineering. (A) [139], (B) [140], (C) [141] (D) [87].

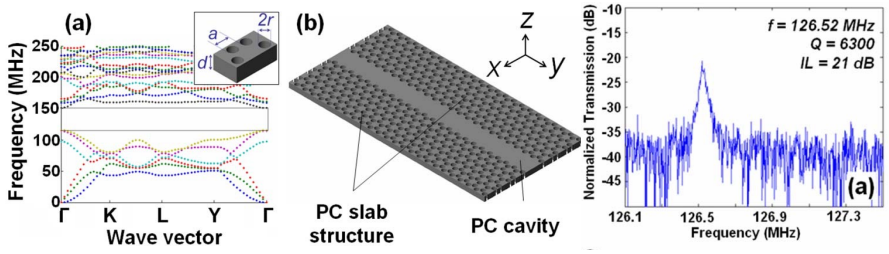

Figure 1.17 – (a) Perfect PnC band structure based on hexagonal holey lattice PnC on a silicon plate ; (b) Schematic of PnC with a waveguide in center ; (c) Transmission of Lamb waves at the frequency in the middle of the band gap, through the defect-containing PnC. [55]

Pillared PnCs interacting with Lamb waves has also been investigated. Some examples of designs are illustrated in Fig 1.18. In 2008, two teams reported independently the PnC via the plate with resonant pillars. Pennec et al. [142] numerically studied a crystal of this type by analyzing the influence of geometric parameters and plate as well as

resonant cylinders materials. Wu et al. [143] simultaneously published an article on a similar structure formed by cylindrical aluminum pillars periodically arranged on an aluminum plate.

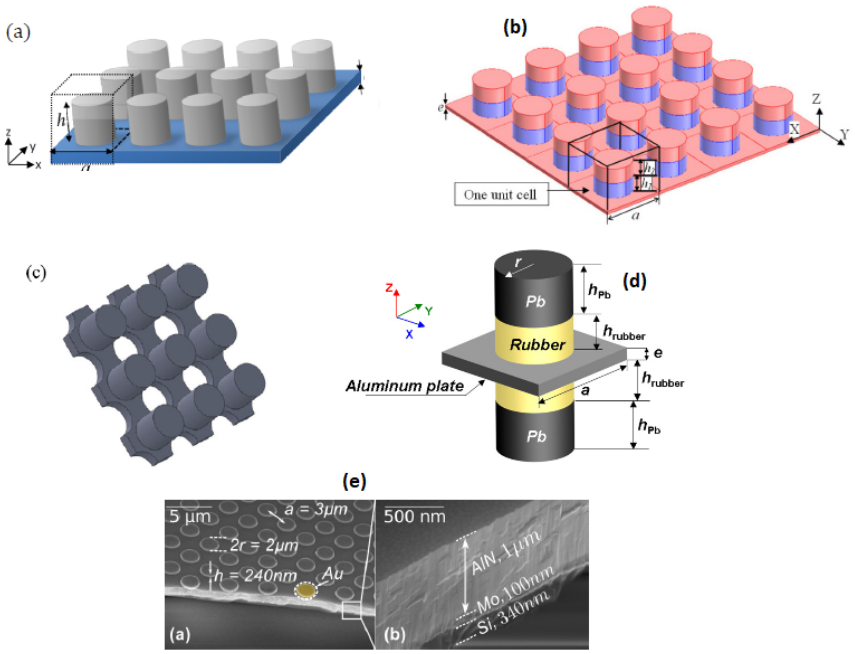

FIGURE 1.18 – Examples of PnC designs based on pillars deposited on a membrane. (a) [142], (b) [39], (c) [144] (d) [42], (e) [109].

In 2010, Oudich et al. [39] studied a phononic crystal formed of an epoxy plate, on which are periodically deposited cylindrical pillars formed of a bilayer of silicone and lead, see Fig 1.18(b). These authors have demonstrated that the opening of the band gap is well associated with the local resonance mechanism. The choice of a soft material (epoxy) for the plate and a composite for the resonant pillar, led to a very weak coupling between the plate and the pillar. This made it possible to obtain a very localized resonance of the mode in the pillar, whereas the resonances are less localized in the structures of Pennec et al. and those of Wu et al. [142, 143] because of the materials chosen. Bilal et al. [144] have proposed a phononic crystal design where they exploited both the pillars and the holes to expand the band gaps, see Fig 1.18(c). Assouar et al.

[42] have demonstrated the possibility of expanding the band gaps of the local resonant crystals by attaching resonant pillars symmetrically to one side and the other of the plate, see Fig 1.18(d). Pourabolghasem et al. [109] have reported a first experimental RF frequency demonstration of a PnC design based on AlN membrane and platinum pillars (Fig 1.18(e)).

Lamb-based PnCs could be used in RF communications (including waveguides [3, 4, 7], cavities and filters [10]), the acoustic isolators [11, 13], focalizations and auto-collimations [28, 145, 146], the thermal control [20, 21, 23], sensors [15–17], etc. Nevertheless, the thin plates used to propagate the Lamb waves are often fragile and therefore difficult to manufacture.

1.2.4 Love waves

As for Love waves, they propagate in a plate constructed on a substrate. So they are also confined to the surface but with a more tough device. They have only one component : the horizontal transverse wave, or shear horizontal (SH) waves. The existence of Love waves requires that the SH velocity in the guiding layer be smaller than that of the substrate. Therefore, many combinations between guiding layer and substrate have been demonstrated. For example, ST-cut quartz substrate with different guiding layers such as SiO_2 [147, 148], PMMA [149, 150] and ZnO [151]. Or it could be a substrate of $LiTaO_3$ with different guiding layers as SiO_2 [152], ZnO [153], gold, SU-8 and parylene-C [152].

Love waves have mainly contributed to the development of liquid sensors [19, 147, 154, 155], and have recently been introduced in the PnCs investigation. In 2013, M. E. Korotyaeva et al. [156] reported Love waves propagating in PnCs based on periodic baffles or cylinders of Pb embedded in a guiding layer of epoxy lying on the uniform substrate of Si, see Fig 1.19. The dispersion characteristics of the structure were investigated by modifying the depth of Pb baffles (or cylinders).

In 2014, T.-W. Liu et al. [12, 131] investigated the interaction of Love waves with

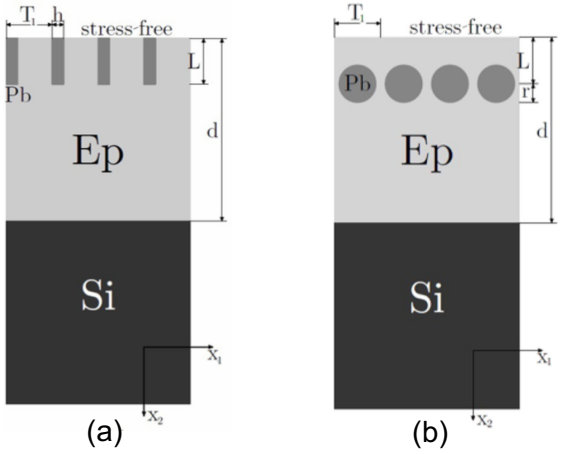

FIGURE 1.19 – Periodic (a) baffles or (b) cylinders of Pb embedded in a guiding layer of epoxy lying on the uniform substrate of Si. The structure is periodic in the sagittal plane and uniform along the out-of-plane direction. [156]

PnC based on etched holes in a SiO_2 plate on a quartz substrate, shown in Fig 1.20, and observed partial band gaps in the x-axis direction. Note that the complete band gap is preferred in the sensor manipulation to avoid waves diffusion in all directions. The partial band gaps is waiting to be improved. In 2019, J. Bonhomme et al. [157] brought the concept of multi-layered pillars into Love wave based PnC for mass sensing application, see Fig 1.21. The pillar is made of successive layers of silica (SiO_2) and tungsten (W) with the SiO_2 layer on its both ends. Despite the technical difficulty, it was numerically demonstrated that this structure can give rise to a sharp transmission attenuation.

Despite the lack of results for PnC investigation on Love waves, we could consider them given the confinement of Love waves. This is why we introduce Love waves into this work. We will investigate Love waves interacting with different structures such as defect states in PnC, pillar based PnC and pillared meta-surface.

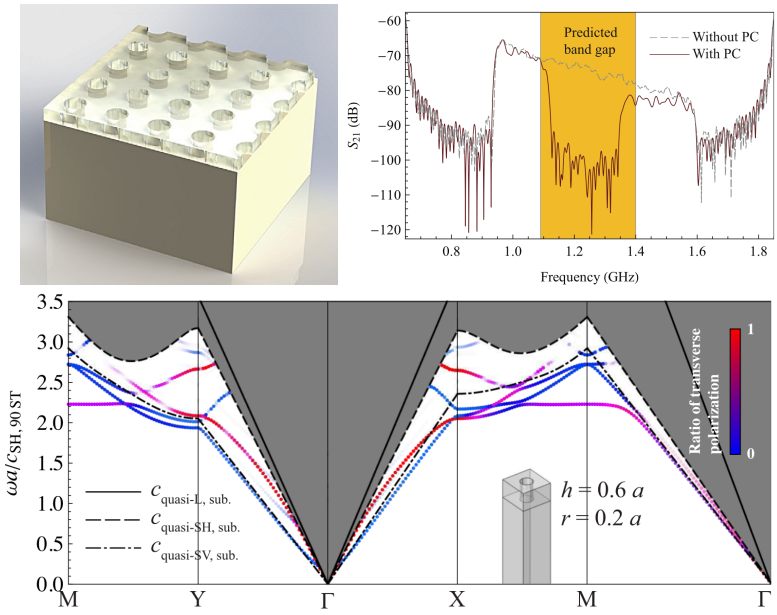

FIGURE 1.20 – (a) Schematic of the PnC composed of holes etched on a SiO_2 plate deposited on a quartz substrate ; (b) Transmission of Love waves through the PnC along the direction ΓX ; (c) PnC band structure. Red indicates Love modes, blue indicates Rayleigh modes. [12, 131]

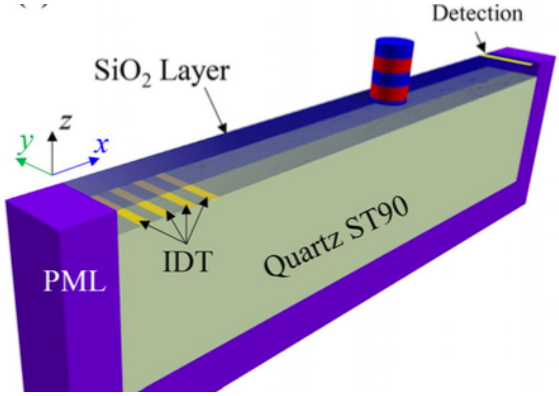

FIGURE 1.21 – Schematic representation of the unit cell used for simulation of the multi-layered pillar based system. The periodicity is along the y direction. [157]

1.3 Interaction of acoustic resonators

In recent years, the control of mechanical vibration as building block for the investigation of quantum related effects has attracted considerable attentions in platforms

such as opto-mechanics [158–162], plasmonics [163–165], nano-mechanics [166, 167] and acoustics [116, 136, 168–171]. The coherent control of the vibration properties [166, 167], coupling effects [160, 171, 172], dissipative [173] and nonlinear characteristics [174] of the mechanical resonators gives rise to a wide variety of applications in sensors [175–177] and signal processing [178–180]. While different modes in a single mechanical resonator can be coupled by tuning related parameters [166, 174, 181, 182], different mechanical resonators can be coupled through various medium [116, 159–161, 169, 171, 183, 184] or via direct contact interaction [185, 186]. In acoustics, coupled resonators has been reported in systems such as cavities [171], waveguides [169], cavity/waveguide [116] or local resonators [170, 187]. The interaction between different resonators allows correlation mechanisms to be scaled up to the resonator array to handle systems with higher fineness [133, 136, 171, 180, 188, 189].

Y. Jin et al. [183, 187] reported the interaction between pillars arranged perpendicularly or parallel to the Lamb waves propagation direction, see Fig 1.22. Strong coupling effect was observed between the pillars and was proved to be function of the geometric parameters. These simple structures exhibit different features related to condensed matter physics such as transmission zero, Fano resonance, acoustic analog of Autler-Townes Splitting (ATS) and electromagnetically induced transparency (EIT).

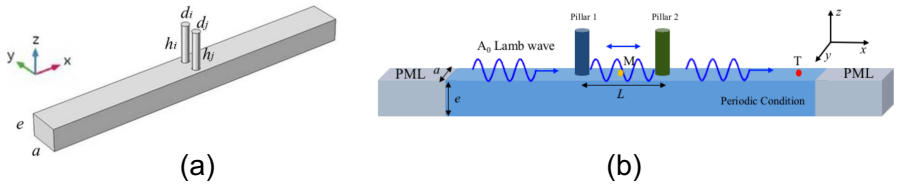

FIGURE 1.22 – Schematic of the unit cells of pillared meta-surfaces. Lamb waves propagate along the x-axis. (a) [187], (b) [183]

R. A. Jahdali et al. [180] reported the design of a sound trapping device based on the coupled Helmholtz resonators (HRs) loaded to an air waveguide, as shown in Fig 1.23(b). The HR can be modeled by a classical mass-spring system, and the effective

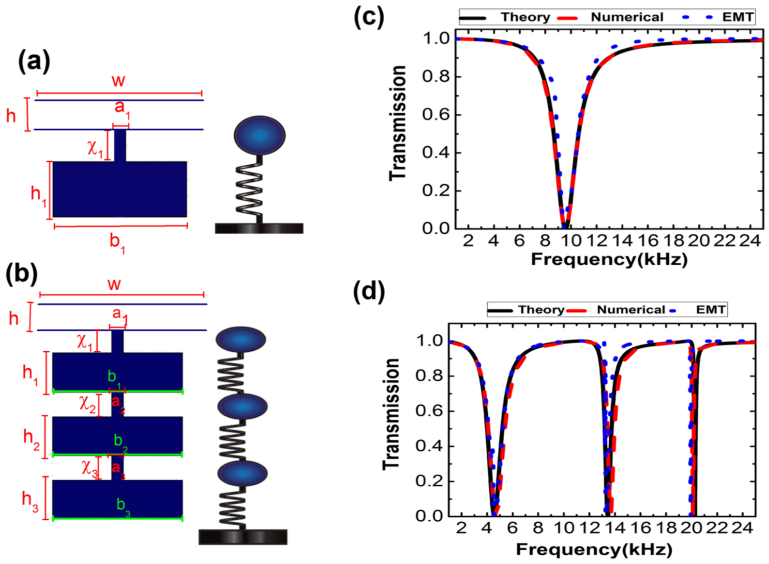

FIGURE 1.23 – Schematic of the building block of (a)single HR and (b)three coupled HRs meta-material, and the corresponding mechanical mass-spring system. (c,d) The transmission coefficient of a plane wave incidence from the left side on the unit cell theoretical prediction (black solid curve), and numerical simulation (red solid curve), compared with the transmission coefficient of the same plane wave incident on an effective homogeneous slab (blue dots curve) for the unit cell is illustrated in (a,b), respectively. [180]

bulk modulus is calculated based on the effective medium theory (EMT). N coupled resonators cause negative effective bulk modulus near the resonance frequency and induce N flat bands that give rise to the confinement of the incoming wave inside the resonators with corresponding strong absorptions in the transmission spectrum.

A. V. Korovin et al. [171] investigated a silicon corrugated nanobeam including two cavity connected by a waveguide, shown in Fig 1.24. The cavity combines symmetric stubs grafted on each side and circular holes drilled in the middle. The overlapping of two closely spaced phononic cavity modes leads to the formation of symmetric and antisymmetric modes, which can be used for the modulation of the frequency and the quality factors of the propagating cavity modes. The efficient coupling of cavity modes of the same symmetry with the standing modes of a phononic waveguide has been

demonstrated. Such coupling can be used for routing, controlling, and modulating the phononic cavity modes over large distances between cavities.

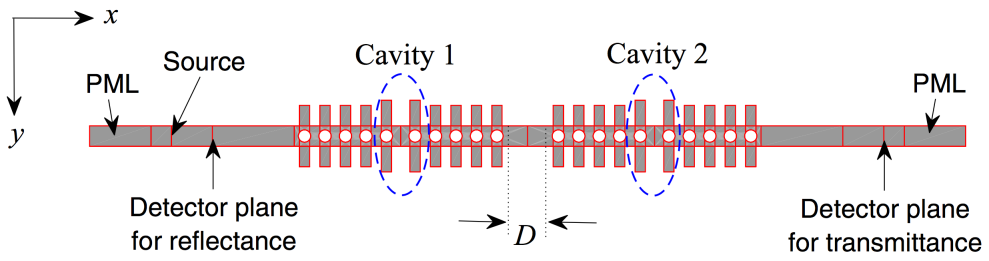

FIGURE 1.24 – Schematic presentation of the phononic nanobeam including two cavity connected by a waveguide. [171]

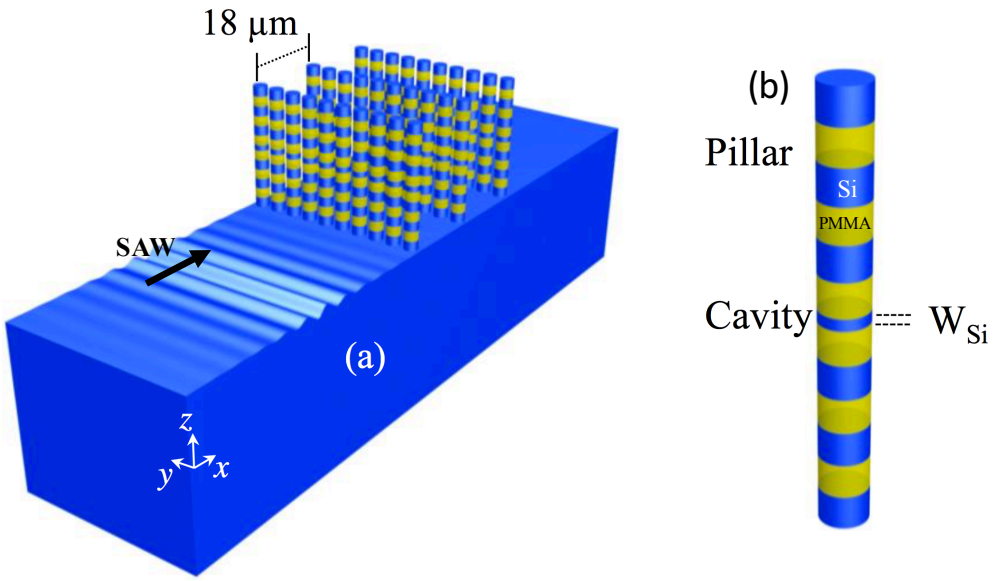

FIGURE 1.25 – (a) Schematic view for the transmission through three rows of PC pillars spaced by 18μm in the x direction. (b) Phononic pillar where the structural defect is constructed by changing the thickness W_{Si} of the central Si layer. [136]

M. Oudich et al. [136] designed a cavity in multi-layered pillars constructed by a periodic stacking of PMMA and Si layers on a Si substrate, as shown in Fig 1.25. The pillar acts like 1D PnC and gives rise to band gaps along the pillar. When coupled with surface acoustic waves (SAW), local resonant modes are found at the pillar substrate interface and produce SAW attenuation. By tailoring a defect inside the pillar, cavity

modes were created in the band gap and lead to sharp SAW transmissions. The strong coupling between the cavity modes and the confined local resonant modes can give rise to a Fano-like resonance as well as an acoustic analog of electromagnetically induced transparency (EIT).

In this work, we will design and characterize different resonators with strong resonances, which refer to isolated modes or local resonant modes. The interaction between these resonators will be investigated to develop advanced functions for signal processing or sensing applications.

1.4 Interests and applications

By analogy with electrons, the development of photon devices contributes to wireless communication and the use of optical fibers and microwaves [190]. Since electrons and photons play an important role in electronics and optics, phonons as another important type of particles are responsible for the transmission of sound and heat in acoustics and thermodynamics. This is because sound and heat can be described as mechanical vibrations in atomic networks. The difference is that acoustic waves oscillate at low frequencies and propagate over a wide distance, whereas most heat vibrations oscillate at high frequencies and propagate in short distances.

Since the band structure is scalable with the dimensions of unit cell, phononics play a role in a wide frequency range from Hz to THz, which gives PnCs a great potential for applications. With the development of PnCs in both the theoretical and experimental aspects, tremendous works has been devoted to the propagation of waves in the range of sonic (kHz) and ultrasonic (MHz) frequencies in the past two decades. The easiest to understand is an acoustic isolator, which reduces acoustic waves by taking advantage of band gaps, using in the scientific aspect (including substrate isolation [10], the reflective grating [9, 11, 12] and the acoustic diode [6, 191, 192]) and in everyday life (including

noise attenuation [130] and the anti-seismic structure [8]), see Fig 1.26.

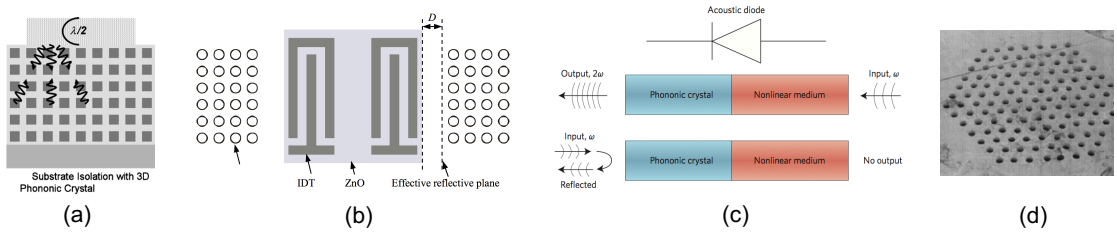

FIGURE 1.26 – Different applications based on band gap effect of the PnCs : (a) substrate isolation [10], (b) reflective grating [9], (c) acoustic diode [192], (d) anti-seismic structure [8].

Many functional devices for RF communications originate from the introduction of point or linear defects in PnCs, such as waveguides [2, 93, 114],cavities [1], filters [75], multiplexers [116] and devices based on their combination, see Fig 1.27.

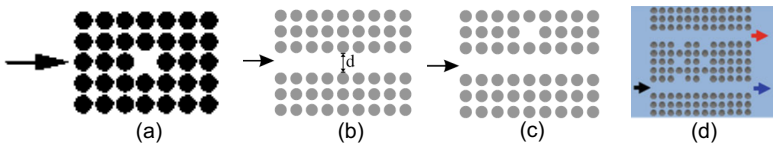

FIGURE 1.27 – Different applications based on defect states in PnCs : (a) cavity [1], (b) waveguide, (c) cavity combined with waveguide [5], (d) multiplexers [116].

As the resonant frequency (and therefore the phase velocity) is affected by the working environment, sensors could be created by a disturbance of the characteristics of the trajectory on which the acoustic waves propagate, see Fig 1.28, including the concentration of the liquid (or gas) [15, 17, 18], the pressure [14] and the mass applied to the PnCs surface [19], etc.

Besides the band-gap-based applications for confining and controlling the elastic waves propagation, the applications of the wave dispersion characteristics can be quite interesting even without the appearance of band gap, such as negative refraction phenomena and self-collimation, which are at the origin of the potential applications, including imaging [26], focalization [24, 78, 122–124], beam-splitting [125], no-defect

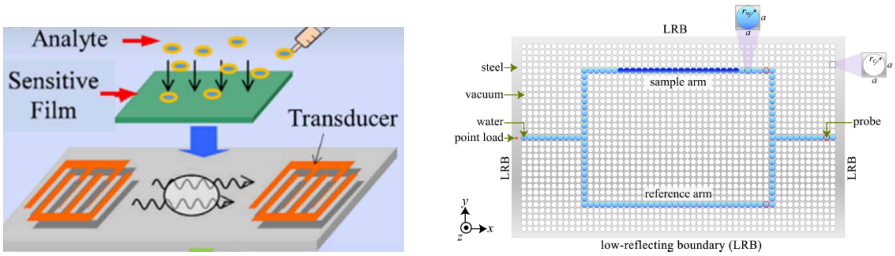

FIGURE 1.28 – Sensor applications based on PnCs. (a) [19], (b) [18].

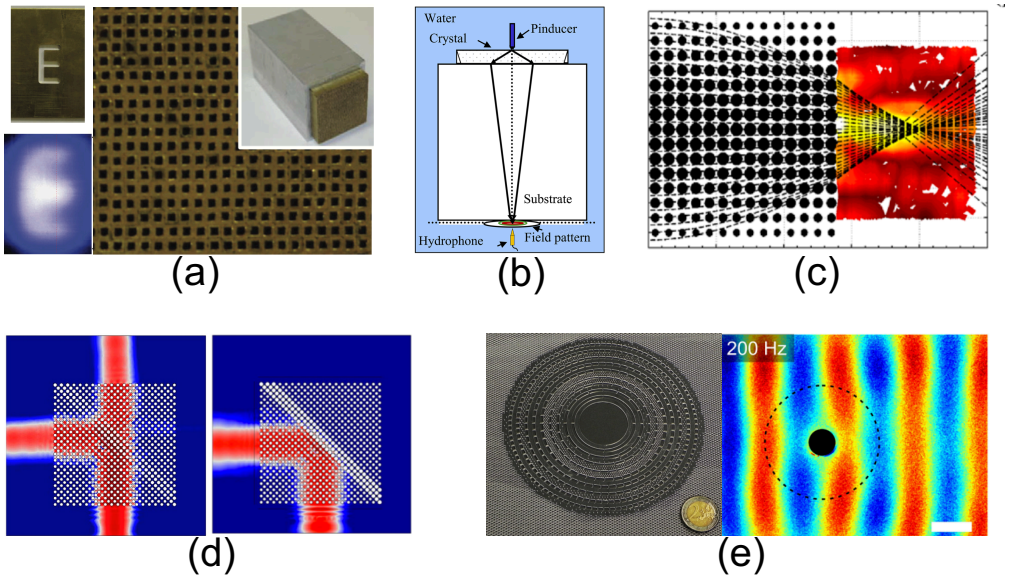

FIGURE 1.29 – Applications of acoustic meta-materials : (a) deep sub-wavelength imaging [26], (b) negative refraction based focalization [31], (c) positive gradient refraction based focalization [127], (d) beam-splitting [29], (e) cloaking phenomenon [193].

waveguide [30], sound propagation control [83], cloaking [126, 193] and hyperlens [24], etc. They can control the propagation of waves surprisingly, and are therefore called metamaterials. A similar theory was used to make thermal metamaterials [27, 190] for high frequency phonons, see Fig 1.30. Understanding and controlling the properties of PnCs also provides us opportunities to thermally insulate the construction and transform lost heat into electricity, etc.

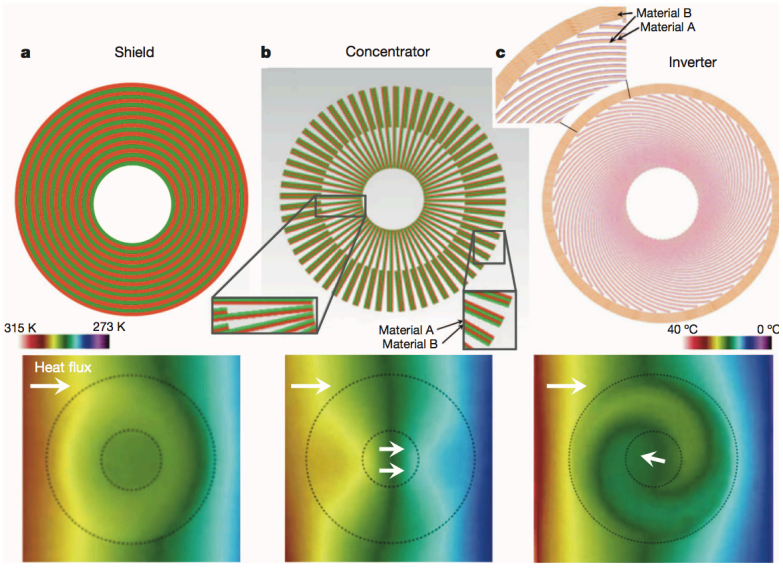

FIGURE 1.30 – Thermal meta-materials : (a) A thermal shield (top), bottom shows corresponding measured temperature profile for horizontal heat flux (white arrow). (b) A thermal concentrator. (c) A thermal inverter. [190]

1.5 conclusion

In this chapter, we reviewed in the first step the history and context of the phononic crystals (PnCs) and meta-materials. As an analogy of the periodically arranged atomic lattice/dielectric materials that can provide band gaps to prevent the propagation of electronic/electromagnetic waves, these elastic materials with periodic structure provides band gaps for the acoustic waves. The band gap effect of PnCs have attracted a great deal of concern since 90 decades. After the first demonstration of the local resonant PnC in 2000, the investigation of meta-materials has caused increasingly attention. PnCs can be periodically arranged in all the three spatial dimensions. Among them, 2D PnCs is regarded as the most interesting, of which the inclusions can be either holes or pillars. In addition to the Bragg band gap resulting from the periodicity of inclusions, pillar-based PnCs exhibit local resonant band gaps that are almost independent of the periodicity. Different material combinations and inclusion forms are capable of providing variable device properties. The introduction of defects into PnCs can introduce passing band

into the initial band gap and is therefore at the origin of multiple applications such as signal processing and sensors. The investigation on the refraction properties of PnCs gives rise to divers applications for meta-materials.

Secondly, according to the involved acoustic waves that interact with PnCs, we divided most of the existing literature into 4 categories : Bulk waves, Rayleigh waves, Lamb waves and Love waves. They all can give rise to band gaps in PnCs. Since the energy of bulk waves dissipates faster than that of the surface waves, Bragg mirror can be used to confined the waves to the surface. Nevertheless, bulk waves is less used for high frequency devices due to the limit of the manipulation. We compared their functions at the presence of defects, and showed that Rayleigh waves can not well interact with the defect modes because they are not well confined to the surface, which limits their applications. Lamb waves devices are often fragile and difficult to manufacture, although Lamb waves are well confined to the surface. Love waves is considered as a compromise between Rayleigh waves and Lamb waves since they are well confined to the surface and exhibit device toughness. However, there has been a lack of investigation on Love-wave-based PnC devices. Therefore, we chose to study Love waves in this work.

Thirdly, we bought up the interest of investigating the vibration properties and interaction effects of the acoustic resonators. An acoustic resonator may be a cavity, a waveguide, or a local resonator (pillar, Helmholtz resonator, etc.) Coupling may happen for different modes in a single resonator by tuning related parameters, or among different resonators through various medium. The coupling effects allows to handle systems with higher fineness. Our goal is to design and characterize different resonators with strong resonances, and to investigate the interaction between these resonators to develop advanced functions for signal processing or sensing applications.

Finally, based on different physical properties, we presented divers applications of PnCs, such as acoustic isolators based on band gap effect, thermal control based on high

frequency waves, RF communications based on defect modes, sensors based on wave propagation, and meta-materials based on wave dispersion characteristics.

Chapitre 2

Fundamental Theories on Phononic Crystals

In this chapter, we review the fundamental theories of phononic crystals (PnCs) used in this work. Firstly, we present the essential elastic theory for the deformation of a solid. By considering the piezoelectricity of the materials, we obtain the elastic waves' propagation equations in piezoelectric structures. Then, the propagation equations are adapted to different surface acoustic waves (SAW, including Rayleigh waves, Lamb waves and Love waves) by adopting corresponding boundary conditions. Next, we present lattice and band structure theories for analyzing the periodic systems. Finally, we introduce two different mechanisms of band gaps that may exist in the PnCs.

2.1 Elastic waves propagation

2.1.1 Generalized Hooke's law

Under the action of external forces, a solid undergoes a deformation as its particles move relatively to each other. Suggest that $u_i(x_j)$ is the displacement of a material point at coordinates x_j $(i, j = 1, 2, 3)$ in an orthonormal coordinate system. The deformations

are defined by the strain tensor :

$$S_{ij} = \frac{1}{2}\left(\frac{\partial u_i}{\partial x_j} + \frac{\partial u_j}{\partial x_i}\right) \tag{2.1}$$

The stresses that develop in this solid tend to restore it to its initial form. In an elastic medium, the stresses are canceled when the deformations cease. Hooke's law is used for small deformations where we can assume that the relation between stress and strain is linear :

$$T_{ij} = c_{ijkl} S_{kl} = c_{ijkl} \frac{\partial u_l}{\partial x_k} \tag{2.2}$$

by summing from 1 to 3 on all repeated indices. T_{ij} is the i^e component of the force acting on the unit of surface perpendicular to the axis x_j. The tensor of elastic rigidity of four rank, c_{ijkl}, is symmetric with regard to the first two indices (since $T_{ij} = T_{ji}$), and to the last two (since $S_{kl} = S_{lk}$). It is therefore reduced to the rigidity matrix $c_{\alpha\beta}$ with α and β varying form 1 to 6.

The balance of forces acting on a volume $\mathscr{V}$ delimited by the surface $\mathscr{S}$ inside a solid is

$$\int_{\mathscr{V}} F_i \mathrm{d}\mathscr{V} + \int_{\mathscr{S}} T_i(\vec{n}) \mathrm{d}\mathscr{S} = 0 \tag{2.3}$$

with $T_i(\vec{n}) = T_{ij} n_j$. $\vec{n}$ is the unitary vector normal to the elemental surface $\mathrm{d}\mathscr{S}$. $\vec{F}$ is the external volume force density. According to the Green theory, the equilibrium condition of a volume leads to :

$$F_i = -\frac{\partial T_{ij}}{\partial x_j} \tag{2.4}$$

By denoting by ρ the density of the solid and by $\ddot{u}_i$ the acceleration of the particles, the fundamental law of dynamics applied to an elementary volume $\mathrm{d}V$ leads to the equation of translational motion

$$\frac{\partial T_{ij}}{\partial x_j} = \rho \ddot{u}_i - F_i \tag{2.5}$$

2.1.2 Elastic-electric field

In piezoelectric materials, the mechanical subsystem is coupled to the electromagnetic one. Since the velocity of the elastic waves is much lower than the that of the electromagnetic waves, the electromagnetic field becomes quasi static. Therefore, the magnetic field is negligible ($\vec{\text{rot}}\vec{E} = -\frac{\partial \vec{B}}{\partial t} \approx 0$) and the Maxwell equations are simplified to :

$$\begin{cases} E_i = -\frac{\partial \Phi}{\partial x_i} \\ \frac{\partial D_j}{\partial x_j} = \rho_e \end{cases} \tag{2.6}$$

with E_i, Φ, D_j, ρ_e denoting the electric field , potential, electric displacement field and free charge density per unit volume, respectively.

The direct piezoelectric effect expresses the polarisability of certain dielectrics when they are deformed ; the opposite effect indicates that a piezoelectric material, placed in an electric field, is subjected to stresses and deforms. This gives the additional terms which express the mechano-electric coupling by the piezoelectric constant e :

$$\begin{cases} D = \varepsilon E + eS \\ T = cS - eE \end{cases} \tag{2.7}$$

2.1.3 Propagation equations

The substitution of the relations (2.2) into the equations (2.7), then to the equations (2.5) and (2.6) leads to, in the absence of external sources (F_i et $\rho_e = 0$), four homogeneous partial differential equations of order two, called the propagation equations :

$$\begin{cases} \rho \ddot{u}_i = c_{ijkl} \frac{\partial^2 u_l}{\partial x_j \partial x_k} + e_{kij} \frac{\partial^2 \Phi}{\partial x_j \partial x_k} \\ e_{jkl} \frac{\partial^2 u_l}{\partial x_j \partial x_k} = \varepsilon_{jk} \frac{\partial^2 \Phi}{\partial x_j \partial x_k} \end{cases} \tag{2.8}$$

These are the fundamental equations of elastic waves propagating in a piezoelectric medium. The resolution of the previous system in plane waves, of polarization $^{\circ}u_i$, propagating in a direction indicated by the unit l_j, at the speed $V = \omega/k$:

$$\begin{cases} u_i = {}^{\circ}u_i e^{j(\omega t - k l_j x_j)} \\ \Phi = \Phi_0 e^{j(\omega t - k l_j x_j)} \end{cases} \tag{2.9}$$

leads to the three plane waves propagating in the same direction whose polarizations are orthogonal.

2.2 Surface acoustic waves

In order to predict the different types of surface waves, the influence of the boundary conditions on waves propagation will be examined. The case of the isotropic medium is presented as an example.

2.2.1 Rayleigh waves

Rayleigh waves propagating on the surface of a semi-infinite medium have two components : the longitudinal and transverse vertical waves (contained in the sagittal plane defined by the normal to the surface and the wave vector).These two components are out of phase by $\pi/2$. Therefore the polarization is elliptical. The amplitudes of these components decay differently with depth. The wave propagation causes a vibration of the surface, which is felt to a depth of the order of the wavelength λ. Let's set Ox_3 the normal to the free surface directed to the interior of the solid and Ox_1 the direction of propagation. A wave decreasing with the distance x_3 to the surface is expressed as :

$$u_i = {}^{\circ}u_i e^{-k\chi x_3} e^{j(\omega t - k x_1)} \tag{2.10}$$

with $\mathrm{Re}[\chi] > 0$. The mechanical boundary condition is the cancellation of the stress T_{i3} on the free surface $x_3 = 0$:

$$T_{i3}(x_3 = 0) = 0 \tag{2.11}$$

The report of equation (2.10) in equations (2.8) leads to the resolution of the propagation equations for the two components of Rayleigh waves :

$$\begin{cases} u_1 = {}^{\circ}u_1[\mathrm{e}^{-k\chi_1 x_3} - \sqrt{\chi_1\chi_2}\mathrm{e}^{-k\chi_2 x_3}]\mathrm{e}^{j(\omega t - kx_1)} \\ u_3 = j\sqrt{\frac{\chi_1}{\chi_2}}{}^{\circ}u_1[\mathrm{e}^{-k\chi_2 x_3} - \sqrt{\chi_1\chi_2}\mathrm{e}^{-k\chi_1 x_3}]\mathrm{e}^{j(\omega t - kx_1)} \end{cases} \tag{2.12}$$

with

$$\begin{cases} \chi_1 = \left(1 - \frac{V^2}{V_L^2}\right)^{1/2} \\ \chi_2 = \left(1 - \frac{V^2}{V_{TV}^2}\right)^{1/2} \end{cases} \tag{2.13}$$

where $V, V_L = \sqrt{c_{11}/\rho}, V_{TV} = \sqrt{c_{55}/\rho}$ are respectively the phase velocity, the longitudinal and transverse speed, with $V < V_{TV} < V_L$. Rayleigh waves are widely used because they are relatively easy to generate on the surface of piezoelectric crystals.

2.2.2 Lamb waves

When a solid is bounded by two parallel planes, two Rayleigh waves propagate independently on each plane as long as their distance is large compared with the wavelength λ. When the thickness H of the plate becomes of the order of λ, the surface wave components become coupled, and give rise to symmetric or anti-symmetrical Lamb waves.

The Viktorov method proposed a way to understand Lamb waves : suggest that $\phi = \phi(x_3)\mathrm{e}^{j(\omega t - kx_1)}$ is a scalar potential and $\vec{\psi} = \vec{\psi}(x_3)\mathrm{e}^{j(\omega t - kx_1)}$ a vectorial potential, the

displacement field can be written as :

$$\vec{u} = \vec{\nabla}\phi + \vec{\nabla} \wedge \vec{\psi} \tag{2.14}$$

where $\vec{\nabla}\phi$ is a longitudinal wave and $\vec{\nabla} \wedge \vec{\psi}$ a transversal wave. The two components u_1 and u_3 can be calculated :

$$\begin{cases} u_1 = jk\phi - \frac{\partial \psi_2}{\partial x_3} \\ u_2 = jk\psi_2 + \frac{\partial \phi}{\partial x_3} \end{cases} \tag{2.15}$$

The substitution of equations (2.15) in propagation equations (2.8) by neglecting the piezoelectric effect leads to :

$$\begin{cases} \rho\ddot{\phi} = c_{11}\nabla^2\phi \\ \rho\ddot{\psi}_2 = c_{55}\nabla^2\psi_2 \end{cases} \tag{2.16}$$

with $c_{55} = \frac{c_{11}-c_{33}}{2}$ in isotropic medium. The velocity of the longitudinal waves is $V_L = \sqrt{c_{11}/\rho} = \omega/k_L$ and that of the transversal waves is $V_{SV} = \sqrt{c_{55}/\rho} = \omega/k_{SV}$. The expression (2.16) becomes :

$$\begin{cases} \frac{\partial^2 \phi}{\partial x_3^2} + (k_L^2 - k^2)\phi = 0 \\ \frac{\partial^2 \psi_2}{\partial x_3^2} + (k_{SV}^2 - k^2)\psi_2 = 0 \end{cases} \tag{2.17}$$

$\phi(x_3)$ and $\psi_2(x_3)$ are in this way resolved, with solution :

$$\begin{cases} \phi = C_1 \cos(px_3 + B)\mathrm{e}^{j(\omega t - kx_1)} \\ \psi_2 = C_2 \cos(qx_3 + B)\mathrm{e}^{j(\omega t - kx_1)} \end{cases} \tag{2.18}$$

where $p = \sqrt{k_L^2 - k^2}$ and $q = \sqrt{k_{SV}^2 - k^2}$. C_1, C_2 and B are the constants to be determined.

The boundary conditions are the cancellation of stress T_{13} and T_{33} on the two surface

$x_3 = \pm\frac{H}{2}$:

$$\begin{cases} T_{13}(x_3 = \pm\frac{H}{2}) = 0 \\ T_{33}(x_3 = \pm\frac{H}{2}) = 0 \end{cases} \tag{2.19}$$

The substitution of the equations (2.18) in the boundary conditions indicates that $B = 0$ or $\frac{\pi}{2}$, with the determinant :

$$(k^2 - q^2)^2 \tan\left(q\frac{H}{2} + B\right) + 4k^2pq\tan\left(p\frac{H}{2} + B\right) = 0 \tag{2.20}$$

This is the dispersion equation. When $B = 0$, u_1 is pair and u_3 impair, it indicates a symmetric mode. When $B = \frac{\pi}{2}$, u_1 is impair and u_3 pair, it is an asymmetric mode.

2.2.3 Love waves

As for a plate rigidly connected to a semi-infinite substrate whose transverse wave velocity is greater than that in the plate, a shear horizontal wave (of polarization parallel to the surface) bears the name of Love. This wave propagates in different modes and is reflected without changing nature. The polarization of Love waves is along the axis Ox_2 :

$$u_2 = u_2(x_3)\mathrm{e}^{j(\omega t - kx_1)} \tag{2.21}$$

The substitution of the formula (2.21) in the propagation equation (2.8) by neglecting the piezoelectric effect suggests :

$$c_{44}\frac{\partial^2 u_2}{\partial x_3^2} - 2jkc_{46}\frac{\partial u_2}{\partial x_3} + (\rho\omega^2 - k^2c_{66})u_2 = 0 \tag{2.22}$$

In the plate (guiding layer) isotropic, of thickness H, $c_{44c} = c_{66c} = \rho V_{SHc}^2$ and $c_{46c} = 0$.

The expression (2.22) is simplified :

$$\frac{\partial^2 u_2}{\partial x_3^2} + \left(\frac{\omega^2}{V_{SHc}^2} - k^2 \right) u_2 = 0 \tag{2.23}$$

This is a differential equation of order two. To allow a guiding wave in the layer, it is necessary that the discriminant $\Delta = -4\left(\frac{\omega^2}{V_{SHc}^2} - k^2\right) = -4\left(\frac{V^2}{V_{SHc}^2} - 1\right)k^2$ is less than 0 (otherwise the solution will be exponential, which is not a guiding mode). This implies :

$$V > V_{SHc} \tag{2.24}$$

This results in the periodic solution :

$$u_2(x_3) = {}^{\circ}u_2 \cos\left[k\sqrt{\frac{V^2}{V_{SHc}^2} - 1}(x_3 - H) \right] \tag{2.25}$$

H is a constant determined by the mechanical boundary conditions on the surface $x_3 = H$:

$$T_{23}(x_3 = H) = 0 \tag{2.26}$$

In the piezoelectric substrate ($x_3 \leq 0$), therefore, anisotropic, the discriminant of the equation (2.22) is : $\Delta = -4k^2\rho_s V_{SHs}^2 c_{44s}\left(\frac{V^2}{V_{SHs}^2} - 1\right)$, with $V_{SHs} = \left(\frac{c_{44s}c_{66s} - c_{46s}^2}{c_{44s}\rho_s}\right)^{1/2}$ being the shear horizontal velocity in the substrate. The displacement should be null for $x_3 = -\infty$, which implies $\Delta > 0$. This results in :

$$V < V_{SHs} \tag{2.27}$$

and the solution :

$$u_2(x_3) = C_1 e^{m_1 x_3} + C_2 e^{m_2 x_3} \tag{2.28}$$

with $m_{1,2} = \frac{j2kc_{46s} \pm \sqrt{\Delta}}{2c_{44s}}$ and C_1, C_2 the constants to be determined. The attenuation of

waves in the substrate implies that $C_2 = 0$. Supposing the substrate is isotropic or has a direct axis of symmetry of order 4 or 6, we have $c_{44s} = c_{66s} = \rho_s V_{SHs}^2$ and $c_{46s} = 0$. Therefore, the solution is :

$$u_2(x_3) = C_1 \exp\left(k\sqrt{1 - \frac{V^2}{V_{SHs}^2}}x_3\right) \tag{2.29}$$

The value of C_1 and the Love mode are determined by the boundary conditions at the substrate/guiding layer interface (at the plane $x_3 = 0$) : Continuity of displacement and normal stresses :

$$\begin{cases} u_2(x_3 = 0^+) = u_2(x_3 = 0^-) \\ T_{23}(x_3 = 0^+) = T_{23}(x_3 = 0^-) \end{cases} \tag{2.30}$$

This leads to :

$$\begin{cases} C_1 = {}^\circ u_2 \cos(Hk\chi_1) \\ \tan(Hk\chi_1) = \frac{\chi_2 c_{44s}}{\chi_1 c_{44c}} \end{cases} \tag{2.31}$$

with

$$\begin{cases} \chi_1 = \left(\frac{V^2}{V_{SHc}^2} - 1\right)^{1/2} \\ \chi_2 = \left(1 - \frac{V^2}{V_{SHs}^2}\right)^{1/2} \end{cases} \tag{2.32}$$

The last formula (2.31) is the dispersion equation, which has an infinite number of solutions :

$$(Hk)_n = \frac{1}{\chi_1}\arctan\left(\frac{\chi_2 c_{44s}}{\chi_1 c_{44c}}\right) + n\frac{\pi}{\chi_1} \qquad n = 0, 1, 2, \ldots \tag{2.33}$$

This formula reflects an increase $\Delta H = \frac{\pi}{k\chi_1}$ in guiding layer thickness from one mode to the next. Figure 2.1 shows the variation of the phase velocity as a function of the guiding layer thickness. The wave thus described is guided in the guiding layer (periodic solution) and its amplitude decreases exponentially in the substrate. Note that the propagation of Love waves is only possible if the shear horizontal waves velocity in the guiding layer is inferior than that of the substrate, and that the fraction of energy

transported in the layer increases with the increase of the guiding layer thickness.

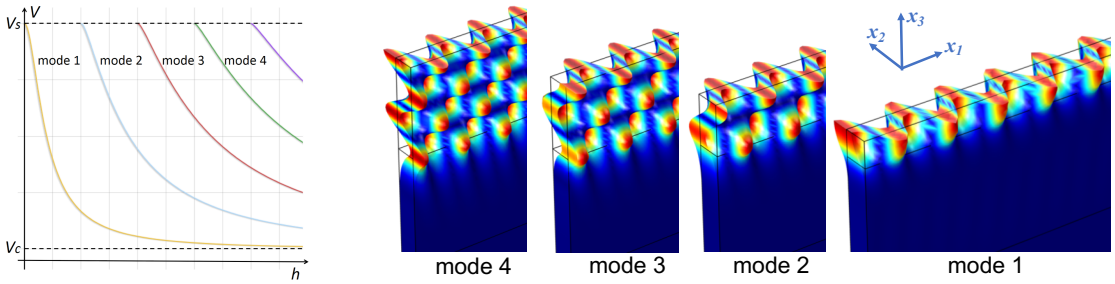

FIGURE 2.1 – Love waves phase velocity as a function of the guiding layer thickness. The deformation fields of the first 4 modes are shown on the right side.

2.3 Lattice periodic condition

Periodic systems are supposed to be very large or even infinite. The idea to investigate such a structure is to reduce the periodic system to a unit cell, and to apply periodic conditions on the boundaries of this cell. The periodic conditions depend on the periodicity along the directions, to express the fact that the conditions of the input acoustic waves are identical to those of the output waves of the cell, with a defined phase shift. According to Bloch-Floquet's theorem, a formula is used to describe the periodic behaviors of the displacement field and the propagation of the elastic waves. Thus, for a periodic infinite domain, the periodic boundary conditions can be written in the form of plane waves :

$$\begin{cases} u(\vec{x}+\vec{a}) = \mathrm{e}^{-j\vec{k}\vec{a}}u(\vec{x}) \\ \Phi(\vec{x}+\vec{a}) = \mathrm{e}^{-j\vec{k}\vec{a}}\Phi(\vec{x}) \end{cases} \tag{2.34}$$

where $\vec{a}$ is the periodic vector of the crystal. u is the displacement and Φ the potential.

2.3.1 Bloch theorem on PnC lattice

A point is used to represent a basic cell that repeats indefinitely in the PnC. Then, the PnC can be considered as a spatial matrix of points. A crystal can be constructed by translating the unit cell with 3 non-planetary vectors $\vec{a_1}$,$\vec{a_2}$,$\vec{a_3}$, which are the basic vectors of the lattice. The coordinates of each point in the crystal can be expressed by a linear composition of the 3 basic vectors :

$$\vec{R_n} = n_1\vec{a_1} + n_2\vec{a_2} + n_3\vec{a_3} \tag{2.35}$$

where $\vec{R_n}$ is the direct or Bravais lattice vector. For any position $\vec{r}$, its physical quantity $f(\vec{r})$ (like density, elastic constants, etc.) also has a periodicity that satisfies :

$$f(\vec{r}+\vec{R_n}) = f(\vec{r}) \tag{2.36}$$

$f(\vec{r})$ is periodic and can therefore be developed as a Fourier series :

$$f(\vec{r}) = \sum_h F(\vec{G_h})\mathrm{e}^{j\vec{G_h}\vec{r}} \tag{2.37}$$

The substitution of 2.37 in 2.36 leads to the relation :

$$\vec{R_n}\cdot\vec{G_h} = 2k\pi \tag{2.38}$$

where k is an integer, $\vec{G_h}$ is the vector of the reciprocal lattice, represented by 3 non-planetary vectors $\vec{b_1},\vec{b_2},\vec{b_3}$, which are called the basic vectors of the reciprocal lattice :

$$\vec{G_h} = h_1\vec{b_1} + h_2\vec{b_2} + h_3\vec{b_3} \tag{2.39}$$

In this way, the relation between the basic vector of the direct lattice and that of the reciprocal lattice is :

$$\vec{a_i} \cdot \vec{b_j} = 2\pi\delta_{ij} \quad i,j = 1,2,3 \tag{2.40}$$

The crystals have a spatial periodicity and symmetry. As a result, eigenfrequencies and eigenmodes have a certain symmetry. When studying eigenfield, the problem can be relatively simplified.

The first Brillouin zone (BZ) in reciprocal space represents the smallest space divided for each point Γ, ie a primitive cell. It is defined as the Wigner-Seitz cell in reciprocal space, formed by the intersection of the vertical plane passing through the middle K of the two points, a point of origin and all points closest to the origin (see Table 2.1).

If the space of the first BZ has a certain symmetry for a group of points, the first BZ can be further reduced. The new zone is called the irreducible Brillouin zone.

According to Bloch-Floquet's theorem, a linear system of translational periodicity has the same periodicity as crystals. The eigenvalues and the eigenvectors have the properties :

$$\begin{cases} \lambda_{\vec{k},n} = \lambda_{\vec{k}+\vec{G_h},n} \\ u_{\vec{k},n}(\vec{x}+\vec{R_n}) = u_{\vec{k},n}(\vec{x}) \end{cases} \tag{2.41}$$

This means that there is no new eigenvalue outside the irreducible Brillouin zone. Therefore, all values of wave vector are in the irreducible Brillouin zone, which greatly reduces the ranges of $\vec{k}$.

The calculations of irreducible BZ, following the direct and reciprocal lattices, determine the ranges of wave vectors for analysis, see Table 2.1.

2.3.2 Band structure

For a given wave vector $\vec{k}$, a series of eigenvalues and corresponding eigenvectors can be obtained. Each eigenvalue and the corresponding eigenvector represents an

Lattice type	Direct lattice	Reciprocal lattice	1st & Irreducible BZ	Direct & Reciprocal basic vectors
Square	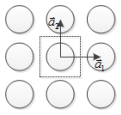	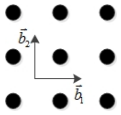	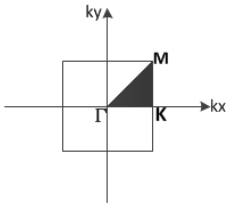	$\begin{cases}\vec{a_1} = a(1,0) \\ \vec{a_2} = a(0,1)\end{cases}$ $\begin{cases}\vec{b_1} = \frac{2\pi}{a}(1,0) \\ \vec{b_2} = \frac{2\pi}{a}(0,1)\end{cases}$
Tri.	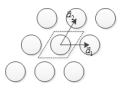	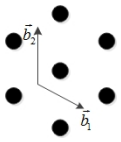	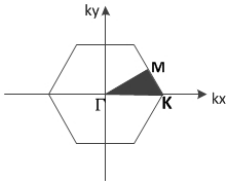	$\begin{cases}\vec{a_1} = a(1,0) \\ \vec{a_2} = a(\frac{1}{2},\frac{\sqrt{3}}{2})\end{cases}$ $\begin{cases}\vec{b_1} = \frac{2\pi}{a}(1,-\frac{\sqrt{3}}{3}) \\ \vec{b_2} = \frac{2\pi}{a}(0,\frac{2\sqrt{3}}{3})\end{cases}$
Hex.	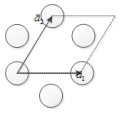	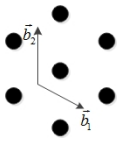	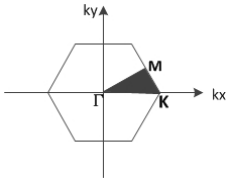	$\begin{cases}\vec{a_1} = a(\sqrt{3},0) \\ \vec{a_2} = a(\frac{\sqrt{3}}{2},\frac{3}{2})\end{cases}$ $\begin{cases}\vec{b_1} = \frac{2\pi}{a}(\frac{\sqrt{3}}{3},-\frac{1}{3}) \\ \vec{b_2} = \frac{2\pi}{a}(0,\frac{2}{3})\end{cases}$

Tableau 2.1 – Direct and reciprocal lattices, first and irreducible Brillouin zones of the common 2D PnCs lattices in isotropic medium. a is the lattice constant. The first BZ are the square (hexagonal) regions while the irreducible BZ are the black triangle regions.

eigenfrequency and corresponding displacement. Since the wave vector is a continuous variable, each eigenvalue becomes a function of $\vec{k}$. When choosing $\vec{k}$ as the horizontal axis and the eigenvalues (eigenfrequencies) as the vertical axis, the relation between them is called the band structure or the dispersion diagram.

It is meaningful to study the band structure of PnCs as it can give much physical information about the crystals. Almost all the investigations and applications of PnCs relies on a band structure analysis.

2.4 Band Gap Mechanism

Phononic band gaps are the ranges of wavelength or frequency within which elastic waves cannot propagate through the structure. Band gaps of PnCs are generally classified into two types : One is due to Bragg diffraction, the other is due to local resonance. The position and width of the band gap depend on the waves propagating directions. Gaps may occur for particular directions of the wave vector, and can also cover the whole Brillouin zone. Generally, a wide band gap requires two main conditions : a large contrast in elastic properties, acoustic velocity and density ; a sufficient filling factor. Materials and lattice type will also influence the band gaps.

2.4.1 Bragg diffraction

The Bragg's law was first established by W. H. Bragg and W. L. Bragg[194] when investigating the diffraction of X-ray in crystals, which could be interpreted as a periodic arrangement of parallel planes, as shown in Fig 2.2. The waves are reflected by the successive layers and will interfere constructively if the path difference is an integer multiple of the wavelength :

$$n\lambda = 2a\sin\theta \tag{2.42}$$

where n is an integer, λ is the wavelength, a is the distance between two crystallographic planes and θ is the angle between the incident wave and the crystal surface. The Bragg's law can be applied more generally in the scattering of a plane wave in periodic media, here for the PnCs are the inclusions with lattice constant a. As the path difference depends on the lattice constant, such Bragg scattering mechanism occurs when the λ is comparable to a.

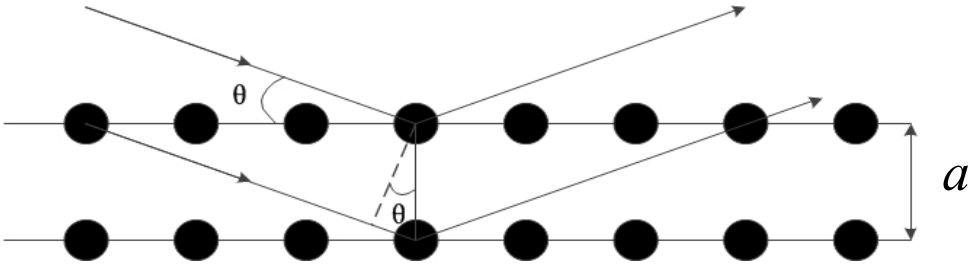

Figure 2.2 – Schematic of Bragg diffraction

When the PnC is 1D, i.e. a successive of plate surfaces with two alternate permittivities, ε_1 and ε_2, we are in the case of a Bragg mirror. The thickness of these two layers are e_1 and e_2, with $e_1 + e_2 = a$ the periodicity. If a normal incident plane wave satisfies :

$$\lambda = 2n_{eff}a \tag{2.43}$$

where n_{eff} is the effective index, the reflected waves will all be in the same phase as the incident wave. Therefore, there is constructive interference between the incident and reflected waves. The reflectivity is maximum and the transmission is null.

2.4.2 Local resonance

Local resonance type band gap, or hybridization band gap, comes from the avoided crossing of two coupled bands in the low frequency range, as shown in Fig 2.3. The generation of locally resonant band gaps depends on the interaction between the scatterers' resonant characteristic and the progressive waves. Because of the resonant scattering,

elastic waves are attenuated sharply during the propagation. The resonance of a single resonator plays the main role. This band gap depends mainly on the intrinsic vibration of the individual particle and persists even with structural disorder. The central frequency of the hybridization band is anti-proportional with the individual particle size. The width of the band gaps increases with the increasing of filling fraction.

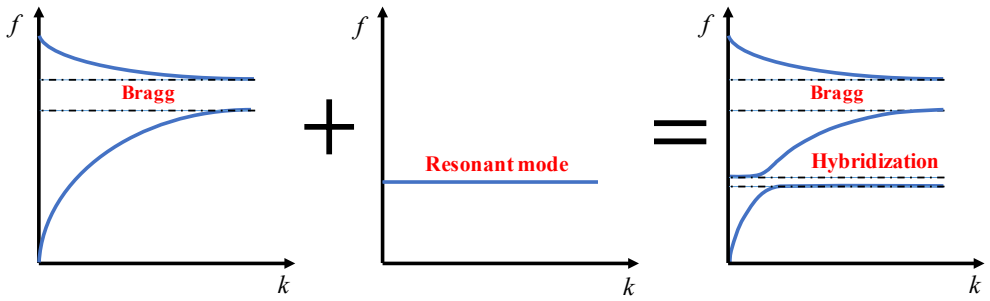

FIGURE 2.3 – Schematic of hybridization band gap formation

Locally resonant phononic crystals were first proposed by Zhengyou LIU in 2000 [35]. Composites which comprise a single microstructure unit composed of relatively high density lead balls and an elastically soft silicone rubber coating are embedded in an epoxy media to form a three-component 3D PnC. The theoretical and experimental results all show that the wavelength corresponding to the band gap of the PnC is much greater than the lattice constant. They also found the existence of band gaps without periodic structures.

2.5 conclusion

In this chapter, we present firstly the generalized Hooke's law as basic elastic theory for small deformations of a solid under the action of external forces. By simplifying the Maxwell equations and considering the piezoelectricity of the materials, we obtain the elastic waves' propagation equations in piezoelectric medium, which can be used to analyze different elastic waves in adopting their corresponding boundary conditions. The

eigenvalue is the wavelength (or frequency) and the eigenvectors are the displacement components. In particular, Love waves exist only when the shear horizontal waves velocity in the guiding layer is smaller than that of the substrate. Love waves amplitude decreases exponentially in the substrate, and the energy transported in the guiding layer increases with the increase of the layer thickness. In a certain system, the thicker the guiding layer, the more modes there are.

Next, we presented the direct and reciprocal lattice of the PnCs, as well as their first and irreducible Brillouin zone (BZ). According to Bloch-Floquet's theorem, the periodic lattices of PnCs leads to periodic displacements. We can therefore calculate the band structure, i.e. the eigen-frequency as function of wave vector, only in the irreducible BZ to analyze the physical characteristics of the PnCs.

Finally, we introduced two different mechanisms of band gaps that may exist in the PnCs. One is the Bragg band gap that results from the Bragg diffraction of waves in the periodic lattice of the PnCs. The central frequency of the Bragg band gap is anti-proportional with the lattice constant, and the corresponding wavelength is comparable to the lattice constant. Another is the local resonant or hybridization band gap which is almost independent of the periodicity of PnCs. It is the coupling result between the intrinsic vibration of the individual particle and the progressive waves. The central frequency of the hybridization band gap is anti-proportional with the particle size, and the corresponding wavelength is much larger than the lattice constant.

This chapter brings up essential theories for analyzing the PnCs, which serves as the basis for comprehension in the next chapters.

Chapitre 3

Interaction of Love Waves with PnCs based on Holes and/or Pillars

Cylinders are the basic inclusion shapes of a 2D PnC. They are usually presented in the form of holes or pillars. This chapter will numerically investigate the interaction of Love waves with basic PnCs based on holes and/or pillars. Love waves are distinguished from SAW by calculating the energy depth and the shear horizontal (SH) polarization ratio. The band structures and the transmissions of Love waves through the PnCs are calculated. Bragg and hybridization band gaps as well as isolated modes are demonstrated. The effects of geometrical parameters are discussed. Different pillar materials are considered to show the effect of the elastic parameters. The modeling and simulation of PnCs was calculated using the finite element method (FEM, COMSOL MULTIPHYSICS).

3.1 Basic unit cell models

Two PnCs based on holes and pillars have been studied in square lattice (Fig 3.1). The unit cells constructed for calculating the band structures for these lattices are shown in Fig 3.2.

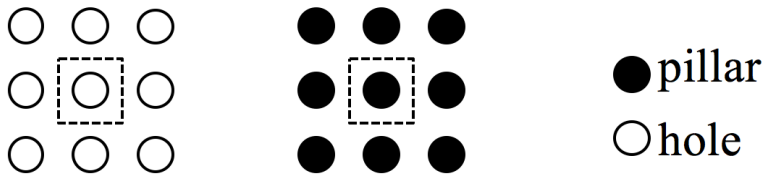

FIGURE 3.1 – Square lattice based on holes (left) and pillars (right).

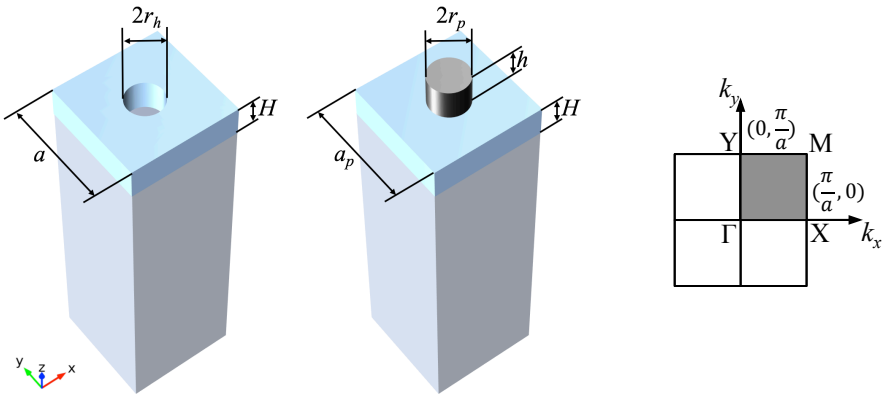

FIGURE 3.2 – Unit cells of the PnCs with square arrayed cylindrical holes, or Ni pillars, respectively in, or on, the silica film deposited on a 90ST-cut quartz. r_h=r_p=0.2a, h=0.6a, H=0.6a, $a_p = a = 4\mu$m. The 1^{st} BZ is shown on the right side of the unit cells. Gray region is the irreducible BZ.

The unit cell used in the Comsol software consists of a 90ST-cut quartz substrate (Euler angles=(0°, 47.25°, 90°), LH 1978 IEEE), a guiding layer of amorphous SiO_2 (ρ = 2200kg/m^3,E = 70GPa, ν = 0.17) and cylindrical hole/nickel pillar (ρ = 8900kg/m^3,E = 219GPa, ν = 0.31). Holes were etched and pillars were built on the guiding layer. The substrate has been rotated 90 degrees around the z-axis from the ST-cut quartz, since a fast SH waves (5000m/s) can be generated by the electric field along the x-axis (the y-axis of the ST-cut quartz), where Rayleigh waves can not be generated[12] due to a zero electromechanical coupling factor to the substrate. The shear wave velocity in the silica film is 3438m/s, less than that in the 90ST-cut quartz substrate, indicating the existence of Love waves.

The square array period or the lattice constant is $a = 4\mu$m. The height of the substrate

is 40μm. The thickness of the SiO_2 layer is $H = 0.6a = 2.4\mu$m, which equals to the hole depth. The hole radius is $r_h = 0.2a = 0.8\mu$m . The pillar has the same size as the hole, i.e. a height of $h = 0.6a$ and a radius of $r_p = 0.2a$. The substrate thickness is considered infinite, compared to the SiO_2 layer thickness and the pillars height. The air hole/Ni pillar are chosen because of their strong contrast in density and elastic constants with regard to the matrix. The first Brillouin zone (BZ) of the PnCs is shown in Fig 3.2(b). Considering the anisotropy of the quartz substrate, the irreducible BZ is a square bounded by Γ-X-M-Y-Γ.

Before meshing the unit cell, the substrate is divided equally into two parts. Subpart is responsible for damping and loss. The bottom of the substrate is assumed fixed. A three-dimensional tetrahedral mesh is used to mesh the unit cell. The size of the element for the substrate is chosen as 2 μm and that for the SiO_2 layer and pillar varies from 50 nm to 1 μm.

The complete structure is constructed by the repetition of unit cells along both directions of the basic vectors. The Floquet periodic conditions expressed in equation :

$$\vec{u_{dst}} = \vec{u_{src}} e^{-j\vec{k_F}\cdot(\vec{r_{dst}}-\vec{r_{src}})} \tag{3.1}$$

are applied on the lateral sides of the unit cell to represent the infinity of PnC, where $\vec{u_{dst}}$ and $\vec{u_{src}}$ are the displacement vectors of the destination and the source, $\vec{r_{dst}}$ and $\vec{r_{src}}$ are the vectors of the destination and the source, $\vec{k_F}$ is the wave vector. The range of $\vec{k_F}$ is the boundary of the irreducible BZ.

3.1.1 Surface modes selection

Since the eigenfrequencies of the PnCs have been calculated using a finite-depth substrate which is supposed to be semi-infinite for Love waves, Lamb modes and bulk modes appear. Therefore, the wavelength normalized energy depth (NED) [132] is

calculated to select the surface modes :

$$\text{NED} = \frac{\iiint_{\mathcal{D}} \frac{1}{2} T_{ij} S^*_{ij}(-z) dxdydz}{n\lambda \iiint_{\mathcal{D}} \frac{1}{2} T_{ij} S^*_{ij} dxdydz} \tag{3.2}$$

where T_{ij} is the stress and S_{ij} the strain. The asterisk (*) signifies the complex conjugate. $\mathcal{D}$ denotes the whole domain of the unit cell. λ is the wavelength. The surface of the PnC coincides with the plane $z = 0$. Note that the integral in the denominator is the total acoustic potential energy in the unit cell and that the integral in the numerator is weighted by the depth of the point where the acoustic energy is not zero. That means if the average depth of the energy is less than the wavelength, the NED will be less than 1. The NED can well select the modes with speed less than the SH wave velocity of the substrate, where the wave vector k is relatively large. As for a relatively small k, λ is fixed to $2a$ that is resulting from $k = \frac{\pi}{a}$ and $k = \frac{2\pi}{\lambda}$. n=1 for the holey PnC and n=1+h/λ for the pillared PnC because of the pillar height.

3.1.2 Waves polarization distinguish

Rayleigh waves comprise longitudinal and shear vertical components while Love wave is a shear horizontal (SH) wave. Surface modes include SH type SAW and Rayleigh type SAW. The ratio of SH polarization is calculated to distinguish Love waves and Rayleigh waves.

$$\text{SH ratio} = \frac{\iiint_{\mathcal{D}} u_{SH} u^*_{SH} dxdydz}{\iiint_{\mathcal{D}} (u_x u^*_x + u_y u^*_y + u_z u^*_z) dxdydz} \tag{3.3}$$

where u_x, u_y and u_z are, respectively, the displacements along the x, y, z directions. u_{SH} is the SH displacement component that can be expressed as $u_x \cos\theta - u_y \sin\theta$, which is perpendicular to the wave vector $\vec{k}$. θ is the angle between $\vec{k}$ and the y-axis with $\tan\theta = \frac{k_x}{k_y}$.

3.2 Band structures of unit cells

3.2.1 Holey PnC

band structure and displacement

The complete band structure of the holey PnC is shown in Fig 3.3. The vertical axis is the normalized frequency $\omega a/c$, where $\omega = 2\pi f$ is the angular frequency and c is the x-axis-propagating SH waves velocity (here the fast shear waves) in the substrate. The gray part is the radiation zone, where the waves diffuse to the volume (the bulk waves). The slope of the black line is the propagating velocity of the SH waves in the substrate, according to $v = \frac{2\pi f}{k}$. Black dotted lines are the dispersion curves of the shear waves in the SiO_2 layer. A mode between these two lines is a guided mode in the SiO_2 layer decaying into the substrate, and a mode below the black dotted line is an evanescent mode or a localized mode in the pillars. The branches in red and yellow denote the surface vibrating modes. With the change of propagation direction, certain modes become gray as they start to diffuse into the volume. The modes colors are determined by their SH ratio. The red modes have a large SH ratio, indicating the Love modes. The yellower the modes, the closer they are to the Rayleigh type. Thanks to the exclusive generation of SH waves in our structure (SiO_2/90ST-cut quartz) in the x direction, on the right side we only show the SH modes (SH ratio>0.5) in the ΓX region. The radiation part is uncovered to show the SH modes beyond the upper limit of the velocity (V_{SH} in substrate). It can be seen that beyond this limit, the second branch of Love modes is still confined to the surface but coupled with the bulk modes.

Since our SiO2/ST-cut quartz structure only allows the propagation of SH waves, only SH modes in the band structure will be studied. It can be seen that the modes in the holey PnC exist at high frequencies, of which two are Love modes. In the Γ-X direction, the Love waves are not coupled to the Rayleigh waves, showing a large partial Bragg band gap ranged from 2.2 to 2.75 between the two Love modes. This band gap is derived

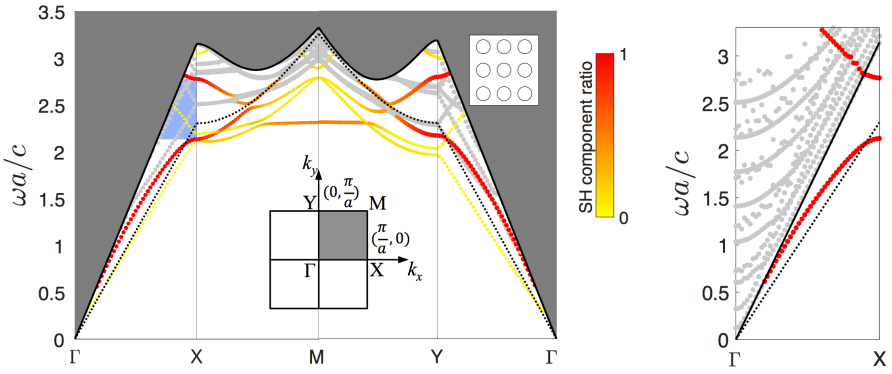

FIGURE 3.3 – (left) Complete band structures of square arrayed holey PnC. Black solid/dotted lines indicate the velocity of the SH waves in the substrate/guiding layer. Red-yellow colors denote the SH component ratio. Gray lines are the modes propagating into the volume. The blue zone indicates the partial band gap of Love modes in the x direction. C is the x-axis-propagating SH waves velocity in the substrate. (right) Band structure of SH modes in the ΓX region.

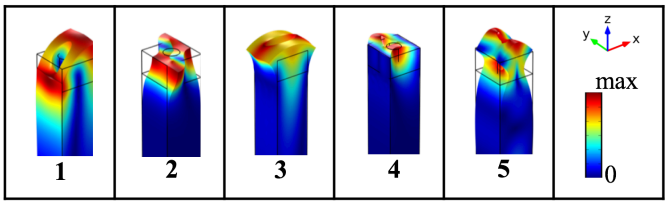

FIGURE 3.4 – Total displacements and deformations of the surface modes at point X of the BZ corresponding to the band structures of the holey PnC.

from the periodic variation of the density and elastic parameters of the inclusions (air holes) and the matrix (SiO_2).

Fig 3.4 shows the total displacements and deformations of the surface modes at point X in the irreducible BZ corresponding to the band structures of the holey PnC. The displacement direction of the unit cell reveals the waves polarization. Fig 3.5 shows the polarizations for each surface mode. The wave vector is chosen as the limit of the ΓX direction in the irreducible Brillouin zone (point X). The total displacement can be divided into 3 components u, v and w, representing the displacement in the x, y and z directions, respectively. It is observed that for the 2 modes indicated in red in the band structure of the holey PnC, i.e. the 1st and 4th modes, the polarization is along

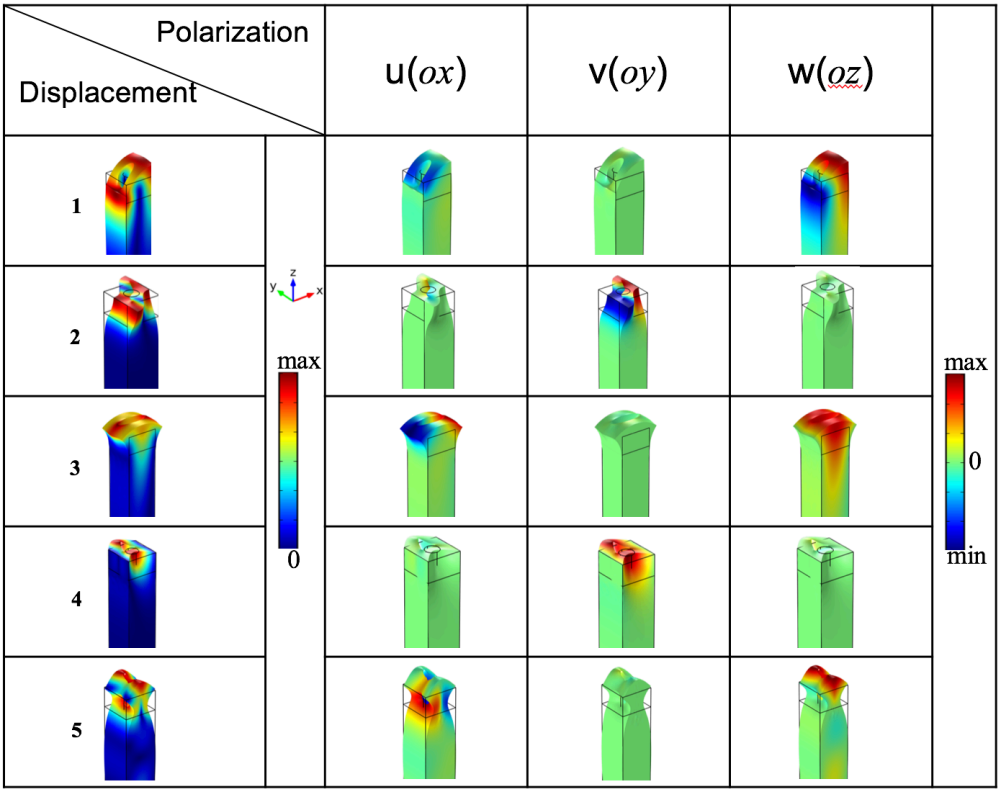

FIGURE 3.5 – Displacement components of the surface modes in the holey PnC at point X of the irreducible Brillouin zone.

the y direction as they do not have displacement component in the xz plane. Since the propagation direction of the waves is along the x axis (we are at point X), we can summarize that these two are Love modes. The other 3 modes are Rayleigh modes whose polarization is in the xz plane.

Due to the large SH polarization ratio of Love modes, as well as the exclusive generation of SH waves by the electric field in our structure, we only need to study the transverse component u_y for the SH modes.

geometrical parameters consideration

To better understand the band properties of the PnCs, we investigated the evolution of the modes with the variation of the geometrical parameters. Here for the holey PnC

are the thickness of the layer H (i.e. the holes depth) and the radius of the holes r_h. We study the effect of these parameters on the SH surface modes (SH ratio > 0.5).

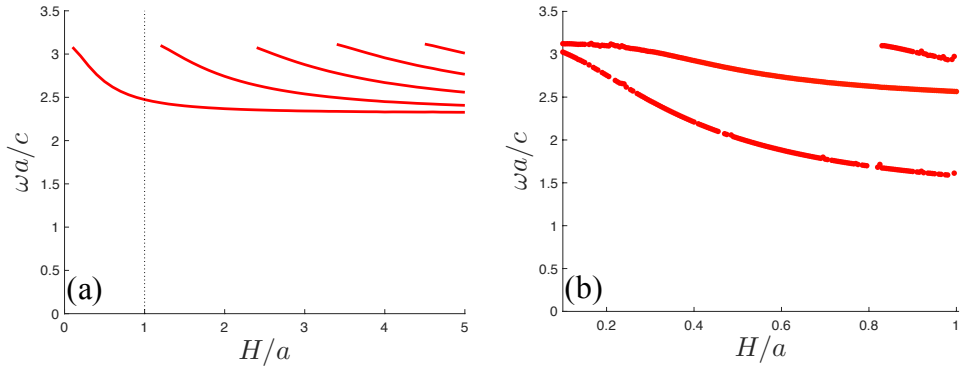

FIGURE 3.6 – Evolution of the SH surface modes normalized eigenfrequencies at the point X of the irreducible BZ by modifying the thickness of the guiding layer for (a) the square array without hole or pillar, (b) the holey PnC.

Fig 3.6 shows the evolution of the SH surface modes normalized eigenfrequencies at the point X of the irreducible Brillouin zone by modifying the thickness of the guiding layer H, for the bare square lattice (without hole or pillar) and holey PnC. The horizontal axis is the thickness of the guiding layer normalized by the lattice constant. For the holey PnC, the relative layer thickness varies from 0.1 to 1 with a step of 0.005. The other geometrical parameters remain the same : $r_h = 0.2a, a = 4\mu$m.

For the structure without hole or pillar, the Fig 3.6(a) gives the coherent dispersion relation as calculated in 2.2.3. It is found that in the interval [0.1, 1] of the normalized thickness, there is only one mode. As the layer becomes relatively thicker, modes with higher orders appear and the frequency of each mode decreases, i.e. the waves velocity of each mode becomes smaller, between the upper limit (corresponding to the SH waves velocity in substrate) and the lower limit (corresponding to the SH waves velocity in the guiding layer).

After adding holes, more modes appear due to more vibration types. To avoid the appearance of too many modes,we only study in the range [0.1, 1] of the normalized

thickness. In Fig 3.6(b) for the holey PnC, the modes still tend to decrease. it is observed that the holes have decreased the lower limit of the wave velocity, while maintaining the upper limit. This means the holes are capable of slowing down the Love waves. However, the modes remain in high frequency. The Bragg band gap between the 2 Love modes opens with the increase of the layer thickness.

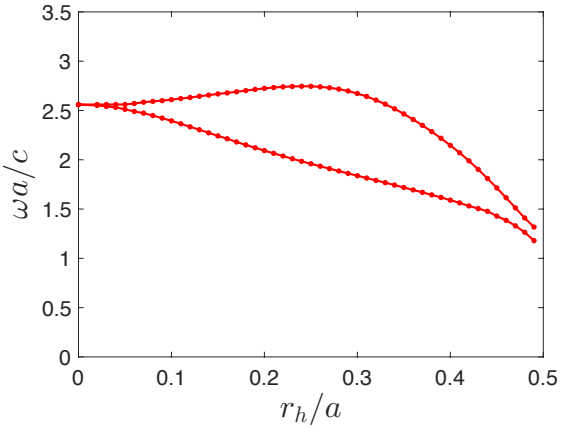

FIGURE 3.7 – Evolution of the SH surface modes normalized eigenfrequencies at the point X of the irreducible BZ by modifying the radius of the hole/pillar for the (a) holey, (b) pillared and (c) mixed lattice.

Fig 3.7 shows the evolution of the SH modes normalized eigenfrequencies at the limit of the irreducible BZ (point X) by modifying the hole radius of the holey PnC. The horizontal axis is the radius normalized by the lattice constant. Other geometrical parameters are fixed : $H = 0.6a$ and $a = 4\mu$m. Bragg band gap is between the two Love modes for the holey PnC. This band gap opens and then closes with the increase of the hole radius, which directly affects the filling factor. the band width reaches a maximum at r/a=0.29. Since the center of the band gap tends to decrease with the increase of the normalized radius, the relative band width ($\Delta f/f_{center}$) reaches its maximum (37.1%) at r/a=0.31. Note that this is a partial band gap at the direction ΓX.

3.2.2 pillared PnC

band structure and displacement

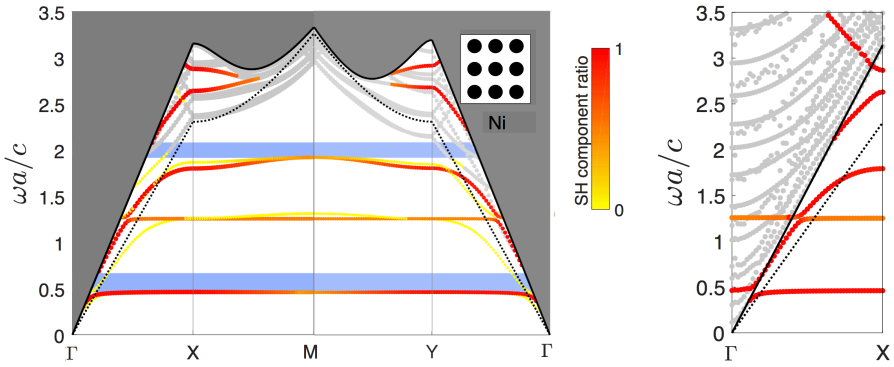

FIGURE 3.8 – (left) Complete band structure of the pillared PnC. Blue zones indicate the complete band gaps. (right) Band structure of SH modes in the γX region.

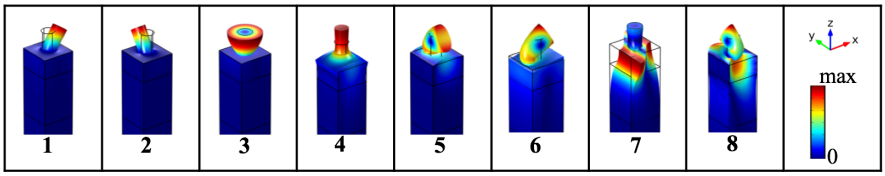

FIGURE 3.9 – Total displacements and deformations of the surface modes at point X of the BZ corresponding to the band structures of the pillared PnC.

The band structure of the pillared PnC is shown in Fig 3.8. Compared with the holey PnC, more modes are observed. Corresponding total displacement fields and deformations for the modes at point X are shown in Fig 3.9. The first 6 are local resonant pillar modes. The first two are flexion modes along x and y directions, respectively. The 3^{rd} is a torsion mode in $x-y$ plan and the 4^{th} a tensile mode along z-axis. The torsional motion of the 3^{rd} mode can be verified by the corresponding U_y component of Love modes shown in Fig 3.10. Since the displacement of torsion mode has also a U_x component, this mode is denoted in orange. The 5^{th} and 6^{th} are mixed modes composed of expanding and flexion modes. At higher frequencies, there are two Love modes guided in the layer and coupling with pillars. These two modes give rise to a partial Bragg band

gap that is due to the periodicity of the pillared PnC. This Bragg band gap is much narrower than that generated by the holey PnC. Note that the pillars generate complete band gaps for Love waves, in the ranges of (0.45, 0.7) and (1.9, 2.1). These complete band gaps are of local resonance type, which result from the coupling of the individual pillar and the progressive SH waves.

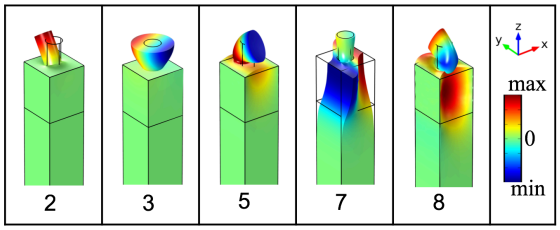

FIGURE 3.10 – u_y of SH surface modes at point X for the pillared lattice.

geometrical parameters consideration

Besides the guiding layer thickness H and the inclusion radius (here the pillar radius r_p), the pillared PnC has a new geometrical parameter (the pillar height h) compared with the holey PnC. We studied the effects of these three geometrical parameters on the SH surface modes.

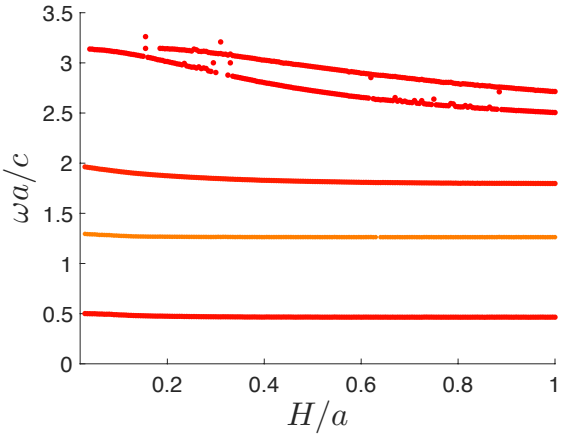

FIGURE 3.11 – Evolution of the SH surface modes normalized eigenfrequencies at the point X of the irreducible BZ by modifying the guiding layer thickness H of the pillared PnC.

In Fig 3.11, SH surface modes normalized eigenfrequencies at the point X are shown as functions of the normalized guiding layer thickness H/a of the pillared lattice. Other geometrical parameters remain fixed : $r_p = 0.2a, h = 0.6a, a = 4\mu$m. Two guiding Love modes at higher frequency range tend to decrease with the increase of the silica thickness. However, the partial Bragg band gap width defined by these two modes at point X has not much changed after H/a exceeding 0.3. On the other hand, the 3 pillar modes at lower frequency (there are 3 SH modes among the 6 pillar modes) are little affected by the evolution of the guiding layer, since they are dominant by the intrinsic vibration of the pillar.

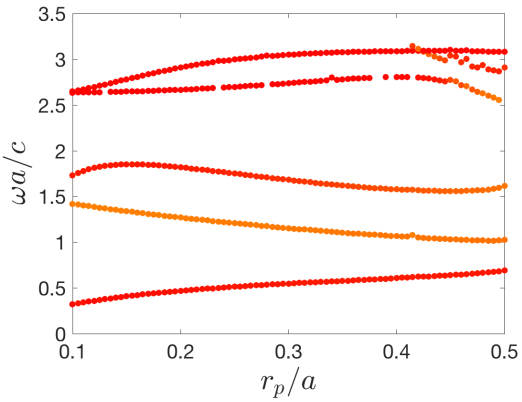

FIGURE 3.12 – Evolution of the SH surface modes normalized eigenfrequencies at the point X of the irreducible BZ by modifying the pillar radius r_p of the pillared PnC.

Fig 3.12 shows the evolution of the SH surface modes normalized eigenfrequencies at the point X by modifying the pillar radius of the pillared lattice, with other geometrical parameters fixed : $h = 0.6a, H = 0.6a, a = 4\mu$m. In the high frequency range, two Love modes guided in the SiO_2 layer give rise to the partial Bragg band gap at the direction ΓX. This band gap opens with the increase of hole radius before r_p/a reaching 0.3. Then the band width remains almost unchanged before r_p/a=0.4. At lower frequency, the 1^{st} SH pillar mode (flexion mode) increases while the 2^{nd} SH pillar modes (torsional mode) decrease, with the increase of the radius. The 3^{rd} SH pillar mode tends to decrease in

the normalized pillar radius range of [0.15, 0.45].

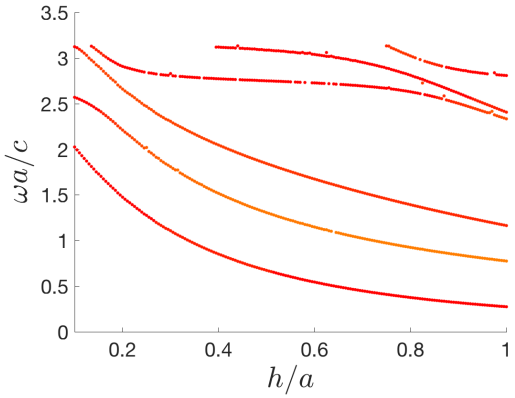

FIGURE 3.13 – SH surface modes normalized eigenfrequencies at the point X as functions of the normalized pillar height of the pillared PnC.

Fig 3.13 shows the evolution of the SH modes normalized eigenfrequencies at the point X by modifying the pillar height of the pillared PnC. The horizontal axis is the pillar height normalized by the lattice constant. Other geometrical parameters keep fixed : $r_p = 0.2a, H = 0.6a, a = 4\mu$m. The first 3 are pillar modes and the others are guiding modes coupled with pillars. Guiding modes begin to appear for different heights. It can be seen that the evolution of the pillar height causes a tendency of decreasing the eigenfrequencies of all the modes, since these modes are all dependent on the pillar's vibration. Nevertheless, the detailed tendency of the pillar modes do not resemble those of the guiding modes in terms of the curve slope.

materials consideration

As we have introduced above, the PnCs are the periodic structures of elasticity or mass, and the phononic band gap is highly dependent on the contrast in physical properties (elasticity, density and acoustic velocity). Therefore, it is meaningful to study the materials of PnCs.

To simplify the model, both of the matrix and inclusions materials are considered

isotropic. ρ and E are the density and Young's modulus. The subscript i and m represent inclusions and matrix. It is known that the formation of a band gap of PnC is due to the diffraction of the phonons that propagate in a crystal at the interface between the matrix and the inclusions. The acoustic impedance of a material is :

$$Z_{i,m} = sqrt(\rho_{i,m} E_{i,m}) \tag{3.4}$$

The propagating velocity in a material is :

$$V_{i,m} = sqrt(E_{i,m}/\rho_{i,m}) \tag{3.5}$$

In the following part, the composition of the material will be discussed. Gold, diamond and silicon are chosen respectively because of their high density, high Young's modulus and facility of manipulation, relative to nickel. The guiding layer is SiO_2. The density and Young's modulus for diamond, silicon, nickel, gold, and SiO_2 are shown in Table 3.1. Fig 3.14 shows the band structures for the square lattice based on diamond, Si, Ni, and Au pillars. The geometrical parameters are the same : $r_p = 0.3a, h = 0.6a, H = 0.6a, a = 4\mu$m, with r_p, h, H, a respectively the pillar radius, the pillar height, the guiding layer thickness and the lattice constant.

/	Diamond	Si	Ni	Au	SiO_2
Density ρ(kg/m^3)	3520	2329	8900	19300	2200
Young's modulus E(GPa)	1220	170	219	70	70
Acoustic velocity V(m/s)	18617	8543	4960	1904	5640

Tableau 3.1 – Relative physical properties of different materials

Diamond studs have relatively high eigenfrequencies, since its acoustic velocity is the highest due to a great Young's modulus. The first 3 modes are the same as the first 3 pillar modes that we have discussed. In the higher frequency range, where the normalized frequency> 2, there are 3 surface modes guided in the layer and coupled

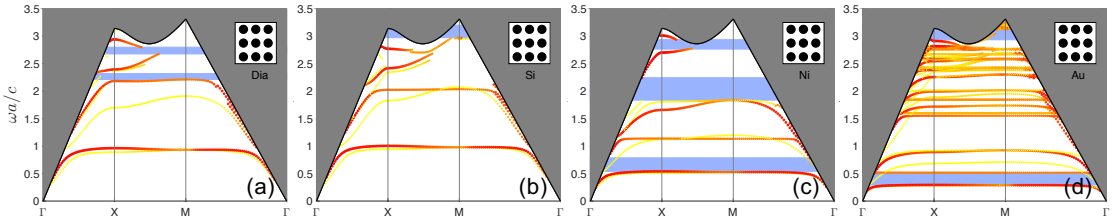

FIGURE 3.14 – Band structures of phononic crystals based on (a) diamond, (b) silicon, (c) nickel and (d) gold pillars. Blue zones denote the band gaps in the Γ-X-M-Γ region of the BZ.

with the pillar.

Gold pillars have lower eigenfrequencies due to its lower acoustic velocity, and therefore more eigenmodes can be excited. The first 6 modes are the pillar modes that have been studied. Nevertheless, at higher frequency range, the guiding modes in the layer are mixed with the pillar modes of higher orders.

The eigenfrequencies is found to be proportional with the Young's modulus and anti-proportional with the density, and is therefore proportional with the acoustic velocity. That is, a soft and heavy material helps to obtain lower eigenfrequencies. Additionally, we observe that the modes are very flat in the band structure for the gold pillar, which means a high Q factor.

3.3 Transmission spectrum

The band structures show the intrinsic properties of PnCs, such as the resonances and the polarizations. However, these results are calculated for the ideal infinite models. Therefore, it is necessary to calculate the transmission spectra of finite 3D PnCs to confirm the theoretical results obtained by the band structures. Moreover, the transmission spectra also help to better understand the band structures.

3.3.1 Transmission model

The calculation of transmission spectra is realized by simulating a SAW device consisting of two parts of aluminum inter-digital transducers (IDTs) and a PnC located between the IDTs. The height of IDTs is h_{IDT} = 200nm. The IDTs are constructed on the quartz surface which is piezoelectric to generate the electric field. The graphic representation of the model is shown in Fig 3.15, here we take the holey PnC as an example. Since the device has translational symmetry along the y-axis which is perpendicular to the direction of propagation, periodic boundary conditions are applied along the y-axis, reducing the simulation structure to only one period. The model is surrounded by perfectly matched layers (PMLs) for absorbing the undesired reflections from the boundary. The bottom and lateral sides are assumed fixed. One of the IDTs performing as a transmitter is given a harmonic voltage signal, with an amplitude of $1V$, to excite acoustic waves in the quartz substrate. These waves are confined in the silica film and propagate through the PnC. They are received by the IDT on the other side. The output is measured by averaging the voltage difference between the odd and even fingers. The odd fingers of the input and output IDTs are assigned to the electrical ground. The even fingers of the output IDT are set to zero surface charge accumulation. Note that the width of the IDT fingers L_{IDT} should be updated for each frequency in the spectrum according to the relation $L_{IDT} = \frac{\lambda}{4} = \frac{v}{4f}$. v is the velocity of Love waves for $H = 0.6a$, resulting from the basic dispersion relation of Love waves. That is, each frequency corresponds to a single wave velocity and wavelength. This model has been validated in the previous work[106] by giving coincident results between simulations and experiments.

3.3.2 Transmission spectrum for holey PnC

Fig 3.16(b) shows the transmission spectrum of the holey PnC, calculated with 10 PnC holes in center and 20 IDT fingers on each side. This frequency response is then normalized by that of the matrix (without PnC), referred to as normalized or

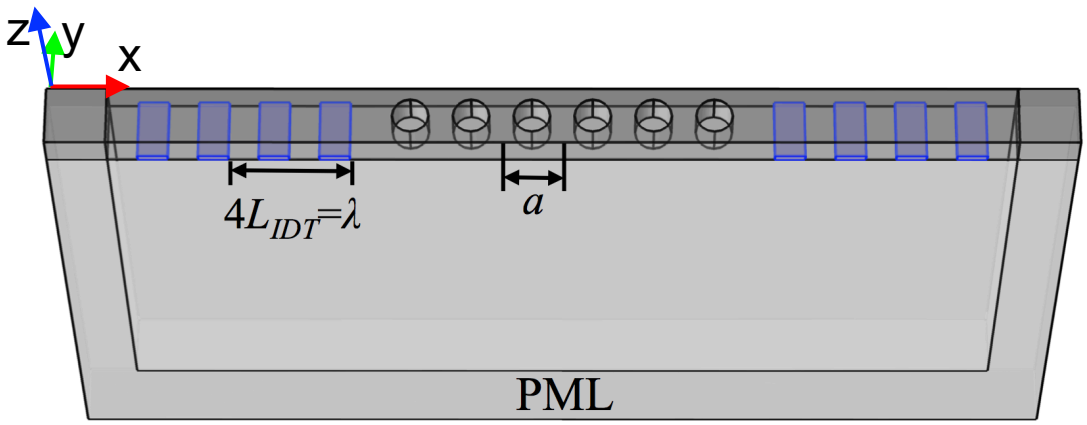

FIGURE 3.15 – Schematic of the SAW device model for calculating the transmission spectra of Love waves through the holey PnC. $r_h = 0.2a$, $H = 0.6a$, $a = 4\mu$m

relative transmissions ΔS_{21}, to show the transmission loss contributed by the PnC only in Fig 3.16(c). The band structure of SH modes around the band-gap zone in the ΓX direction is shown aside. The transmission attenuation appears clear and is consistent with the band structure prediction. It can be seen that the Love modes at higher frequency continues to propagate even after exceeding the limit of the substrate velocity due to a good confinement to the surface.

3.3.3 Transmission spectrum for pillared PnC

The transmissions of Love waves through the pillared lattice are shown in Fig 3.17. We can see that the band structures are compatible with the normalized transmission spectra. It is observed that the hybridization bands at lower frequency give rise to sharp transmission attenuations because of the waves resonant scattering in the pillars. The Bragg band gaps at higher frequency arouse wide attenuation, which come from the periodicity of the PnC.

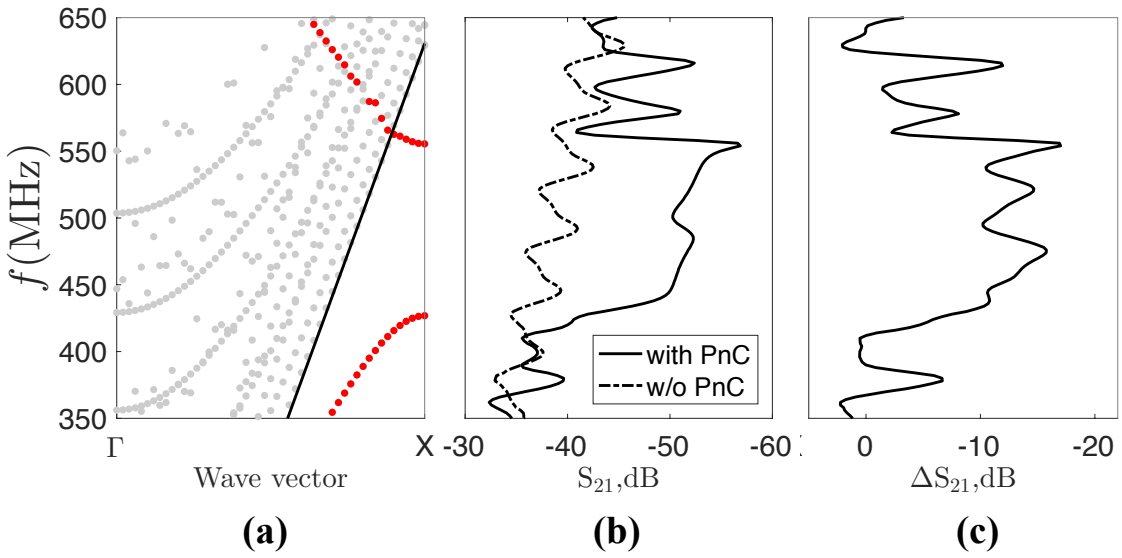

FIGURE 3.16 – (a)Zoom of the band structure of SH modes around the band-gap zone in the ΓX direction of the holey PnC; (b)Transmission and (c) Normalized transmission spectra of Love waves propagating through the holey PnC around the band-gap zone. $r_h = 0.2a$, $H = 0.6a$, $a = 4\mu$m, $N_{PnC} = 10$.

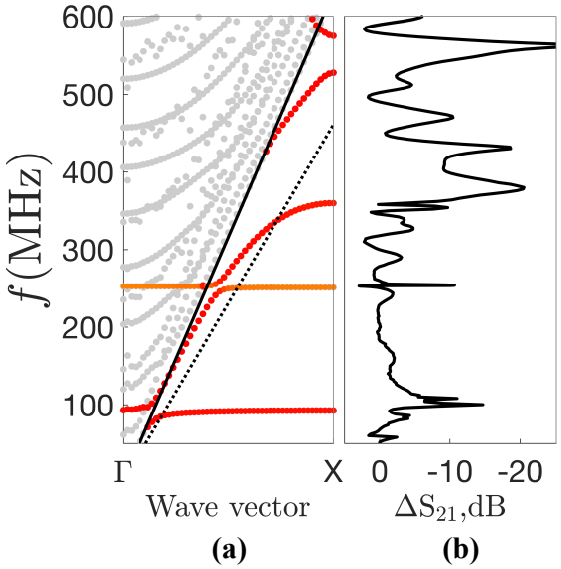

FIGURE 3.17 – (a) Band structure of SH modes in the ΓX direction of the pillared PnC. (b) Normalized transmission spectrum for the pillared PnC. $r_p = 0.2a, h = 0.6a, H = 0.6a, a = 4\mu$m, $N_{PnC} = 10$.

3.4 Mixed lattices

After studying the holey and pillared PnCs separately, it is interesting to consider a lattice with mixed holes and pillars to see if we only obtain the simple combined resonant properties.

3.4.1 Design 1

Band structure and displacement

Firstly, we design a mixed lattice in which the holes/pillars are located at the corners of the unit cell of the pillared/holey PnC, as shown in Fig 3.18. The holes and pillars are respectively arranged in square array. We refer to this lattice as D-PnC since the holes and pillars alternate along the diagonal of the unit cell.

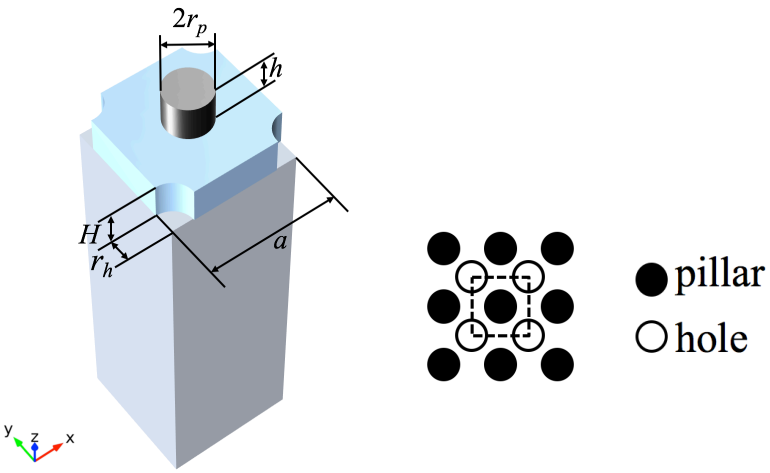

FIGURE 3.18 – Unit cell of the D-PnC. Corresponding schematic of the lattice is shown on the right side. r_h=r_p=0.2a, h=0.6a, H=0.6a, a = 4μm.

The complete band structure of the D-PnC is shown in Fig 3.19. SH modes in the x direction is shown on the right side of the complete band structure. The total displacement fields of the surface modes at point X are shown in Fig 3.20. The displacement of the SH surface modes have the behaviors similar to that of the pillared PnC, therefore

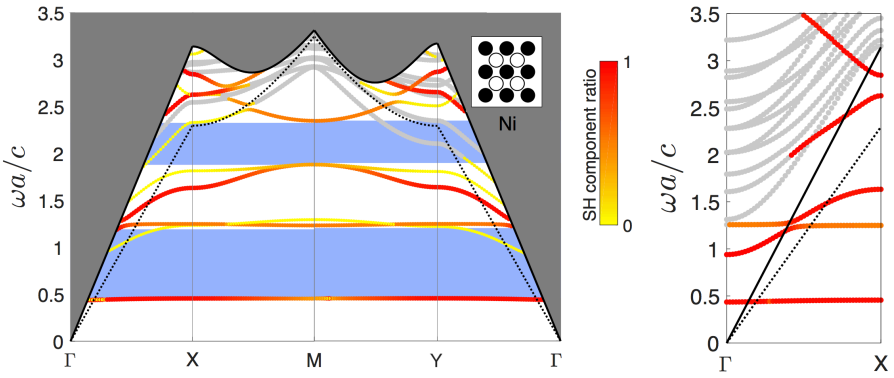

FIGURE 3.19 – (left) Complete band structures of the D-PnC. Blue zones denote the complete band gaps. (right) Band structure of SH modes in the ΓX region.

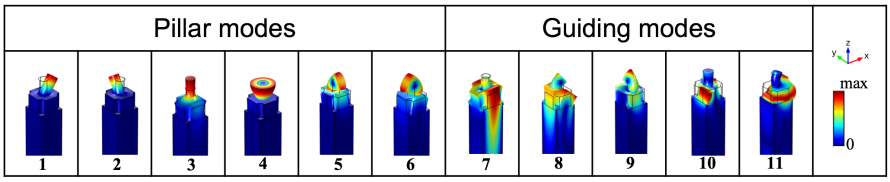

FIGURE 3.20 – Total displacements and deformations of the surface modes at point X of the BZ corresponding to the band structures of the D-PnC.

we will not show their U_y component here. It can be seen that when holes and pillars are mixed, the surface eigenmodes bloom in high and low frequencies. It is found that the mixed lattice contains both the effects of the holes and pillars. The 6 pillars modes at low frequencies still remain. However, in comparison with the pillared PnC, a downward frequency shift of the 3^{rd} SH surface mode (the 5^{th} pillar mode) is observed. It is because that the interaction between the guiding layer and the pillar is more intensive for this mode than the first two SH surface modes. Therefore this mode is more sensitive to the change of guiding layer. Moreover, more guiding modes are confined to the surface due to the holes effect. That is, thanks to the holes, the bulk modes that are filtered out by equation 3.2 and appear gray in the band structure of the pillared PnC (Fig 3.8), become surface modes in the D-PnC. The width of the partial Bragg band gap (in the ΓX direction) between the 2 Love modes at high frequency is almost the same as that of the pillared PnC. However, the complete band gaps become much wider, which results

from the increased frequencies at Γ point of all the progressive SH modes (bulk and surface). This phenomenon also leads to a higher frequency for the appearance of the first guiding mode.

We can conclude that the Bragg band gap is partial in the x direction. The pillars can give rise to complete band gaps, while the holes can promote the confinement of guiding modes. The D-PnC has widened the band gaps.

Geometrical parameters consideration

The evolution of the SH surface modes with the variation of the geometrical parameters (H, r and h) are shown in Fig 3.21. Here we set $r_h = r_p = r$. Compared with the pillared PnC, the mode eigenfrequencies of the D-PnC evolve in much the same way for each case. However, it is worth noting some slight differences :

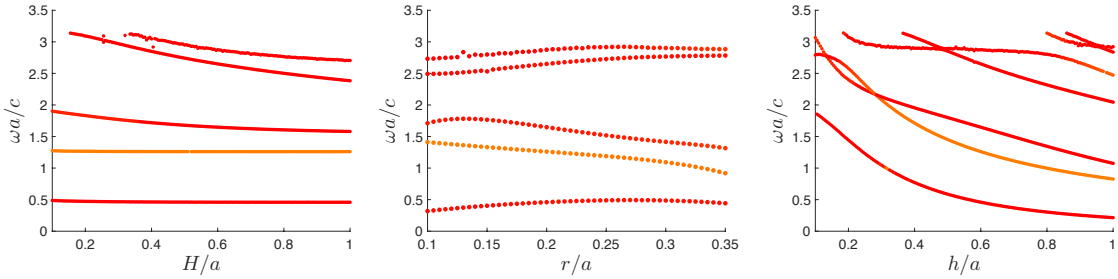

Figure 3.21 – Evolution of the SH surface modes normalized eigenfrequencies at the point X of the irreducible BZ by modifying (a) the guiding layer thickness, (b) the hole/pillar radius and (c) the pillar height of the pillared PnC. The parameters are fixed when they are not the ones being changed : $r_h = r_p = 0.2a, h = 0.6a, H = 0.6a, a = 4\mu$m.

•For the mode frequencies as functions of the guiding layer thickness H (Fig 3.21(a)) : (1) The 3^{rd} pillar mode is more sensitive to the guiding layer evolution when the thickness is relatively small (H/a<0.6). (2) The 2 guiding modes appear in a thicker layer, at H/a=0.15 and 0.35 respectively, compared with H/a=0.01 and 0.2 for the pillared PnC, respectively.

•For the mode frequencies as functions of the hole/pillar radius r (Fig 3.21(b)) : (1)

The partial Bragg band gap closes with the increase of the hole/pillar radius, while the Bragg band gap opens with the increase of the pillar radius for the pillared PnC. (2) The upper limit of the normalized radius becomes 0.35 due to a construction limitation.

•For the mode frequencies as functions of the pillar height h (Fig 3.21(c)) : (1) Certain modes in the mixed lattice meet and cross, i.e. at the point of intersection, the polarization of the two modes occurs simultaneously. This is the case for both the local resonant pillar modes and the guiding modes. (2) The guiding modes begin to appear for different pillar heights compared with the pillared PnC.

Transmission spectrum

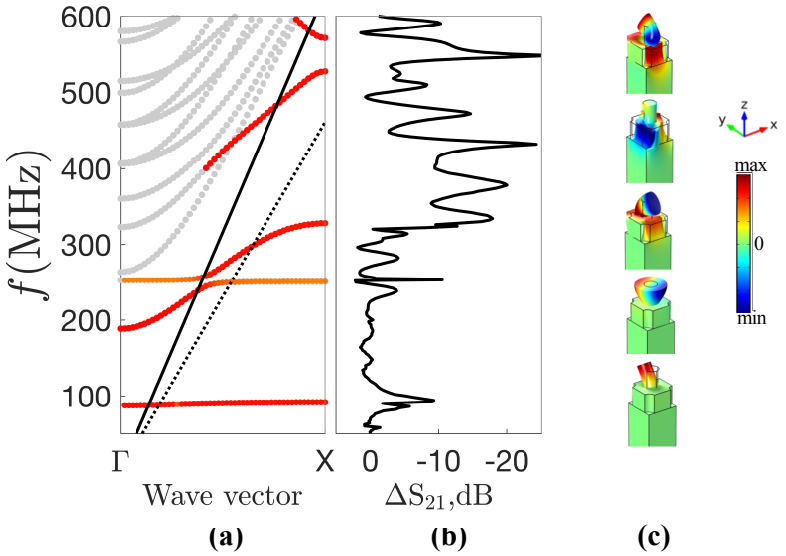

FIGURE 3.22 – (a) Band structure of SH modes in the ΓX direction for the D-PnC. (b) Normalized transmission spectrum of Love waves propagating through the D-PnC. (c) Displacement field u_y of SH surface modes at point X. $r_h = r_p = 0.2a, h = 0.6a, H = 0.6a, a = 4\mu\text{m}, N_{PnC} = 10$.

The transmissions of Love waves through the D-PnC are shown in Fig 3.22. Similar as the second surface SH mode branch of the holey PnC case, a short part of the surface SH mode beyond the black line (red part of the 4^{th} branch) can still propagate. Another

point to note is that the first branch is flat since the SH progressive wave starts to be guided in the silica layer at a higher frequency, compared with the pillared PnC. This single flat branch, denoting the pillar flexion mode, still gives rise to a transmission attenuation because of the waves scattering in the pillars.

3.4.2 Design 2

Since the 2^{nd} SH surface mode (pillar torsional mode) can give rise to a sharp dip in the transmission spectrum of Love waves, it is conceivable to reset this mode into the band gap of the holey PnC to see the coupling results. Therefore, we halve the pillar size to double the torsional mode frequency, namely $r_p = 0.1a$ and $h = 0.3a$. The hole size remains the same : $r_h = 0.2a$, $H = 0.6a$ and $a = 4\mu$m. The lattice arrangement is the same as the D-PnC. We refer to this lattice as Ds-PnC.

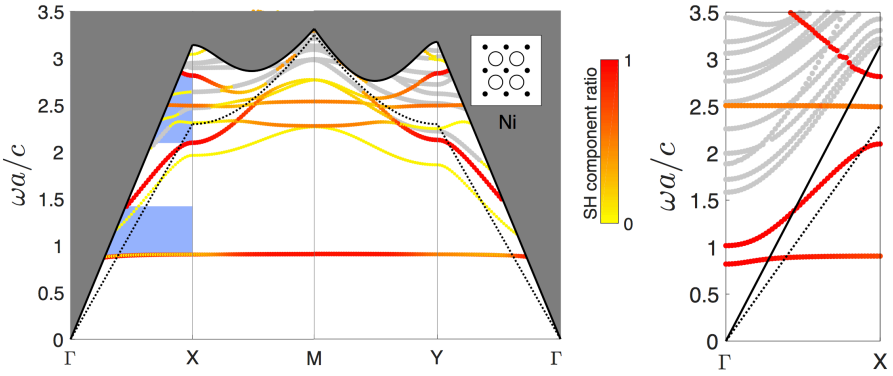

FIGURE 3.23 – (left) Complete band structures of the Ds-PnC. Blue zones denote the partial band gaps in the ΓX direction. (right) Band structure of SH modes in the ΓX direction.

The band structure of the Ds-PnC is shown in Fig 3.23. It can be seen that the pillar mode frequencies are doubled due to the halved pillar size compared with the D-PnC. The second local resonant mode (torsional mode, around 500 MHz) has been modified to the medium of the partial band gap. Another point to be noted is that this structure maintains the increased frequencies of the progressive SH modes at the Γ point. The

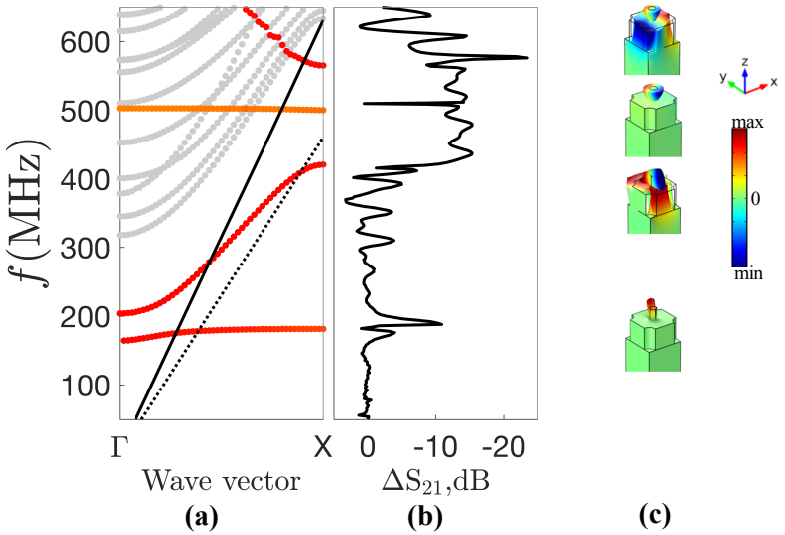

FIGURE 3.24 – (a) Band structure of SH modes in the ΓX direction for the Ds-PnC. (b) Normalized transmission spectrum of Love waves propagating through the Ds-PnC. (c) Displacement field u_y of SH surface modes at point X. $r_p = 0.1a, r_h = 0.2a, h = 0.3a, H = 0.6a, a = 4\mu\text{m}, N_{PnC} = 10$.

transmission spectrum of Love waves propagating through the Ds-PnC is shown in Fig 3.24. In the lower frequency range, the flexion mode (around 180 MHz) raises a small hybridization band gap due to the waves scattering in the pillars. Nevertheless, different from the above results, the torsional mode here gives rise to a sharp transmission peak. This can be understood as the pillar is a secondary source that also generates waves by vibrating. The details of this phenomenon will be discussed in chapter 5.

3.4.3 Design 3

Based on the Ds-PnC, we changed the relative position of the holes and pillars to make them alternate in a line that parallel to the propagation direction, as shown in Fig 3.25. We refer to this lattice as Ls-PnC.

The band structure of the Ls-PnC is shown in Fig 3.26. It can be seen that the increased frequencies of the SH modes at point Γ are canceled. As a result, the guiding mode appears at the original frequency (close to zero). The transmission spectrum of

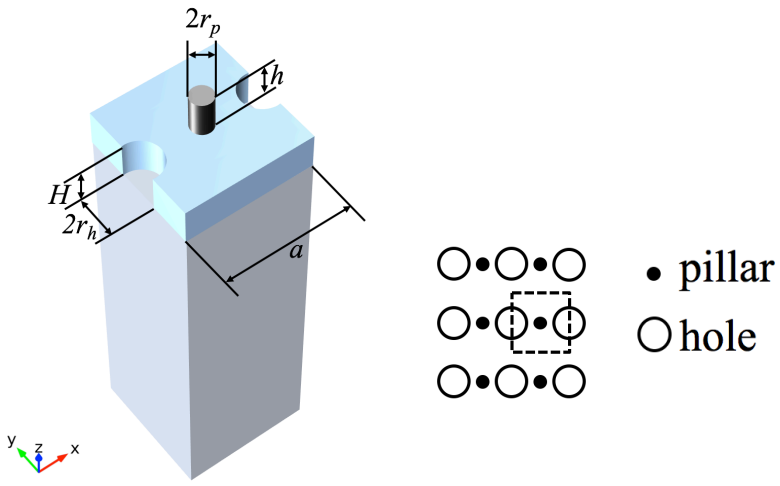

FIGURE 3.25 – Unit cell of the Ls-PnC. Corresponding schematic of the lattice is shown on the right side. $r_p = 0.1a, r_h = 0.2a, h = 0.3a, H = 0.6a, a = 4\mu$m

the Ls-PnC (in Fig 3.27) is almost the same as that of the Ds-PnC despite their different dispersion curves of SH surface modes in the lower frequency range.

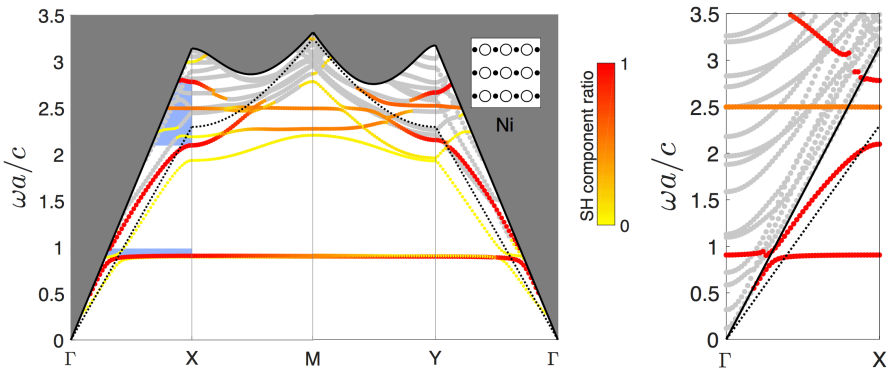

FIGURE 3.26 – (left) Complete band structures of the Ls-PnC. Blue zones denote the partial band gaps in the ΓX direction. (right) Band structure of SH modes in the ΓX direction.

By comparing the transmission spectra corresponding to the first pillar mode (flexion mode) for the three mixed lattices (D-PnC, Ds-PnC and Ls-PnC), we find that this mode always gives rise to a transmission dip even when it is isolated. This is because the waves scattering by the local resonant mode is independent of the lattice symmetry.

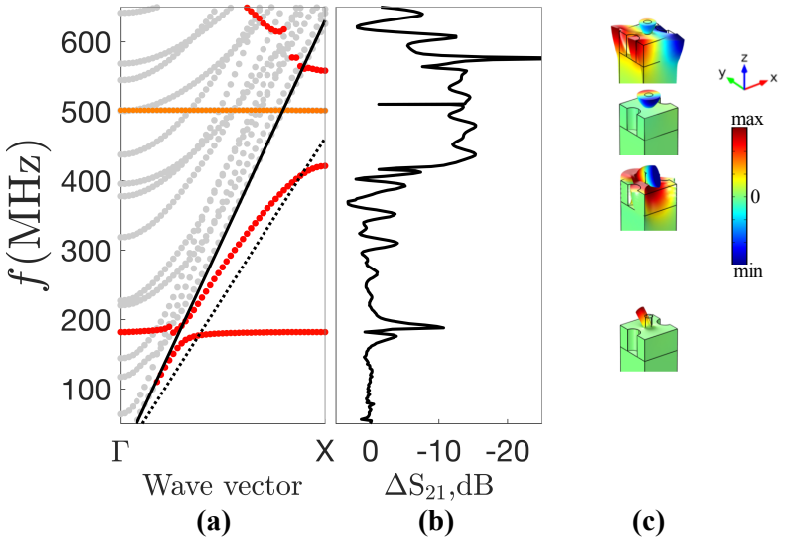

FIGURE 3.27 – (a) Band structure of SH modes in the ΓX direction for the Ls-PnC. (b) Normalized transmission spectrum of Love waves propagating through the Ls-PnC. (c) Displacement field u_y of SH surface modes at point X. $r_p = 0.1a, r_h = 0.2a, h = 0.3a, H = 0.6a, a = 4\mu\text{m}, N_{PnC} = 10$.

3.5 conclusion

This chapter describes the theoretical models built with the FEM using COMSOL software in order to study the band structures and transmission spectra of different PnCs interacting with Love waves. Normalized energy depth (NED) is calculated to select the surface waves, as well as the shear horizontal (SH) displacement component ratio to distinguish Love waves from SAW.

Firstly, band structures for square arrayed holey and Ni pillared PnCs were studied on a guiding layer of SiO_2 constructing on a 90ST quartz substrate. Displacements and deformations of surface eigenmodes are provided. The different polarizations of the modes have been observed and explained, which are consistent with the results calculated by equations (NED and SH ratio). The holey PnC gives rise to two widely separated Love modes at the X point of the irreducible Brillouin zone, denoting a large partial Bragg band gap for Love waves in the x direction. The pillared PnC arouses three

pillar SH modes below the frequencies of two narrowly separated guiding modes at the X points, corresponding to three absolute hybridization band gaps below a small partial Bragg band gap for Love waves.

Then, the effects of geometrical parameters and elastic parameters (different materials) on PnC band gaps were proposed and analyzed. For the holey PnC, Love mode frequencies decreases with the increase of guiding layer thickness, similar as the case for the homogeneous matrix (without hole). The holes are capable of slowing down the Love waves. The hole radius variation leads to the open and close of the Bragg band gap. For the pillared PnC, The guiding layer thickness can nearly not affect the pillar mode frequencies, since the latter result from the intrinsic vibration of the pillar. With the increase of pillar radius, the first SH mode (flexion) frequency increases while the other two pillar SH modes (torsion and mixed modes) frequencies decrease. However, all the three pillar mode frequencies decrease with the increase of pillar height. By changing the pillar materials to diamond, Silicon and gold, we showed that a lower acoustic velocity leads to lower mode eigenfrequencies.

Next, a SAW device model is built to calculate Love waves transmissions through different PnCs. The effect of the band gaps elicited the absorption intervals in the transmission spectra. The transmissions are compatible with the band structures of the PnCs. Love modes above the transverse velocity of the substrate can still be excited.

By combining and adjusting the holey and pillared PnC, we demonstrated that the mixed PnC has a capacity to enlarge the band gap (D-PnC) or to generate isolated mode in the band gap (Ds-PnC and Ls-PnC). An upward shift of the progressive SH modes were observed when the holes and pillars alternate along the diagonal of the unit cell (D-PnC and Ds-PnC), resulting in a higher frequency for the appearance of the guiding mode. The first two local resonant SH modes are proved independent of the lattice symmetry.

This chapter provides a study for the infinite PnCs which serves as the basis of design

for the acoustic resonators in next chapters.

Chapitre 4

Surface Local Resonators

Acoustic Local resonators are individual particles giving intrinsic vibrations at a relative low frequency range compared to the Bragg band gap. In this chapter, we use the pillars as local resonators. Although the periodicity is not a requirement, these pillars are generally regularly arranged, leading to the appearance of Bragg scattering. Phononic pillared meta-surface is a recently proposed structure that stems from the pillared phononic crystals. It consists of a single or a line of pillars on top of a slab, with which one can thoroughly investigate the pillar resonant properties without considering the Bragg scattering. The pillar size, periodicity and the slab thickness are all sub-wavelength-scaled[195, 196]. Several studies have been devoted to the interaction of pillared meta-surface with Rayleigh waves [136] and Lamb waves [187, 197], but no work has been done on Love waves.

Electromagnetically induced transparency (EIT) is a well-known physical effect in atomic systems that arise because of quantum destructive interferences between two excitation pathways to an upper atomic level [198]. Steep dispersion and low absorption take place in a sharp transparency window, which makes it very attractive for a plenty of potential applications in slowing light, enhancing optical nonlinearity and data storage [199–201]. Autler–Townes splitting [202] (ATS) which is the field-induced splitting of

the optical response, is not associated with interference effects and has been described as an incoherent sum of two Lorentzians [203]. EIT and ATS may phenomenologically look similar, but they are different in nature, one being a quantum interference and the other a linear alternating current (AC) Stark effect. EIT and ATS were first observed in quantum/atom systems[202, 204]. In recent years, classic analogues of EIT and ATS have attracted increasing interest in platforms such as photonics [205–207], optomechanics [208–210], plasmonics [163–165] and metamaterials [211–213]. Many discussions have been devoted to their easily confused absorption or transmission spectra.[205, 214–216] Besides their differences in the physical mechanisms, the Akaike Information Criterion (AIC) has been proposed to quantitatively discern EIT from ATS,[214] and the transition from ATS to EIT is thereby carried out.[217] A crossover from EIT to ATS has been shown to exist in hot molecules[218], and in open ladder systems[219]. In acoustic, the analogue of EIT, also referred to as AIT, has been investigated in different structures[220–224], but the analogue of ATS and its comparison with AIT is only recently reported[183]. Additionally, the distinction and transition between acoustic analogue of ATS and AIT has not been quantitatively investigated before.

This chapter will investigate the interaction of Love waves with the pillared metasurface. We show that these simple structures present different properties related to condensed matter physics such as transmission zeros, Fano interference, acoustic analogue of Autler-Townes Splitting(ATS), cavity modes and acoustically induced transparency (AIT). These results should have important consequences for potential acoustic applications such as wave control, designing of meta-materials and bio-sensors.

4.1 resonant properties of single pillar line

Since a sharp hybridization band gap is found for the 2^{nd} SH mode in the pillared PnC around 250 MHz, see Fig 3.17, we halved the pillar size to obtain a resonance around 500

MHz.Namely, the pillar radius, height and lattice constant is $r_p = 0.2a_p, h = 0.6a_p$, and $a_p = 2\mu$m, respectively. The thickness of SiO_2 layer remains unchanged, i.e. $H = 2.4\mu$m. Love waves propagate along the x-axis. Although H/a_p has increased, which refers to a decrease in normalized frequencies of the guiding modes, the Bragg band gap still stays beyond the pillar modes, see Fig 3.11. In this way we can investigate the pure resonance properties of the pillars even if they are periodic along the x direction.

Here firstly, we construct a supercell corresponding to a meta-surface of one single pillar line perpendicular to the propagating direction, as shown in Fig 4.1. The period along the y-axis is $a_p = 2\mu$m. The length of the unit cell L is $20a$ to insure a decoupling between the unit cells. Floquet periodic boundary conditions are applied along the x and y directions. The surfaces of the pillars coincide with the plane $z = 0$. The bottom of the substrate is assumed fixed.

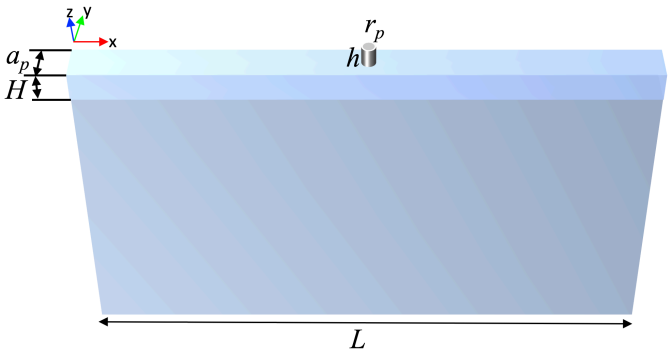

FIGURE 4.1 – supercell of one line of cylindrical Ni pillars on the SiO_2 film deposited on a 90ST-cut quartz. The period is a_p along the y direction. Love waves propagate along the x-axis. r_p=$0.2a_p$, $h = 0.6a_p$, H=2.4μm, L=$20a_p$, $a_p = 2\mu$m.

Corresponding SH modes (SH ratio>0.5) band structure in the x direction is shown in Fig 4.2(b). The modes colors are determined by their NED values (λ in the eq. 3.2 is still fixed at 8μm). The modes in red are well confined to the surface, and can therefore be excited by Love waves. Certain modes become pink as they are less confined to the surface. Two hybridization band gaps are observed respectively in the frequency range [177.3, 183.1] MHz and [501.8, 503.3] MHz, indicated in blue, which originates from the

coupling of local resonant pillar modes and the SH SAW. Note that in the frequency range [100, 600] MHz, the wavelength ranges from 6.8 to 48.8μm. Therefore, our structure is indeed a meta-surface with sub-wavelength-scaled pillar size, periodicity and guiding layer thickness.

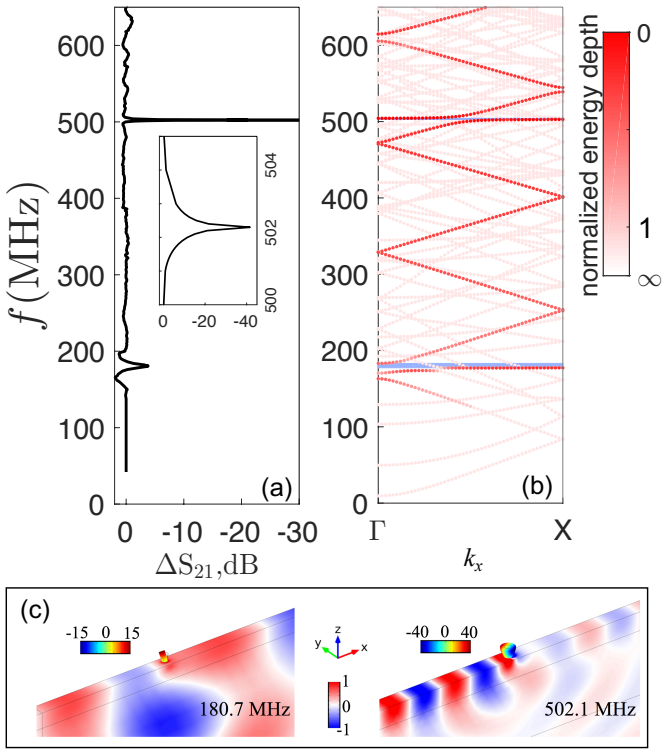

FIGURE 4.2 – (a) Transmission spectrum of Love waves propagating through a single pillar line. Inset is the zoom of the torsional mode induced dip. (b)Band structure of SH modes in ΓX direction for the unit cell of a single pillar line. The red-white colors denote the normalized energy depth. A mode in red can be excited by Love waves. (c) u_y component of the displacement fields for two local resonant pillar modes. The amplitudes in the pillar are normalized to the maximum amplitude in the SiO_2 film. $r = 0.2a_p$. $h = 0.6a_p$, $a_p = 2\mu$m.

The transmission spectra is calculated by simulating the same dispersive SAW device introduced in Ch 3, with the supercell located between IDTs. The relative transmission is denoted as ΔS_{21}. Fig 4.2(a) shows the transmission spectrum of the single pillar line. It can be seen that the transmission spectrum corroborates well with the band

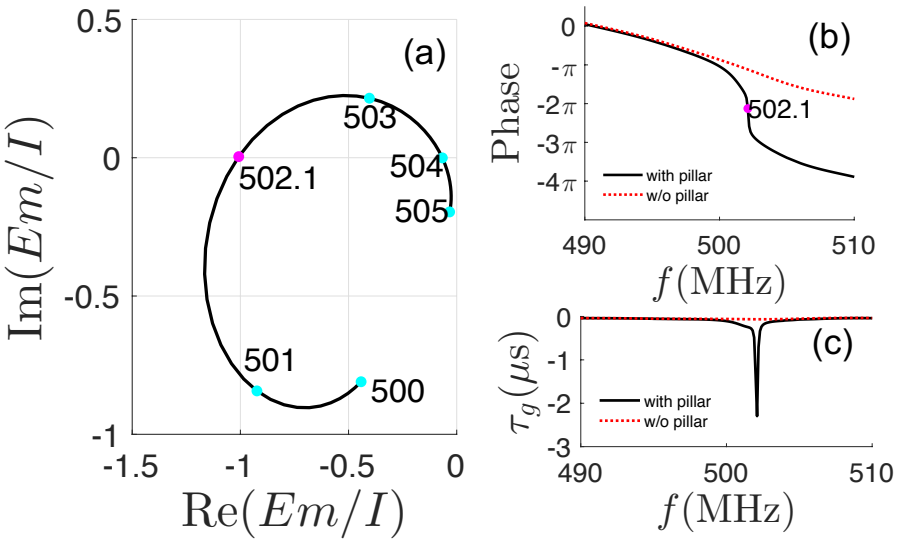

FIGURE 4.3 – (a) Complex plot of the normalized emitted waves in the frequency range [500, 505] MHz. The rose dot corresponds to the transmission dip at 502.1 MHz. (b) Phase of total transmitted waves. Red dotted line denotes the reference phase (incident waves without pillar). (c) Group delay time of the transmitted waves with and without pillar.

structure prediction. The displacement fields and the deformations at the two dips are shown in Fig 4.2(c). Due to their large SH component ratio, as well as the exclusive generation of SH waves by the electric field, we only show the transverse component u_y. The amplitude in pillar is normalized to the maximum amplitude in the matrix and is indicated beside the pillar. The two dips correspond to the pillar's intrinsic bending and torsional modes, respectively. The torsional mode induced transmission dip is better attenuated, since the excited torsional motion leads to, on the side opposite to the incident wave, a wave of identical amplitude and opposite phase, which is responsible for a destructive interference. To further confirm this mechanism, the emitted wave Em is calculated by subtracting the incident waves I (transmitted waves on the bare matrix without pillar) from the totally transmitted waves T : $Em = T - I$. Em is then normalized by I. Fig 4.3(a) is the complex plot of the normalized emitted wave in the frequency range [500, 505] MHz around the torsional mode. The rose dot corresponds to the dip

at resonant frequency of 502.1 MHz. This mode falls at point (-1,0), which refers to the same amplitude with a phase shift of 180°with respect to the incident waves. This results in a destructive interference and a strong attenuation in transmission. The phase shift of full transmitted waves is shown in Fig 4.3(b). Red dotted lines represent the incident waves. The dip corresponds to a π change in phase with respect to the incident waves. The phase shift is 0 (2π) before (after) the resonant frequency, meaning that the transmitted waves are in phase with the incident waves when they deviate from the resonant frequency. The corresponding phase derivative or group delay time τ_g of the transmitted waves is shown in Fig 4.3(c), with $\tau_g = \frac{d\phi}{d\omega}$, where ϕ denotes the phase and $\omega = 2\pi f$ is the angular frequency. The waves are delayed at the resonant frequency. It can be seen that the resonance is characterized by a rapid variation of phase and amplitude.

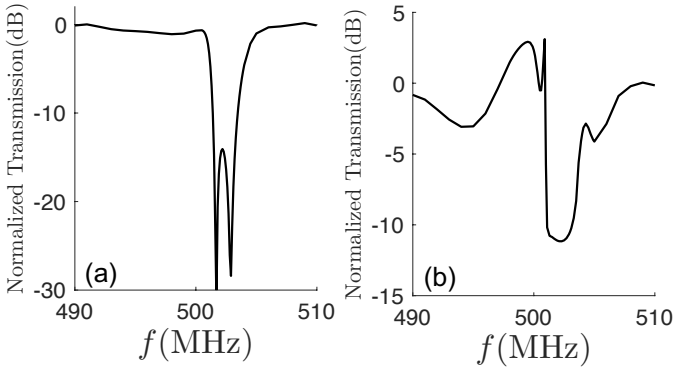

FIGURE 4.4 – Normalized transmission spectrum and of Love waves propagating through (a) 2 lines and (b) 10 lines of pillars.). $r_p = 0.2a_p$. $h = 0.6a_p$, $a_p = 2\mu$m.

This single pillar line is then changed to two lines, with a center distance equals to a_p. The transmission spectrum is shown in Fig 4.4(a). It can be seen that this structure enlarged the attenuation width while giving rise to two dips due to a coupling between the two pillars on the way of the waves propagation, which is a phenomenon that will be discussed in the section4.2. Fig 4.4(b) is the transmission spectrum obtained by 10 lines of pillars. The lower limit of the transmission has augmented whereas the dip

becomes wider until full stretched between the two limits of the hybridization band gap. Therefore, we can conclude that the lines number can affect the depth and the width of the resonant dip.

4.1.1 periodicity consideration

The effect of the lattice constance a_p on the resonant behaviors is then investigated. We modify gradually the value of a_p while keeping the pillar size, i.e. $r_p = 0.4\mu$m and $h = 1.2\mu$m. Fig 4.5 shows the dip frequency and width as functions of the lattice constance. It can be seen that the dip frequency decreases and then becomes almost constant with the increase of a_p, as a result of decreased coupling effect between the adjacent pillars. When a_p exceeds 2μm, the pillar coupling becomes very weak and the dip frequency is close to the pillar intrinsic torsional mode frequency. The dip width, here the full width at half maximum (FWHM) also decreases with the increase of a_p, which denotes an increase in the Q factor. To avoid a great pillar coupling effect in the y direction, we keep a_p at 2μm in the sections below.

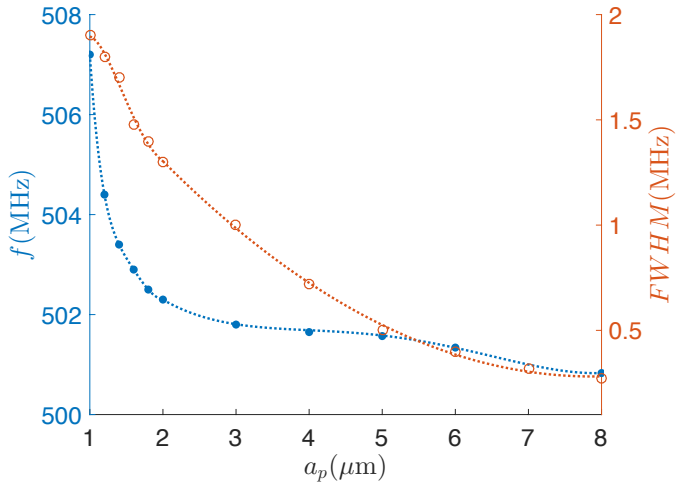

Figure 4.5 – Dip frequency (blue dots) and width (brown cycles) as functions of the lattice constance a_p. $r_p = 0.4\mu$m, $h = 1.2\mu$m.

4.2 Two lines of pillars

4.2.1 Two lines of identical pillars : Autler-Townes Splitting & cavity mode

Transmission spectra are then calculated around the torsional mode frequency for two lines of identical pillars. Corresponding supercell is shown in Fig.4.6. Two cylindrical Ni pillars on the silica film have a radius of $r_{p1} = r_{p2} = 0.2a_p$. The distance between the centers of the two pillars is denoted by d. In addition to our intuitively predicted transmission dip, different phenomena appear when we gradually increase the distance d between the pillar lines. When $d < 1.4a_p$ (Fig 4.7(a)), a coupling effect arises between the pillar lines, causing a lifting of frequency degeneracy of the pillar torsional mode, and the original transmission dip splits into two dips with a transparency window in the middle, referred to as acoustic analogue of Autler-Townes Splitting (ATS). The coupling becomes stronger when d gets smaller, as shown in Fig 4.7(a). Note that the pillar coupling also depends on the pillar mass. Therefore, the distance limit $1.4a_p$ can be detuned by changing the pillar size (radius or height). The displacement fields u_y at the dips and peak for $d = 0.5a_p$ are shown aside in Fig 4.7(d). It is found that the largest amplitude is located in the pillars for dip1 at 499.8 MHz. The two pillars are in opposite phase at dip1 frequency and in-phase at dip2 frequency, which is a feature of the ATS resonance that can be confirmed by calculating the phase difference between the two pillars. Since the pillars are in torsional mode in the range of measurement, all the points on the side of the pillar that faces the incident waves are in phase. The phases of u_y on the wave-facing sides of the two pillars are probed. The cases of $d = 0.5a_p$ and $d = a_p$ are shown as examples in Fig 4.8(a) and (b). Rose and green dots correspond to transmission dips and peaks, respectively. It can be seen that the two pillars have a phase difference of π at the first dip, meaning that they are 180°out-of-phase. The phase difference is 2π at the second dip, indicating that they are in-phase. This reveals that the pillar vibrations are symmetrical at the dip1 frequency and asymmetrical at the dip2

frequency.

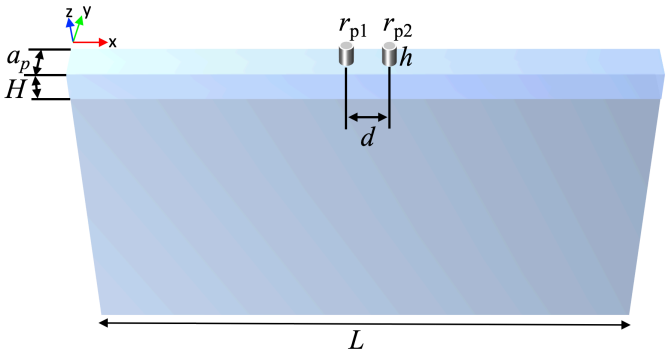

FIGURE 4.6 – Unit cell of two lines of cylindrical Ni pillars on the SiO_2 film deposited on a 90ST-cut quartz. The period is a_p along the y direction. Love waves propagate along the x-axis. r_{p1}=r_{p2}=0.2a_p, h = 0.6a_p, H=2.4μm, L=20a_p, a_p = 2μm.

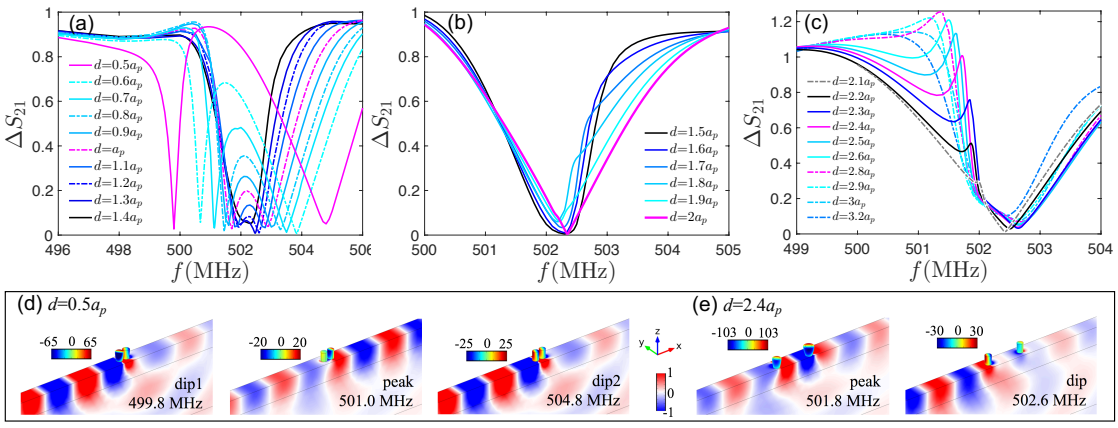

FIGURE 4.7 – Normalized transmission spectrum of Love waves propagating through the two identical pillar lines around the resonant frequency of torsional mode at 502.1 MHz with different central distance d : (a) presents the lifting of degeneracy and the apparition of Autler-Townes Splitting with the decrease of d ; (b) shows the red-shift of cavity mode by increasing d when $d < 2a_p$ (c) presents the appearance of cavity mode peak when $d > 2a_p$. (d) and (e) are the displacement fields u_y at the dips and peaks for d=0.5a_p and 2.4a_p, respectively. r_{p1}=r_{p2}=0.2a_p, a_p = 2μm.

Since we work around 500MHz with Love waves velocity v around 4200 m/s, the wavelength $\lambda = v/f$ is therefore around 8.4μm. $d \approx 2a_p$ ($a_p = 2\mu m$) indicates a distance around $\lambda/2$ corresponding to the Fabry-Perot (FP) resonance. This resonance is almost invisible in the transmission spectrum when it matches the pillar torsion mode, since

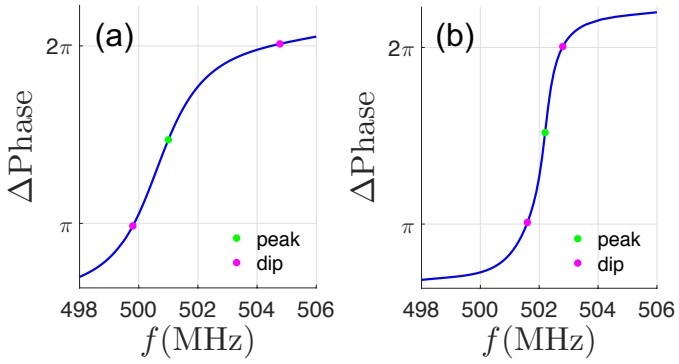

FIGURE 4.8 – Pillar phase differences for ATS in the case of (a) $d = 0.5a_p$ and (b) $d = a_p$. Rose and green dots correspond to transmission dips and peaks, respectively. r_1=r_2=$0.2a_p$, $a_p = 2\mu$m.

the waves are almost totally reflected. However, when we change the distance between pillars around $\lambda/2$, the proximity of FP resonance with the pillar mode gives rise to the cavity modes at the two edges of the dip, as shown in Fig 4.7(b) and (c). In these cases, the two pillars act like partial reflectors, and the normally incident waves are multiply reflected to produce multiple transmitted waves with path difference equal to $n\lambda$, where n is an integer. In this way, constructive interference occurs, leading to a resonant enhancement. The two pillars along with the guiding layer between them become a cavity to confine the waves. Nevertheless, in the transmission spectra, the behaviors for $d < 2a_p$ (Fig 4.7(b)) are less marked than that for $d > 2a_p$ (Fig 4.7(c)), where peaks rise at the lower edge of the dip, and give rise to Fano-like resonance line-shapes. However, we have verified that it can not be fitted by a Fano type formula. The displacement field u_y at the peak and dip for $d = 2.4a_p$ are shown aside in Fig 4.7(e), since the transmission curve for $d = 2.4a_p$ presents the most confined peak. At the peak frequency, large amplitudes are observed for the three parts of the cavity (two pillars and the guiding layer in between). This behavior is different from that of ATS, the largest amplitude in the pillars occurs at the peak where the waves in the guiding layer are highly confined in the cavity.

To show more clearly the transition of the cavity mode with respect to the dip when

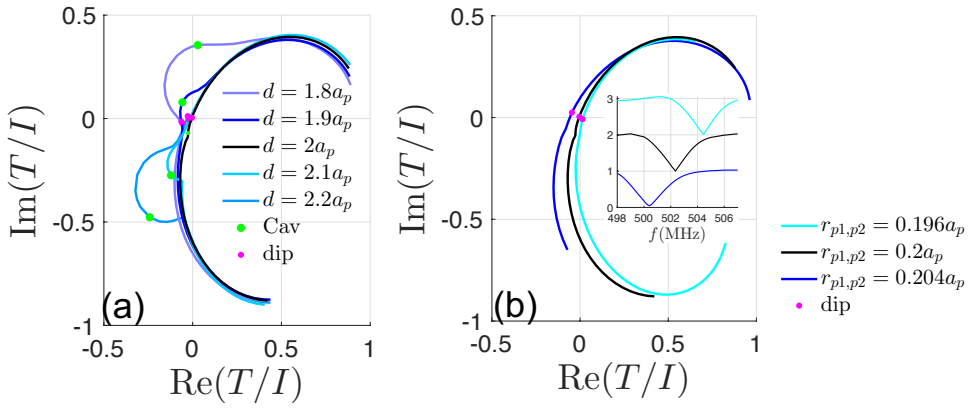

FIGURE 4.9 – (a)Complex plots of the normalized transmissiosn in the frequency range [500, 505] MHz for d varies from $1.8a_p$ to $2.2a_p$. The rose and green marks correspond to the dip and cavity mode frequencies, respectively. r_{p1}=r_{p2}=$0.2a_p$. (b) Complex plots of the normalized transmissions for $d = 2a_p \approx \lambda/2$ when all the pillars' radius vary from $0.196a_p$ to $0.204a_p$. Inset shows the transmission spectra of corresponding curves.

d changes, we draw the complex plots of the normalized transmissions in Fig 4.9(a). The cavity mode is manifested as an additional perturbation on the original ellipse. Since the phase changes clockwise, it can be seen that the cavity mode passes the dip as d increases. When the cavity mode approaches to the dip, the perturbation decreases. For $d = 2a_p$, the cavity mode coincides with the FP resonance and becomes almost invisible. Additionally, we can see that the behaviors for $d < 2a_p$ and for $d > 2a_p$ are quite similar, with the perturbation frequency either larger or smaller than the dip frequency.

Fig 4.9(b) shows the complex plots of the normalized transmissions of Love waves for $d = 2a_p$ when we change the radius of both pillars from $0.196a_p$ to $0.204a_p$, indicating a shift in pillar resonant frequency. It is found that the cavity mode remains almost invisible, i.e. still coincides with the FP resonance. That is because the distance between pillars corresponding to the FP resonance is almost unchanged in our range of measurement (from 498 to 506 MHz), i.e. $\lambda/2$ is always around $d = 2a_p$. Therefore when we change the pillar vibration frequency, we obtain the parallel cavity modes for the same value of d.

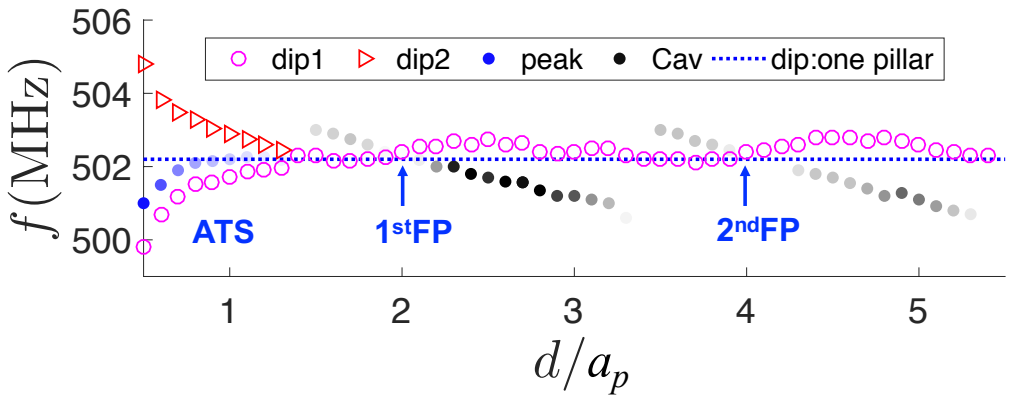

FIGURE 4.10 – Dip, peak and cavity mode frequencies as functions of the distance d between two identical pillar lines. Blue dotted line is the dip frequency of a single pillar line. ATS appears in the coupling region of $d < 1.4a_p$. The 1^{st} and 2^{nd} Fabry-Perot resonances fall at d=$\lambda/2$ and λ, respectively. r_{p1}=r_{p2}=$0.2a_p$, $a_p = 2\mu$m.

To give an overview of the resonance behaviors, the dip and peak frequencies for different d are shown in Fig 4.10. Blue dotted line is the dip frequency of the single pillar line. It can be seen that the pillar coupling induced ATS is in the region $d < 1.4a_p$, where the two dips are mismatched with the single pillar resonant frequency. This coupling disappears when d exceeds $1.4a_p$, and only one dip (quasi-zero transmission) remains. This dip matches the single pillar resonant frequency except when the cavity modes appear below (upon), the dip frequency shifts slightly upward (downward). The interaction between the pillars is much stronger for d/a_p=2 than that for d/a_p=4. Therefore, the resonances around d=λ are too weak to be observed. Note that the frequency of the cavity modes changes much slower than that of the FP resonance. The 1^{st} and 2^{nd} FP resonance exists only in the very closed regions around $d = 2a_p$ and $4a_p$, respectively. In these two cases, FP resonances are particular cases of the cavity modes when the later coincide with the dip. In the other regions, one should avoid to mix up the cavity mode with the FP resonance.

In order to show the behavior of the cavity modes at the vicinity of the transmission dip, we plotted in Fig 4.11(a) the transmission spectra for $d = 2.4a_p$ when all the pillars'

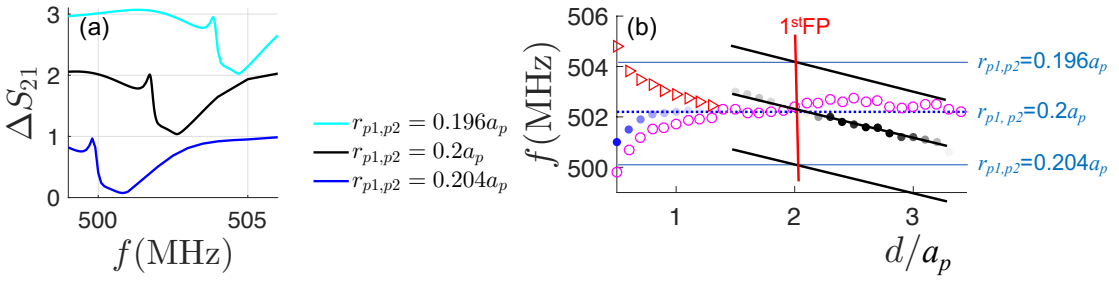

FIGURE 4.11 – (a)Transmission spectra for $d = 2.4a_p$ when all the pillars' radius vary from $0.196a_p$ to $0.204a_p$. (b) Cavity modes (black lines) for two lines of identical pillars when changing the pillar resonant frequency (blue lines). Red line denotes the 1^{st} FP resonance.

radius vary from $0.196a_p$ to $0.204a_p$. It can be seen that we obtain almost the same cavity mode at different frequencies. Along with Fig 4.9(b), we can present in Fig 4.11(b) the relation between cavity modes (black lines) and FP resonance (red line). When we change the pillar resonant frequency (blue lines), FP resonance remains at almost the same position. For each radius value, the FP resonance is a particular case of the cavity modes when the later coincide with the dip.

4.2.2 Two lines of dissimilar pillars : Autler-Townes Splitting, cavity & Acoustically Induced Transparency

Since an increase of pillar radius or height will induce a decrease in the torsional mode frequency, one can gradually tune the position of the dip by modifying the pillar size. Here we modify the pillar radius as example since the radius is easier to be tuned in experimental process.

The effect of pillar radius on the hybridization band gap is presented in Fig 4.12(a). An increase of radius will induce a decrease in resonant frequency and an increase in band gap width.

In the case below, the second pillar radius r_{p2} is tuned from $0.195a_p$ to $0.205a_p$, while the first pillar radius r_{p1} being fixed to $0.2a_p$. Fig 4.13 shows the transmission spectra

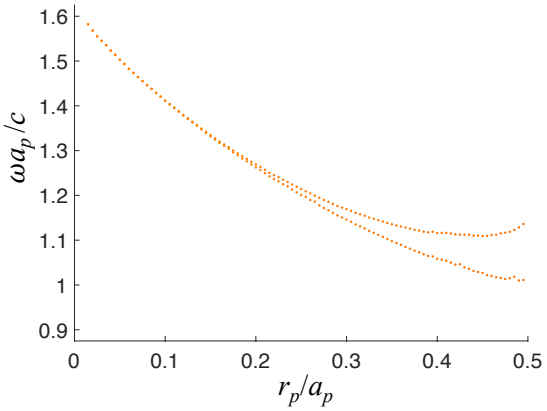

FIGURE 4.12 – Hybridization band gap as a function of the pillar radius. The band gap is between the two dotted lines. $a_p = 2\mu$m.

of Love waves propagating through the two dissimilar pillar lines for different d that remains unchanged for each case. Dotted blue and rose lines denote the dip positions for a single line of pillars with radius equals to r_{p1} and r_{p2}, respectively. Fig 4.13(a) corresponds to the case $d = 0.5a$, where the coupling between the pillars is so strong that the two dips stay all the way mismatched with their corresponding single pillar dip positions. When d gets larger, the coupling becomes weaker : Fig 4.13(b) corresponds to the case $d = a_p$. It is found that this coupling decreases with the increase of radius mismatch. In the case of $r_{p2} = 0.195a_p$ and $0.205a_p$, each dip almost coincides with the corresponding resonant frequency of one single pillar. In order to show the anti-crossing lines of ATS for $d < 1.4a_p$, we plotted in Fig 4.14 the dip frequencies for different d as functions of r_{p2}. It can be seen that with the increase of pillar distance, the anti-crossing lines get closer to the crossing line (for $d = 1.4a_p$), and that each anti-crossing line will rejoin its individual pillar resonant frequency when the radius mismatch is sufficiently large. This means the pillar coupling effect decreases when their distance or/and their radius difference increases.

For $d = 2a_p$ as shown in Fig 4.13(c), two pillars with different radius give rise to two dips with a transparency window in the middle. These peaks have a narrower

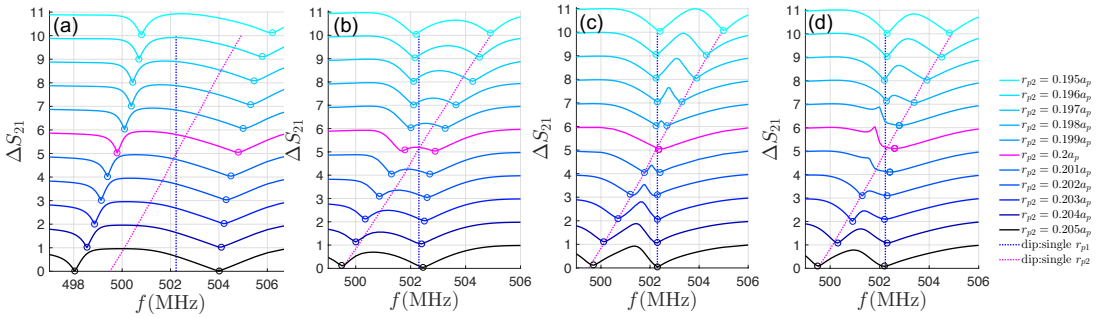

FIGURE 4.13 – (a) Transmission spectra of Love waves for d= (a)$0.5a_p$, (b)a_p, (c)$2a_p$, (d)$2.4a_p$ when gradually changing the radius of the second pillar from $0.195a_p$ to $0.205a_p$. The radius of the first pillar r_{p1} is fixed to $0.2a_p$. $a_p = 2\mu$m.

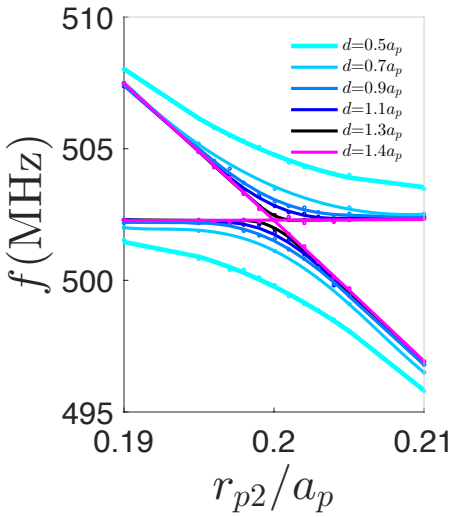

FIGURE 4.14 – Anti-crossing lines for ATS when $d < 1.4a_p$. Dip frequencies for different d as a function of the second pillar radius r_{p2}. r_{p1} is fixed to $0.2a_p$. $a_p = 2\mu$m.

line-shapes compared with the cases of ATS (see also Fig 4.16). Each dip is consistent with the corresponding dip frequency of one single pillar since no more coupling exists, which means each of them originates from individual pillar's torsional mode. The displacement fields u_y for $r_2 = 0.202a_p$ are presented in Fig 4.15. It can be seen that each dip corresponds to a large amplitude in a single pillar, indicating the attenuation of transmission at each pillar's resonant frequency due to the destructive interferences. The peak correspond to a Fabry-Perot resonance since d is close to $\lambda/2$. The two detuned

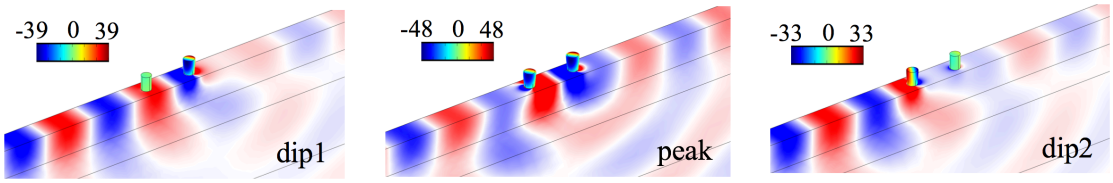

FIGURE 4.15 – Displacement field u_y at the dips and peak for AIT in the case of $d = 2a_p$. The two pillars differ in radius with $r_{p2} = 0.202a_p$ and $r_{p1} = 0.2a_p$. $a_p = 2\mu$m.

pillar modes act as two partial reflectors and are hence able to support the constructive interference of the FP resonance, where large amplitudes are observed for the three parts of the cavity (two pillars and the guiding layer in between). This three-resonance system induced transparency window is referred to as the Acoustic analogue of Electromagnetically Induced Transparency, also called Acoustically Induced Transparency (AIT). The peak rises and gets wider with the increase of radius difference. As for $d = 2.4a_p$ shown in Fig 4.13(d), where a cavity mode peak is observed for the two identical pillars, it is found that with the increase of pillar radius mismatch, the peak confinement decreases and the dip1 becomes evident for $r_{p2} = 0.198a_p$ and $0.202a_p$. Compared with the case of $d = 2a_p$ (Fig 4.13(d)), the peak between two dips is less confined due to the red shift of cavity mode with respect to the pillar resonant frequency. Note that AIT requires a well excited resonance between the two dips. Therefore, in the case of $d = 2.4a_p$, the transparency window is only two dips resulting from the different resonant frequencies of two pillars.

The transmission spectra of AIT are similar with those of ATS, however, they originate from different mechanisms. ATS appears only when the two pillars are coupled to each other, and exists even when the two pillars are identical. AIT appears when d is out of the pillar coupling region and only when the two pillars are different. The pillars and the cavity interact at the peak. Moreover, AIT requires a clearly identified 3-level resonant system, which is not the case for ATS.

Besides the different mechanisms related to ATS and AIT as presented above, cor-

responding analytical formulas of ATS and AIT for transmission spectra can be used to fit the numerical data to better distinguish these different transparency windows. The transmission curves for ATS can be written as the sum of two separate inverse Lorentzian profiles representing the two dips, while the transmission for AIT is expressed as the difference of a broad Lorentzian profiles and a narrow one with a similar central frequency [205, 216] :

$$T_{ATS} = 1 - \frac{C_1(\Gamma_1/2)^2}{(f-\delta_1)^2 + (\Gamma_1/2)^2} - \frac{C_2(\Gamma_2/2)^2}{(f-\delta_2)^2 + (\Gamma_2/2)^2}, \tag{4.1}$$

$$T_{AIT} = 1 - \frac{C_+(\Gamma_+/2)^2}{(f-\delta_c-\epsilon)^2 + (\Gamma_+/2)^2} + \frac{C_-(\Gamma_-/2)^2}{(f-\delta_c)^2 + (\Gamma_-/2)^2}, \tag{4.2}$$

where C_1, C_2, C_+, C_- are the amplitudes of the Lorentzian profiles, Γ_1, Γ_2, Γ_+, Γ_- are their full width at half maximum (FWHM). δ_1, δ_2, δ_c are the central frequencies with ϵ denoting a possible slight shift on δ_c. Γ_1, Γ_2, δ_1, δ_2 and δ_c can be directly taken from the transmission spectra.

In an intermediate state, the transmission spectra can be fitted by a transition formula that considers both the features of ATS and AIT :

$$\begin{aligned} T_{ATS/AIT} = 1 &- \frac{C_a(\Gamma_a/2)^2}{(f-\delta_1)^2 + (\Gamma_a/2)^2} - \frac{C_b(\Gamma_b/2)^2}{(f-\delta_2)^2 + (\Gamma_b/2)^2} \\ &- \frac{(f-\delta_1)C_d(\Gamma_d/2)^2}{(f-\delta_1)^2 + (\Gamma_d/2)^2} + \frac{(f-\delta_2)C_e(\Gamma_e/2)^2}{(f-\delta_2)^2 + (\Gamma_e/2)^2}, \end{aligned} \tag{4.3}$$

where C_a, C_b, C_d, C_e, Γ_a, Γ_b, Γ_d, Γ_e are parameters to be determined. Note that this formula can also be used to fit the ATS and AIT cases.

Fig 4.16 shows the numerical data (black dots) together with the best fit functions T_{ATS} (red lines) and T_{AIT} (blue lines) for the four values of d in Fig 4.13 which stand for strong coupling ATS, weak coupling ATS, AIT and intermediate states, respectively, in the case of $r_{p2} = 0.202a_p$ and r_{p1} fixed to $0.2a_p$. The best fit functions are determined

by resorting to the least-squares method, that is, by searching the fit parameters that minimize the sum of squared errors between numerical data and fit function :

$$\sum (FEM_i - F_i)^2, i \in [1, N] \tag{4.4}$$

where N is the number of values calculated by FEM. F_i is the value of T_{ATS} or T_{AIT} corresponding to each data frequency. It can be seen that, as expected, for $d = 0.5a_p$ and a_p where coupling exists between the pillars, T_{ATS} fits the numerical data much better than T_{AIT}. Whereas for $d = 2a_p$, T_{AIT} fits the numerical data better than T_{ATS}. For $d = 2.4a_p$, both T_{ATS} and T_{AIT} do not fit the numerical data well. In this case, $T_{ATS/AIT}$ (green line) fits the data better.

By fitting the numerical data to the model fits of T_{ATS} and T_{AIT} for different r_{p2} (r_{p1} fixed), the relation between the fits parameters and r_{p2} can be obtained as shown in Fig 4.17, where Fig 4.17(a) presents the fit parameters of the ATS model for $d = 0.5a_p$ and Fig 4.17(b) are those of the AIT model for $d = 2a_p$. The parameters of ATS model describing each Lorentzian curve are independent of each other. It can be seen that Γ_1 increases with the increase of radius mismatch while Γ_2 increases with the increase of r_{p2}. We think this is resulting from the symmetrical/asymmetrical vibration of the two pillars at dip1/dip2 in the ATS cases. C_1 is relatively stable while C_2 presents a slight tendency to increase. The parameters of AIT model are related to each other. As can be seen in Fig 4.17(b), these four parameters all increase as the radius mismatch increases and are almost symmetrical in our range of measurement. Despite a larger values of Γ_+ compared with Γ_-, C_+ and C_- are almost the same for different r_{p2} .

With the increase of distance between pillars, the transition from ATS to AIT can be quantitatively studied by evaluating the quality of these model fits. The Akaike information criterion (AIC)[225] is used to discern AIT from ATS, which provides a method to select the best model from a set of models. This criterion quantifies the

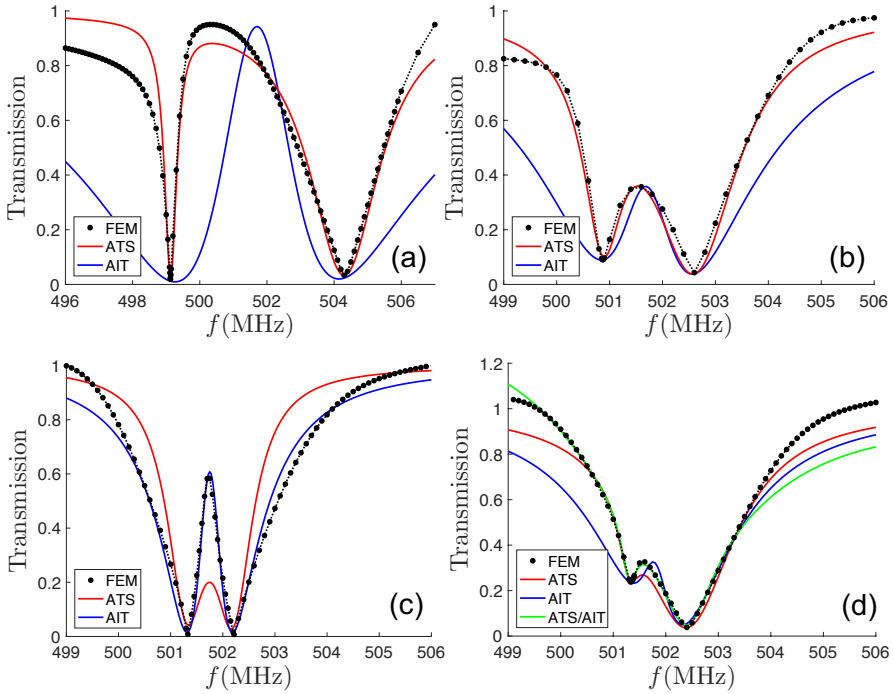

FIGURE 4.16 – Transmission spectra and model fits of ATS and AIT, for $r_1 = 0.2a_p$, $r_2 = 0.202a_p$ and $a_p = 2\mu$m. Numerical data (black dots) are presented together with the best fits of functions T_{ATS} (red lines) and T_{AIT} (blue lines). For (a) d=0.5a_p and (b)$d = a_p$, T_{ATS} fits the numerical data better than T_{AIT}. (c) For d=2a_p, T_{AIT} fits the numerical data better than T_{ATS}. (d) For d=2.4a_p, $T_{ATS/AIT}$ (green line) can be used to fit the numerical data whereas T_{ATS} and T_{AIT} do not fit well.

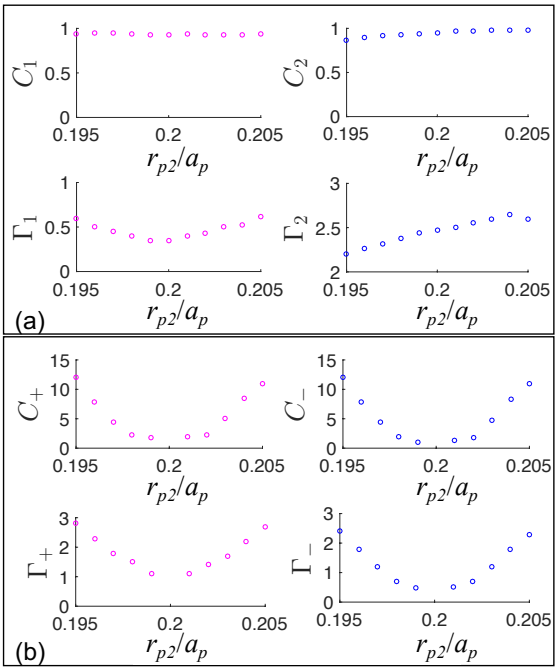

FIGURE 4.17 – Fit parameters as functions of r_{p2}/a_p for (a)$d = 0.5a_p$ with model fits T_{ATS} ; (b)$d = 2a_p$ with model fits T_{AIT}. $r_{p1} = 0.2a_p$, $a_p = 2\mu$m

amount of information lost, i.e. the degree of unfitness, and is given as $I_j = 2k - 2ln(L_j)$, where $k = 4$ is the number of unknown parameters and L_j the maximum likelihood for the considered models, i.e. j =ATS or AIT. Since we already found the best fit functions of T_{ATS} and T_{AIT}, it is sufficient to calculate the likelihood of these two functions. Then, the AIC weight $W_j = e^{-I_j/2}/\sum_1^N e^{-I_j/2}$ can give the relative likelihood of a candidate model. N is the number of considered model. In our case, $N = 2$ as only two models are involved. Since we have more than one calculated data for each model, we utilize the AIC mean per-point weight[214] $\overline{w}_j = e^{-I_j/2n}/\sum_1^N e^{-I_j/2n}$ to calculate the statistically synthesized likelihood of the candidate model. n is the calculated data number. The AIC mean weight can be rewritten as :

$$\overline{w}_{ATS} = \frac{e^{-I_{ATS}/2n}}{e^{-I_{ATS}/2n} + e^{-I_{AIT}/2n}} \tag{4.5}$$

with $\overline{w}_{ATS} + \overline{w}_{AIT} = 1$.

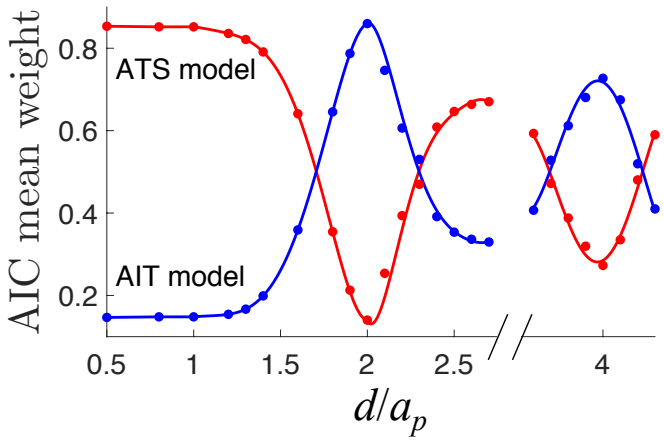

FIGURE 4.18 – AIC mean weight as a function of the distance between pillars d for ATS model (red line) and AIT model (blue line), in the case of $r_{p2} = 0.202a_p$. $r_{p1} = 0.2a_p$, $a_p = 2\mu$m

Fig 4.18 shows the AIC mean weight of the ATS and AIT models as function of the distance between pillars, in the case of $r_{p2} = 0.202a_p$ and $r_{p1} = 0.2a_p$. It can be seen that, as expected, the AIC mean weight of ATS model is dominant for the small distance region, which means it is preferable to use the ATS model. When the d increases, the AIC mean weight of AIT model starts to increase as well, and becomes dominant for $d \in [1.8a_p, 2.2a_p]$. Since cavity mode is not presented at the peak for $d = 1.8a_p$, and starts to interact with the dip1 for $d = 2.2a_p$, the AIT is hence in the distance range of $d \in [1.9a_p, 2.1a_p]$. When d continues to increase, the AIC mean weight of ATS becomes dominant again until d increases to around $4a_p$, i.e. the position of the second FP resonance, where we found the second AIT position for $d \in [3.9a_p, 4.1a_p]$. The periodicity of AIT, which is a behavior that hasn't been addressed before in the existing literature, results from the periodic apparition of FP resonance. The AIC mean weight of the second AIT region is smaller than that of the first AIT region, since the interaction of the system decreases with the increase of distance between pillars d. Note that the ATS in our case exists

only for $d < 1.4a_p$, therefore the transition region $d \in [1.4a_p, 1.8a_p]$ as well as the larger distances other than the AIT regions do not represent ATS or AIT. We can see that the theoretical distinction between ATS and AIT helps the comprehension of the analytical results. On the other hand, this criterion is useful when we cannot theoretically rule out the AIT phenomenon. This happens for example when the radius mismatch is so large that the peak is much wider with respect to the two dips. In this case, although FP resonance is still present between two dips, the transmission spectra can not be well fitted by the AIT model and therefore cannot be ascribed to an AIT.

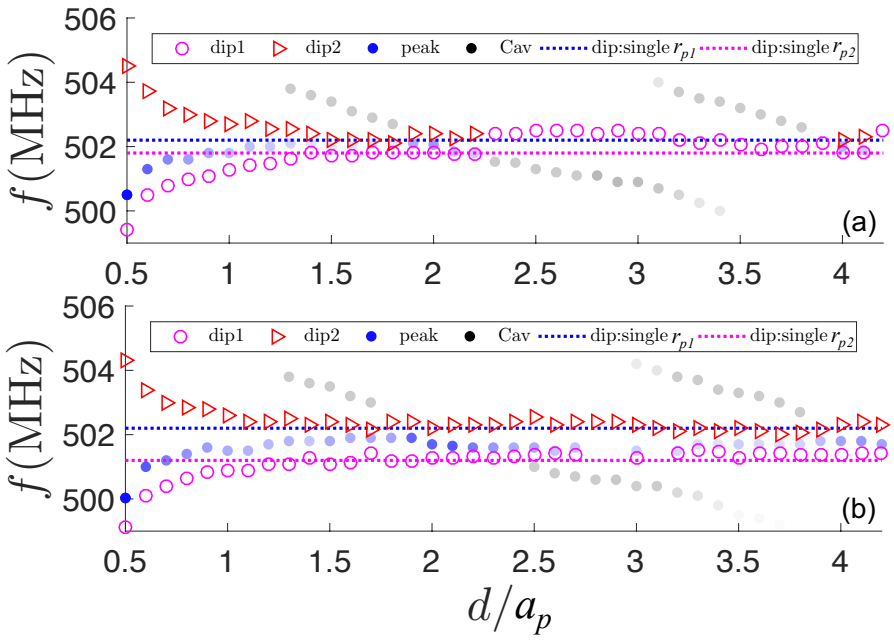

FIGURE 4.19 – Frequencies of dips, peaks and cavity modes as a function of the distance d between two dissimilar pillar lines, in the case of (a) $r_{p1} = 0.2a_p$ and $r_{p2} = 0.201a_p$, and (b) $r_{p1} = 0.2a_p$ and $r_{p2} = 0.202a_p$. $a_p = 2\mu$m.

Fig 4.19 gives the same results as in Fig 4.10, but with two lines of dissimilar pillars. Fig 4.19(a) is the case of $r_{p1} = 0.2a_p$ and $r_{p2} = 0.201a_p$. Dip1 corresponds to the second pillar. It can be seen that outside the ATS region, this dip becomes invisible after d exceeding $2.2a_p$. This is because on the one hand, the interaction between the two pillars becomes too weak and on the other hand, the radius mismatch is too small : This dip

become visible again when d approaches to $4a_p$, since the interaction between the two pillars regains its strength in the AIT region. When we enlarge the radius difference (see Fig 4.19(b)), most of the dip1 in this region become visible. Moreover, we can see that the cavity modes cross the center of the two dips at d=$2a_p$ and $4a_p$, where we obtain the AIT type of FP resonance. This behavior is compatible with the cavity mode-FP resonance relation that we presented in Fig 4.11(b). FP resonances are particular cases of the cavity modes when the later fall in the center of the two dips.

pillar height mismatch

The radius of the two pillars are increased/reduced from the original radius $r_p = 0.2a_p$ by the same amount Δr. That is, $r_{p1} = r_p + \Delta r$ and $r_{p2} = r_p - \Delta r$, with the height h fixed at $0.6a_p$. Fig 4.20(a) shows the transmission spectra of Love waves through the two lines of pillars when $d = 2a_p$, i.e. in the region of AIT. It can be seen that by decreasing Δr, the two dips approach to each other and the peak with almost unchanged frequency decreases and becomes invisible for identical pillars.

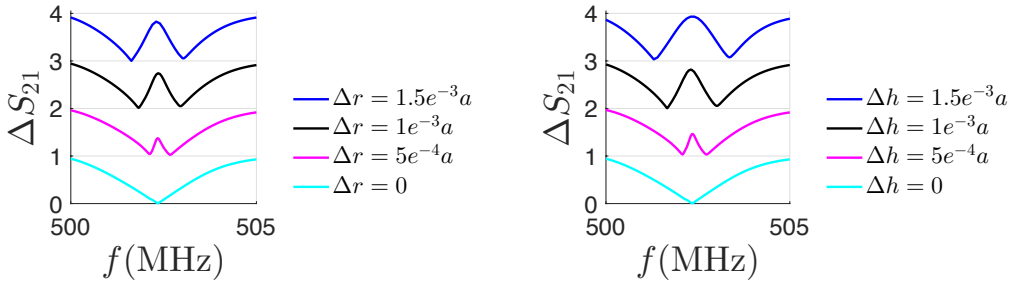

FIGURE 4.20 – (a)Normalized transmission spectra of Love waves propagating through the two lines of pillars with different radii, r_{p1}=r_p+Δr and r_{p2}=r_p-Δr, in the case of $d = 2a_p$. AIT peak rises and becomes wider with the increase of pillar height mismatch. $h = 0.6a_p$, $r_p = 0.2a_p$. (b)Same as (a) but detuning the pillar heights : h_1=h+Δh and h_2=h-Δh, in the case of $d = 2a_p$. $h = 0.6a_p$, $r_{p1,p2} = 0.2a_p$ and $a_p = 2\mu$m

Since the pillar intrinsic mode is sensitive to the pillar size, the above effects can also be obtained by detuning the pillar height. In the same way, the heights of the two pillars are increased/reduced from the original height $h = 0.6a_p$ by the same amount

Δh, i.e. $h_1 = h + \Delta h$ and $h_2 = h - \Delta h$. The radius of both the two pillars r_{p1} and r_{p2} are fixed at $0.2a_p$. The distance between the two pillars is also $d = 2a_p$. Fig 4.20(b) shows the corresponding transmission spectra. It can be seen that the modification of pillar height has similar effects on the line-shapes of the transmission spectra.

4.3 Fano resonance by geometrical mismatch

In this section we will investigate one line of alternating pillars that differ in geometrical parameters, namely the radius and the height. Fig 4.21 shows the supercell of this structure, which contains only two pillars with periodic conditions applied along the y axis.

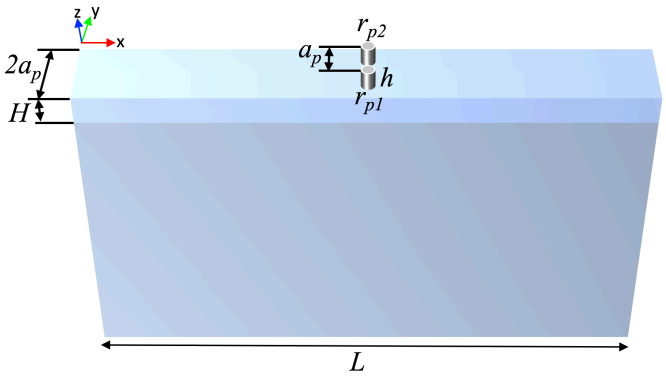

FIGURE 4.21 – Supercell of one line of alternating Ni pillars on the SiO_2 film deposited on a 90ST-cut quartz. The period is $2a_p$ along the y direction. Love waves propagate along the x-axis. r_{p1}=$0.2a_p$, $h = 0.6a_p$, H=2.4μm, L=$20a_p$, $a_p = 2\mu$m.

As indicated in Fig 4.22, two pillars in different radius give rise to two dips. Each dip is consistent with the corresponding resonant frequency of one single pillar, meaning that each of them originate from individual pillar's torsional mode. The displacement fields are presented aside. It can be seen that each dip corresponds to a large amplitude in a single pillar, indicating the attenuation of transmission at each pillar's resonant frequency. Between these two dips is a passing band. The maximum transmission in this passing band is denoted as a peak p. Note that single pillar dips are calculated by

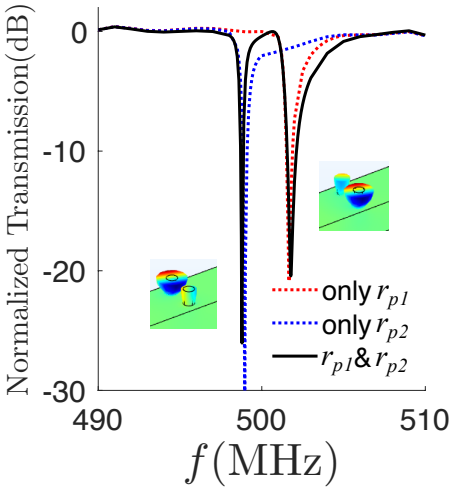

FIGURE 4.22 – Normalized transmission spectra of Love waves through the pillar line. u_y for two dips are shown aside. $r_{p1} = 0.2a_p, r_{p2} = 0.205a_p$. $H = 2.4\mu$m, $a_p = 2\mu$m.

removing the other one, i.e. a pillar with a periodicity of $2a_p$, since this line of alternating pillars is actually a combination of two pillared PnCs of which each has a periodicity of $2a_p$. These two dips are well suited to each single pillar dip since the difference in radius is not small enough, so the coupling between the two pillar is quite weak.

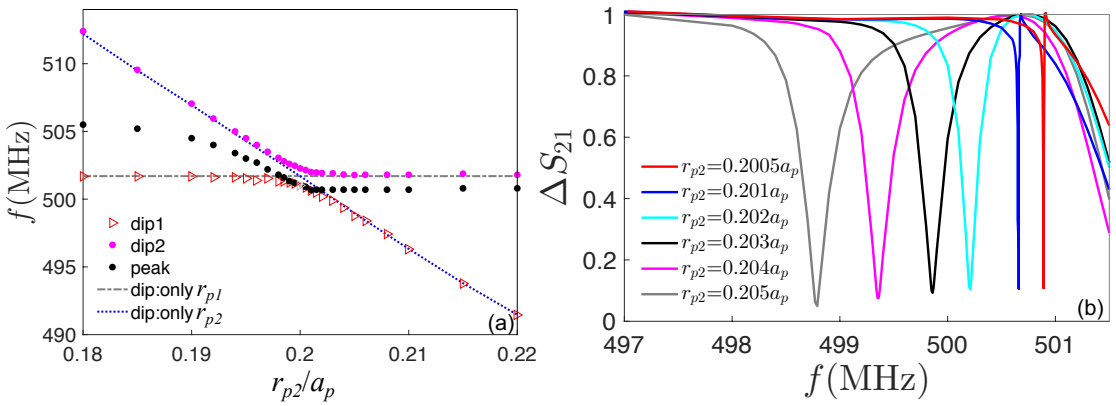

FIGURE 4.23 – (a) Dips and peak frequency as a function of the radius of pillar2. Gray dashed line and blue dotted line are respectively the dip frequency of a single pillar of r_{p1} and r_{p2} with doubled periodicity $2a_p$; (b) Normalized transmission spectra for r_{p2} varies from $0.2005a_p$ to $0.205a_p$. $r_{p1} = 0.2a_p$, $a_p = 2\mu$m.

If we gradually reduce the difference between the two pillar radii, these two dips will

become closer until the coupling between the pillars is strong enough and the two dips become mismatched with their corresponding single pillar dips, as shown in Fig 4.23(a). In this whole view of the pillars coupling behaviors, it can be seen that the mismatching region, i.e. the coupling region, for r_{p2} is between $0.199a_p$ and $0.201a_p$. One interesting point is that when r_{p2} approaches to r_{p1}, the peak intensity does not decrease and the peak starts to be very close to the first dip, forming along with the dip1 the asymmetric transmission line-shapes, referred to as Fano resonances. It is worth noting that, when $r_{p1} = r_{p2}$, the only dip is induced by a line of same pillars with a period of a_p, where a weak coupling between the pillars results in a mismatch from the pillar intrinsic torsional mode frequency (the intersection point of the blue and gray lines). Fig 4.23(b) describes the transmission spectra for r_{p2} varies from $0.2005a_p$ to $0.205a_p$. As we can see, dip1 become increasingly finer, as it moves to the peak. When $r_{p2} \leq 0.201a_p$, where the coupling become relatively strong, the peak starts to appear sharp.

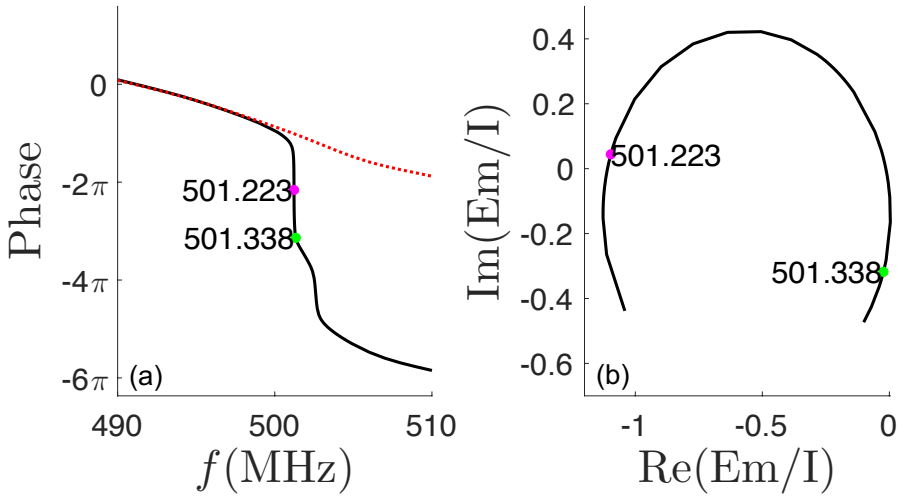

FIGURE 4.24 – (a) Phase shift of the full transmitted Love waves, red dotted line is the phase of the incident waves; (b) Complex plot of Love waves emitted by the pillar line in the frequency range (501.21, 501.35) MHz. The two frequencies marked in rose corresponds to the dip1 and peak when $r_{p2} = 0.199a_p$. $r_{p1} = 0.2a_p$, $a_p = 2\mu$m.

Fig 4.24(a) shows the phase shift of the full transmitted waves for $r_{p2} = 0.199a_p$ and

$r_{p1} = 0, 2a_p$. Red dotted line is the phase of the incident waves (transmitted waves without pillars). The two frequencies marked in rose corresponds to the dip1 (at $f = 501.223$ MHz) and peak (at $f = 501.338$ MHz). It can be seen that dip1 corresponds to a phase shift of π and the peak corresponds to a phase shift of 2π. The normalized emitted waves for $r_{p2} = 0.199a_p$ and $r_{p1} = 0, 2a_p$ are calculated and a Complex plot of normalized emitted wave are shown in Fig 4.24(b). At $f = 501.223$ MHz, the normalized emitted wave is near the point (-1,0), indicating an amplitude close to 1 and a 180°out-of-phase with respect to the incident waves, which results in a destructive interference and a strong attenuation in transmission. At $f = 501.338$ MHz, the emitted wave is close to (0,-0.3) point, indicating a small amplitude with 90°phase shift, which will induce a slight amplitude enrichment.

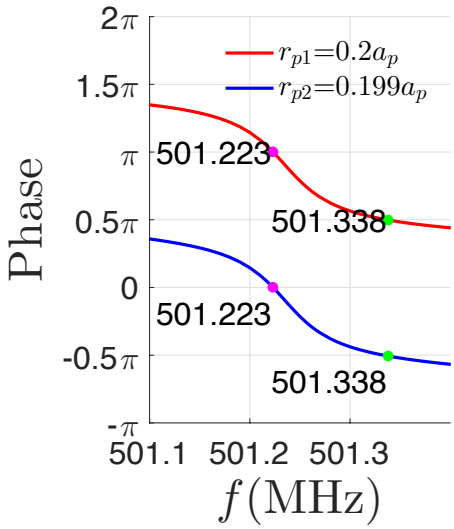

Figure 4.25 – (a) Phase shift on the wave-facing side of the pillars in the frequency range (501.1, 501.4) MHz. $r_{p1} = 0.2a_p$, $r_{p2} = 0.199a_p$, $a_p = 2\mu$m.

Fig 4.25 shows the displacement phase on the wave-facing sides of the two pillars, in the frequency range of (501.1, 501.4) MHz. It can be seen that the two pillars have a phase difference of π, and each pillar has a phase shift of $\frac{\pi}{2}$ from dip1 (at 501.223 MHz) to peak (at 501.338 MHz).

The above results allow us to conclude that a Fano resonance can be induced by a slight radius difference for the two dissimilar pillars. The origin of this Fano resonance is a strong coupling between the two pillars, which arouses a degeneracy of both modes from their individual resonant frequecy. The Fano resonance is an asymmetric transmission line-shape resulting from the interference between the emitted and incident waves. The anti-resonance (dip1) corresponds to an amplitude close to 1 and a phase shift of π for the normaliezed emitted waves, whereas the resonance peak corresponds to an small amplitude with a phase shift of $\pi/2$, which enriches the incident waves amplitude. This resonance peak persists as long as the radius differece is not canceled, and can be confined by reducing the radius mismatch.

4.3.1 Periodicity influence

Since a small lattice constance in the y direction can induce a strong coupling effect between the pillars as shown in Fig 4.5, we decrease a_p in the cases below while maintaining the pillar size. Fig 4.26(a) shows the transmission spectra of Love waves propagating through the alternating pillar line for different a_p, in the case of $r_{p1} = 0.4\mu$m and $r_{p2} = 0.398\mu$m. It can be seen that with the decrease of a_p, dip1 becomes shaper and the peak changes to the other side of the dip1. Corresponding quality factors (Q) of the dip1 are shown in the table above the figure. Moreover, dip1 frequency decreases to show a greater mismatch with the corresponding single pillar dip frequency. Fig 4.26(b) shows the dips and peak frequencies as functions of the lattice constance a_p. The frequency difference between the two dips becomes larger when decreasing a_p, resulting from the increased pillar coupling effect.

$a_p(\mu$m)	1	1.2	1.4	1.6	1.8	2
Q	3.33e^5	4.76e^4	5.56e^4	1.67e^4	1.43e^4	1.25e^4

When gradually varying the second pillar radius r_{p2} from 0.39μm to 0.41μm, the

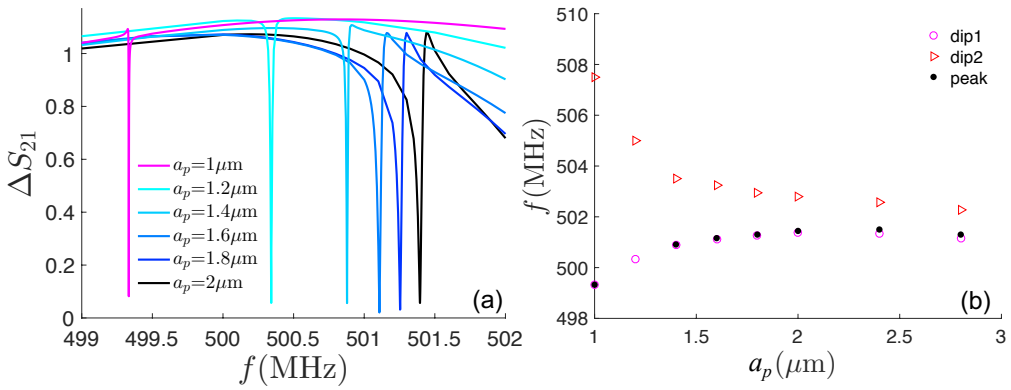

FIGURE 4.26 – (a)Normalized transmission spectra of Love waves for a_p varies from 1μm to 2μm. (b)Dips and peak frequencies as functions of the lattice constance a_p. $r_{p1} = 0.4\mu$m, $r_{p2} = 0.398\mu$m, $h = 1.2\mu$m

transmission spectra for different a_p are shown in Fig 4.27. Dotted blue and rose lines denote the single pillar dip frequencies with a periodicity of $2a_p$ and a radius equal to r_{p1} and r_{p2}, respectively. Fig 4.27(a) corresponds to the case $a_p = 1\mu$m, where the coupling of the pillars is so strong that the two dips stays all the way mismatched with their corresponding single pillar dip frequency. When a_p gets larger, the coupling becomes weaker. Fig 4.27(b) corresponds to the case of $a_p = 2\mu$m. Since this coupling effect decreases with the increase of radius mismatch, the dips almost coincide with the corresponding single pillar dip frequency in the case of $r_{p2} = 0.39\mu$m and 0.41μm. Strong coupling occurs in the radius region of $r_{p2} \in [0.398, 0.402]$ μm. Fig 4.27(c) shows the case of $a_p = 4\mu$m, where the coupling effect between the adjacent pillars is very weak. It can be seen that dip1 becomes shorter when r_{p2} approaches to r_{p1}.

4.3.2 pillar height mismatch

Since the pillar intrinsic mode is sensitive to the pillar size, the effects of pillar height is also studied by increasing the height of the second pillar $h2$ from $0.6005a_p$ to $0.604a_p$, while fixing $h1$ at $0.6a_p$. The two pillars are characterized by the same radius $r_{p1,p2} = 0.2a_p$. Fig 4.28 shows the evolution of dip1 and peak when we gradually modify

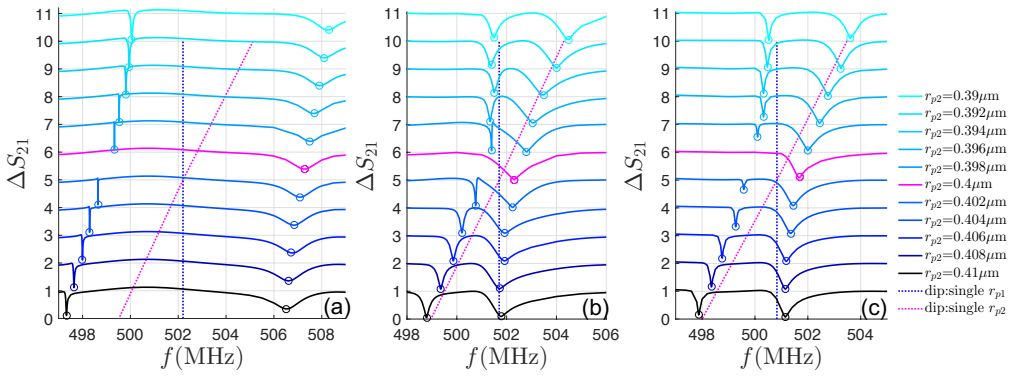

FIGURE 4.27 – Normalized transmission spectra of Love waves for a_p= (a)1μm, (b)2μm and (c)4μm, when gradually changing r_{p2} from 0.39μm to 0.41μm. Dotted blue and rose lines indicate the single pillar dip frequencies with a periodicity of $2a_p$ and a radius equal to r_{p1} and r_{p2}, respectively. r_{p1}=0.4μm.

the pillar height from $0.6005a_p$ to $0.604a_p$. It is found that the peak is relatively wider than that for the same radius mismatch in Fig 4.23(b), indicating a relatively weaker coupling induced by the height mismatch.

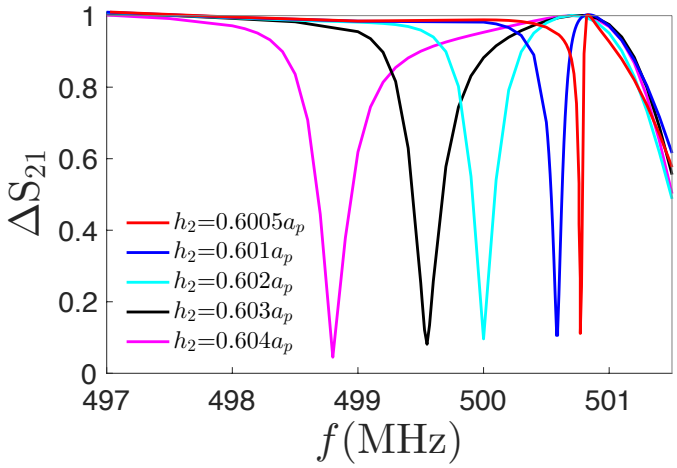

FIGURE 4.28 – Normalized transmission spectra for $h2$ varies from $0.6005a_p$ to $0.604a_p$. $h1 = 0.6a_p$, $a_p = 2\mu$m.

4.4 tunable passing band

From the investigations presented above we know that the different pillars give rise to separate dips, and that two lines of same pillars are able to either separate dips or widen one dip. Therefore it is conceivable to design a passing band by a simple combination of these two cases : two lines of alternating dissimilar pillars. Here in Fig 4.29 we present two passing band based on pillars differ in radius.

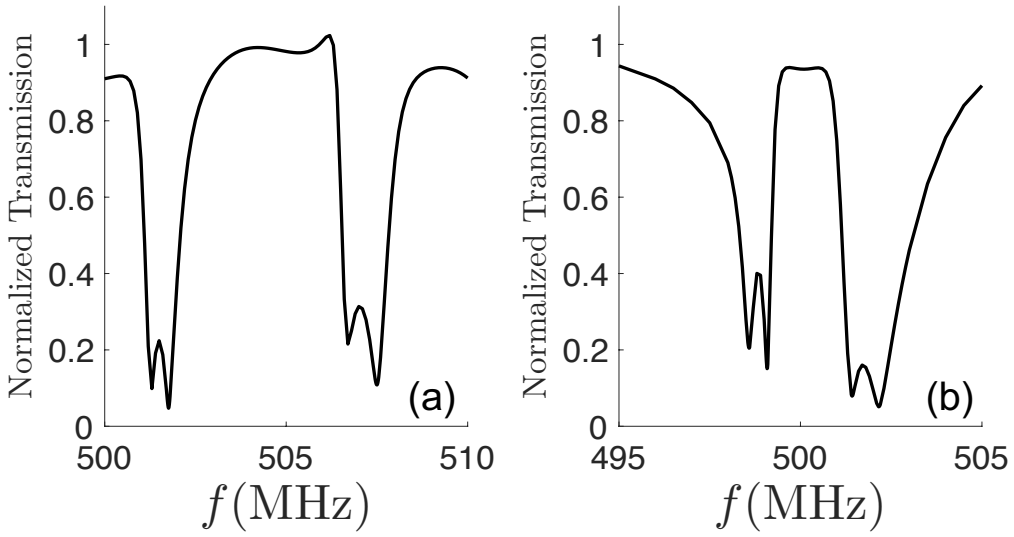

Figure 4.29 – Passing band formed by two lines of alternating dissimilar pillars with r_{p2} equals to (a) $0.19a_p$ and (b) $0.205a_p$. $r_{p1} = 0.2a_p$. $h = 0.6a_p$, $d = a_p$, $a_p = 2\mu$m.

In fact, the different radius are employed to determine the position of the dips, whereas the distance between the two pillar lines is used to design the width of the dip. In this way, we can realize a tunable passing band by only two lines of simple pillars.

4.5 Conclusion

In this chapter, the interaction of Love waves with one and two lines of cylindrical Ni pillars are investigated on the silica film deposited on the 90ST quartz substrate.

Firstly, pillar intrinsic torsional mode is demonstrated to be well excited by Love

waves. One line of identical pillars can give rise to a sharp transmission dip due to a destructive interference. The coupling between the adjacent pillars become weak when the periodicity along the y direction exceeds 2μm (i.e. $r_p/a_p<0.2$).

Secondly, acoustic analogue of Autler-Townes Splitting (ATS) and Fabry-Perot resonance of Love waves are first demonstrated in two lines of identical pillars by varying the distance between the pillar lines. ATS appears when the distance is smaller than the half wavelength and a strong coupling is aroused between the pillar lines, causing the pillar mode induced transmission dip to split into two dips with a transparency window in the middle. This coupling decreases with the increase of pillar distance. We demonstrated the different pillar vibration symmetries at the two dip frequencies, which lead to different dip widths. Fabry-Perot resonance exists at the positions where the distance between the pillar lines is a multiple of half wavelength. The proximity of Fabry-Perot resonance with pillar intrinsic mode gives rise to the cavity modes with transmission enhancement on the two edges of the single dip. We avoided to mix up the FP resonances with the cavity modes by presenting the different frequency variation with respect to the distance between the pillars.

Thirdly, the radius of one line of pillar is modified to detune the pillar resonant frequency. In the pillar coupling region, the coupling effect decreases with the increase of radius mismatch, and the two dips will rejoin their individual pillar mode frequencies. When the distance between the pillar lines is a multiple of half wavelength, Fabry-Perot resonance along with the two different pillars' resonances give rise to the Acoustically Induced Transparency (AIT). With similar transparency window in the transmission spectra, ATS and AIT phenomena are then fitted respectively with the corresponding formula models, showing good agreements. The fit parameters are demonstrated as functions of the geometrical parameter. The Akaike information criterion (AIC) is first used in acoustic system to quantitatively evaluate the quality of the fit models, which illustrates the transition from ATS to AIT as well as the periodicity of AIT by increasing

the distance between the pillar lines. The theoretical and analytical differentiation of ATS and AIT should be used together to discriminate the assignment of the observed spectrum to one or the other physical mechanism.

Next, two dissimilar pillars that alternate in a single line are demonstrated to raise two dips with a peak in middle. The first dip along with the peak give rise to a Fano resonance when the two pillars have a small geometrical mismatch and the coupling between the pillars is so strong that the dips are mismatched with their individual pillar mode frequencies. This resonance can be increasingly confined by reducing the periodicity along the y direction, with a Q-factor of up to $3{,}33\times10^5$. The results presented in this study could be used to potential acoustic applications such as signal processing, wave control, meta-materials and bio-sensors. The above phenomena can also be obtained by detuning the pillar height.

The resonant properties of local resonators and their coupling effects studied in this chapter can be used for further investigation on the interaction between different resonators, which will be presented in the next chapter.

Chapitre 5

Love Waves in Defect States

The introduction of defects into PnCs is at the origin of multiple applications such as waveguide [2, 93, 114], cavity [1, 55, 115], filter [5, 75] and multiplexer [116]. Most research on the defect modes is based on the bulk waves [1, 2, 5], Rayleigh waves [54] and Lamb waves [55, 72], while sensors, especially the bio-sensors, are based on the Love waves and shear horizontal Lamb waves, which are compatible with the liquid environment [15, 16] and leak less energy in the liquid. However, Lamb waves propagate on the extremely thin slabs, making them comparably fragile and therefore difficult to manipulate. Whereas Love waves exist in the guiding layer deposited on a semi-infinite substrate, which guarantees both the confinement of the energy and the toughness of the device, in comparison with the Lamb waves devices. In recent years, the partial band-gap effect of PnCs on Love waves has been reported and a reflective grating was then proposed[12, 131]. Nevertheless, the exploitation of Love waves interacting with the defect states in PnCs remains to be investigated.

Coupling modes have been investigated in both PnCs [116, 136, 168–171] and PtCs [158–162], exhibiting features such as energy transferring [116, 159, 169], absorption [168, 170], wave confinement [159] and frequency modulation [171]. Most of the research is based on the cavity/waveguide [116, 159, 171], cavity/cavity [161, 171] or waveguide/

waveguide [169] systems. Wang et al. [170] demonstrated the transmission cancellations due to the coupling modes of a 1D locally resonant PnC. Ohta et al. [160] studied the coupling between a PtC nanobeam cavity and a quantum dot. The emission peak of the quantum dot could be tuned by temperature to cross the cavity mode which splits into two peaks. In recent years, peak splitting phenomena have also been discussed in the coupling of two PnC cavities [171], giving rise to a capacity of frequency modulation as well as improved quality factors. We believe that it is conceivable to investigate similar effects in different PnC devices.

This chapter introduces defect states into the holey PnC by removing lines of holes from the guiding film perpendicularly to the propagation direction. New flat cavity modes are observed in the band gap of the perfect PnC and give rise to transmission peaks isolated from outside band. Geometrical parameters such as holes radius, cavity width and crystal size are discussed. Cavity modes in pillared and mixed PnCs are also observed. By introducing lines of pillars into the cavity, we studied the coupling between the pillars mode and the cavity modes. Single pillar line in the cavity is investigated by modifying the position of the pillar. Collective pillars give rise to extremely flat modes that lead to sharp transmission peak. When pillar mode frequency approaches the cavity mode, peak splitting effect is observed on the original cavity mode. The pillars are found to be able to significantly improve the quality factor and transmission of the cavity mode.

5.1 Supercell model with cavity

The resonator is realized by removing W lines of holes along the y direction in the PnC lattice, forming a cavity perpendicular to the propagation direction. A supercell containing $1\times(6 + W/a)$ unit cells is constructed and shown in Fig 5.1, with periodic boundary conditions applied in the x and y directions.

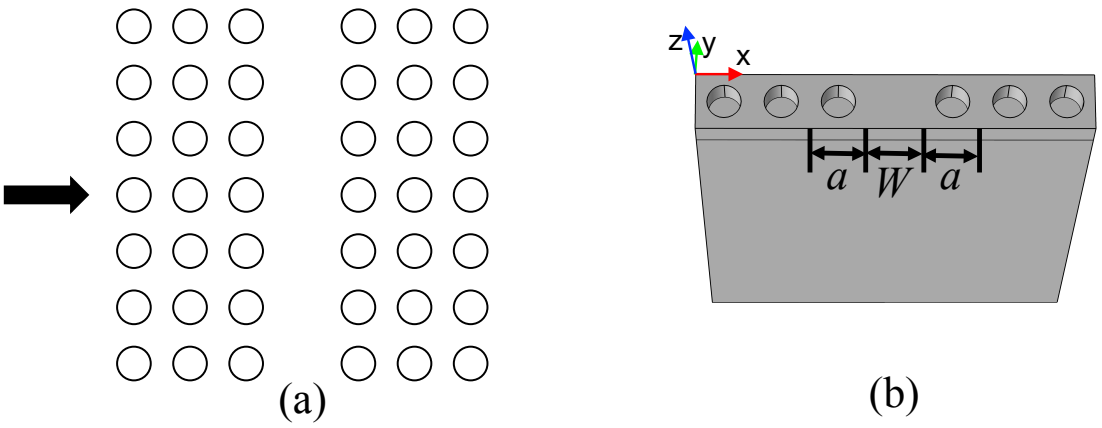

FIGURE 5.1 – (a) Schematic diagram of the PnC lattice containing a defect (cavity). The arrow denotes the direction of waves propagation ; (b) Supercell of the defect-included PnC containing $6+W/a$ unit cells, with $N_{PnC} = 3$ on each side of the cavity.

5.2 Band structure and transmission spectrum of supercell

5.2.1 Band structure calculation

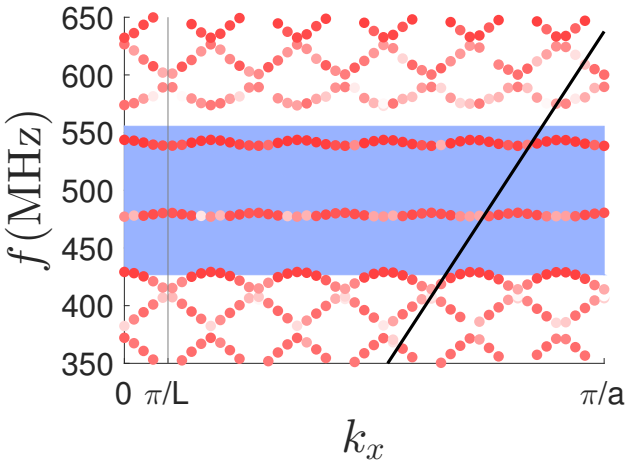

FIGURE 5.2 – (a) Repeated band structure of Love waves for an over-calculated wave vector of the supercell. Black line is the dispersion curve of the SH waves in substrate. Band gap of the perfect holey PnC is indicated in blue. $L = 6 + W/a$, $W = 5a$, $r_h = 0.2a$. $H = 0.6a$, $a = 4\mu$m, $N_{PnC} = 3$

First we set the cavity width to $W = 5a$. The band structures of Love waves in the

PnCs containing the defect are calculated along Γ-X. Love modes are selected by the same formulas (3.2 and 3.3) introduced in chapter 3. Note that the Γ-X will be 11 times smaller as we calculate for a supercell which is 11 times longer. That is, k_x in the irreducible Brillouin zone will be 11 times shorter, since the eigenfrequencies will be repeated in the inner part of the supercell. As a result, the band structure will be folded and repeated 11 times in the rest part. Fig 5.2 shows an example of the repeated band structure for an over-calculated wave vector.

5.2.2 Cavity modes in holey PnC

The Love waves band structures of the defect-containing PnCs are shown in Fig 5.3(a) and (d), for r_h/a=0.2 and 0.3 respectively. It is found that new flat modes, referred to as defect modes or cavity modes, appear inside the previously observed band gaps. These band structures are attributed to the coupling between the cavity and the perfect PnCs. Two cavity modes are predicted in Fig 5.3(a), respectively at 479.5 MHz and 538.5 MHz. In Fig 5.3(d), another two are at 401.4 and 475.9 MHz.

The corresponding displacement fields of the cavity modes are shown in Fig 5.3(c) and (f). The displacements are concentrated in the center of the model (in the cavity) and attenuated at both ends. Inside the cavity, the displacements are uniform throughout the defect with maximums near the edges. In both cases, one of the cavity mode is symmetrical and the other one is antisymmetric. It can be seen that the cavity modes for $r_h = 0.2a$ are more confined to the surface than that for the radius of $0.3a$. In Fig 5.3(d), the flat mode on the upper limit of the band-gap region is not referred to as a cavity mode, since its displacement is no more concentrated in the cavity. Fig 5.3(b) and (e) show the normalized transmission spectra with and without the cavity in the PnCs, for the two different radius, calculated with 4 holes on each side of the cavity (N_{PnC}=4). For $r_h = 0.2a$, two obvious peaks are found at 478 MHz and 540.6 MHz, consistent with the predicted resonant frequencies with small shifts due to the numeric mesh

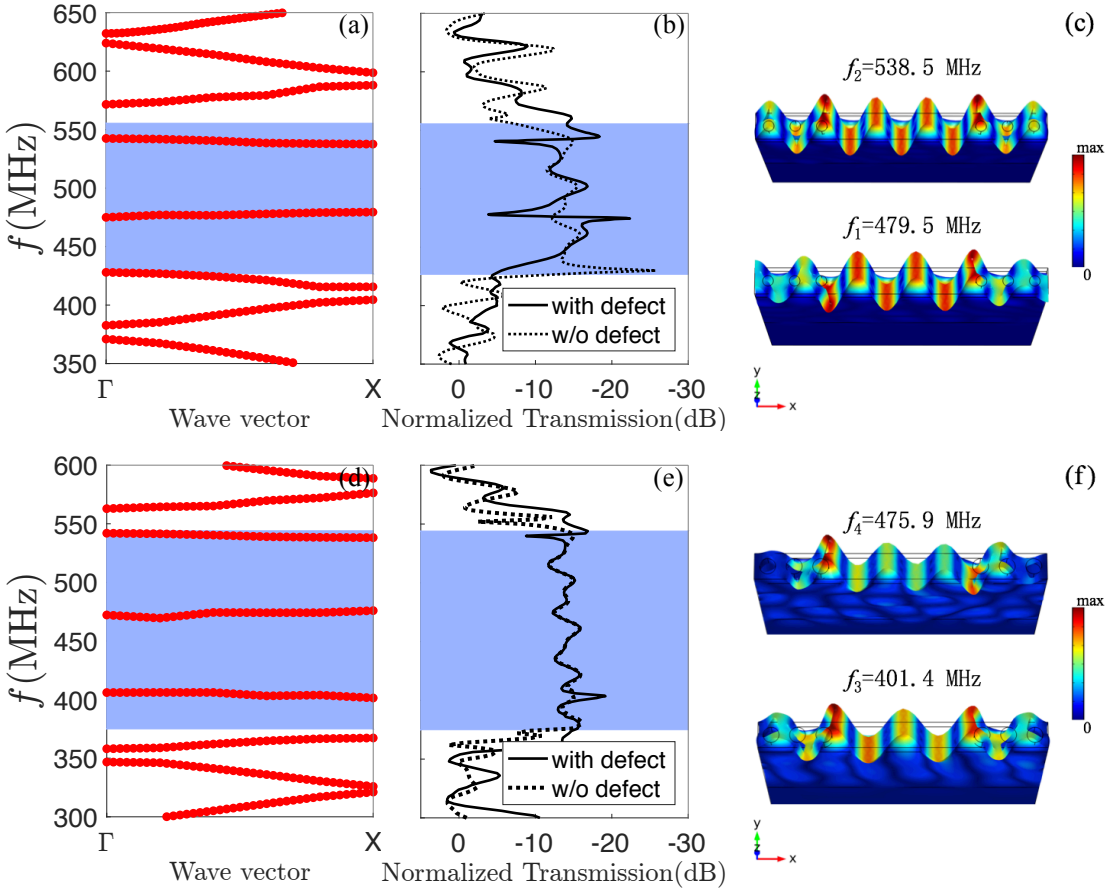

FIGURE 5.3 – Band structures of Love modes on the defect-containing PnCs in the Γ-X direction around the band-gap region with (a)$r_h = 0.2a$ and (d)$r_h = 0.3a$, Blue zones are the predicted band gaps of the perfect PnCs ; Normalized transmission spectra of Love waves with and without the defect (cavity) for (b)$r_h = 0.2a$ and (e)$r_h = 0.3a$, with $N_{PnC} = 4$; Displacement fields of the supercells at the resonant frequencies of the cavity modes for (c)$r_h = 0.2a$ and (f)$r_h = 0.3a$. $W = 5a$, $H = 0.6a$, $a = 4\mu$m

construction process of the FEM. These two flat cavity modes give rise to the highly confined transmission peaks. This means the cavity enables the propagation of waves that are otherwise forbidden in the perfect PnC. Each of the two transmission peaks possesses an asymmetric line-shape. The 1^{st} transmission peak starts with an anti-resonance and ends with a resonance, while the 2^{nd} transmission peak possesses the opposite behavior. In Fig 5.3(e) for $r_h = 0.3a$, only a small dip is found at 403.2 MHz,

corresponding to the first defect mode in the band-gap region. This resonance is rather difficult to recognize from the band-gap bottom. Furthermore, no resonance has been found at the 2^{nd} predicted resonant frequency, which is referred to as a deaf mode. These phenomena might be resulting from the less confinement of the cavity modes for $r_h/a = 0.3$. In other parts of the band-gap region, a superposition of the two curves is observed.

5.3 Geometrical parameters consideration

5.3.1 holes radius effects

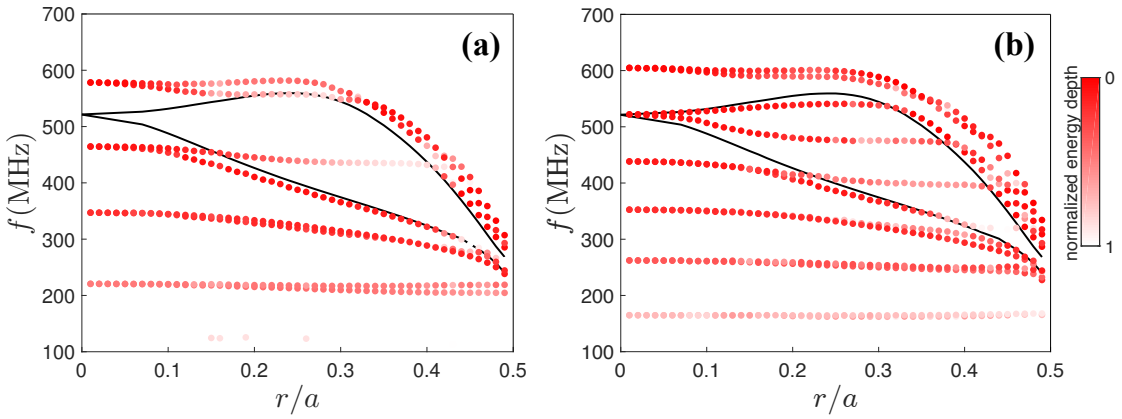

FIGURE 5.4 – Love modes eigenfrequencies of the defect-containing PnC as a function of the hole radius. Inside the two black curves delimiting the band-gap zone of the perfect PnC are the cavity modes. Red-white colors denote the normalized energy depth (NED) of the Love modes. Red indicates a good confinement to the surface. The cavity width is (a) $W = 2a$ and (b) $W = 5a$. $r = 0.2a$, $H = 0.6a$, $a = 4\mu$m, $N_{PnC} = 3$.

Fig 5.4(a) and (b) shows the eigenfrequency-radius relation of a 2 and 5 holes removed supercell (W=2a and 5a), respectively, with 3 holes on each side of the cavity (N_{PnC}=3), calculated at the limit of the BZ (point X). Between the two black curves is the band-gap region of the perfect PnC, which has been presented by Fig **??**(a) in Chapter 3. For the cavity width $W/a = 2$, only one cavity mode is observed. It cuts through the

band gap with the increase of holes radius, and its frequency is little influenced by the holes radius. However, the waves become less confined to the surface as the red gets less intense.

As for the cavity width $W/a = 5$, two cavity modes are already in the band-gap region when r_h/a is near 0. They are separated with a certain distance as the radius increases. The two modes below penetrate into the band gap and become cavity modes. It seems that the four cavity modes have a tendency to reach a similar distance from each other, referred to as mode spacing, the same way as the Love modes with r_h/a close to 0. Once this distance is reached, the lower external modes will cut in and their frequencies will be little affected by the normalized radius of the PnC. The modes outside are disturbed when approaching the band gap, and begin to surround this region. Nevertheless, a larger radius of the holes and a lower order of the cavity modes result in a deeper mode energy (less confined to the surface), leading to a drop of energy transmission. The lowest cavity mode that appears around r_h/a=0.45 becomes even difficult to recognize. This explained the different transmission peaks for the $r_h = 0.2a$ and $r_h = 0.3a$ defect-containing PnCs presented in Fig 5.3.

Although the number and frequencies of cavity modes are different for the two cavity width, one can draws some common points to understand the hole radius effects : the radius has little influence on the cavity frequencies. However, the waves confinement and hence the transmission performances are strongly dependent on the holes radius.

5.3.2 Cavity width effects

Fig 5.5 is the eigenfrequency-cavity width relation of a supercell with $r_h = 0.2a$, calculated at point X. Inside the band gap denoted in blue are the cavity modes. As the cavity width increases, the frequencies of cavity modes decrease and modes with higher order appear (denoted by numbers). Apart the 1^{st} cavity mode, other modes are in pairs, and each pair is twisted outside the band-gap region and mutually merged. In our

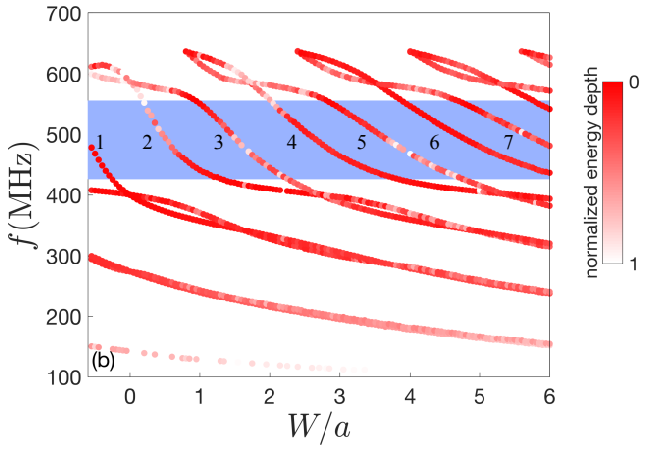

FIGURE 5.5 – Love modes eigenfrequencies as a function of the cavity width. Blue zone is the predicted band gap of the perfect PnC. The numbers denote the order of the cavity modes. $r = 0.2a$, $H = 0.6a$, $a = 4\mu$m, $N_{PnC} = 3$.

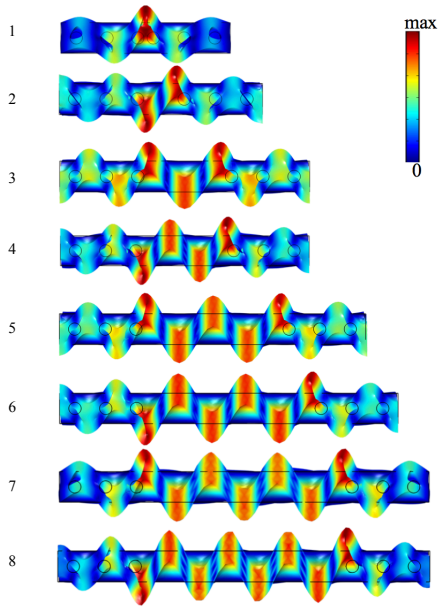

FIGURE 5.6 – Displacement and deformation in xy plane corresponding to cavity modes of different orders (from 1 to 8). $r_h = 0.2a$, $H = 0.6a$, $a = 4\mu$m, $N_{PnC} = 3$.

range of measurement (for W from $-0.6a$ to $6a$), the confinement of Love modes in the band-gap region is better for a larger cavity width ($W > 3a$) or a squeezed cavity width ($W < -0.3a$) . As the order of the cavity modes increases, the modes become less inclined,

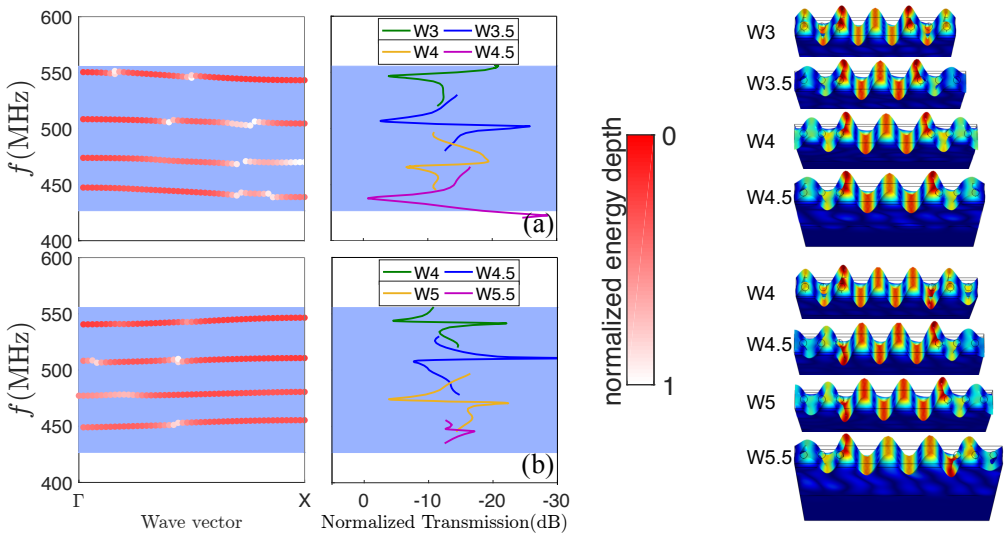

Figure 5.7 – Normalized transmission spectra for the defect-included holey PnC on the (a) 5^{th} and (b) 6^{th} cavity mode. Corresponding dispersion curve for each peak is shown on the left. Blue zones denote the predicted band gap of the perfect PnC. The displacement field of each mode at point X is shown on the right side. $r_h = 0.2a$, $H = 0.6a$, $a = 4\mu$m, $N_{PnC} = 4$.

providing a larger cavity width range for each mode inside the band-gap region. For example, from $1a$ to $2.3a$ for the 3^{rd} cavity mode, and from $3a$ to $4.7a$ for the 5^{th} cavity mode. The wave period in the cavity increases by one-half for every higher mode order as shown in Fig 5.6, resulting in an alternating symmetry as the mode order increases.

According to the cavity modes predictions in Fig 5.5(b), the transmission peaks of cavity modes can be displaced inside the band-gap region by changing the width of the cavity. The fifth and sixth cavity modes are shown as examples in Fig 5.7. As the cavity width increases, the resonant frequency of each cavity mode decreases, with different occurring order of resonance and anti-resonance on the transmission peaks. This proved the possibility of manipulation on the position of transmission peaks.

However, significant changes in shape are observed. This can be explained after carefully observing the dispersion curve of each peak. It is found that the group velocity is negative for the 5^{th} cavity mode and is positive for the 6^{th} cavity mode. This is not

influenced by the change in cavity width. However, the continuity and homogeneity of the dispersion curves are altered. A well confined (denoted in red) and smooth dispersion curve gives rise to a high and sharp transmission peak, see the cases of $W = 4a$ and $W = 5a$ for the 6^{th} mode in Fig 5.7(b). If the mode is leaky (denoted in white) somewhere in the dispersion curve and causes the curve to break (discontinuity or non-smoothness), the corresponding transmission peak might be affected, in terms of height and/or sharpness. The transmission peak of the 6^{th} mode is perturbed on a $W = 5.5a$ cavity, exhibiting a shift at the resonant frequency compared to the dispersion curve, which might be another explication of its shortened peak. A confined mode at point X is hence only a prerequisite for a high and sharp peak. The dispersion curves for the 6^{th} cavity mode are more compact than the curves for the 5^{th} mode, as it possesses a larger range of cavity width within the band gap. Displacement field u_y of the 1^{st} and 2_{nd} cavity modes with N_{PnC} varies from 4 to 8 are shown in Fig 5.9.

5.3.3 Crystal size effects

Fig 5.8(a) shows the influences of the number of PnC holes (the crystal size) on the formation of peaks. As N_{PnC} augments, the band-gap effect increases and it becomes harder for the waves to penetrate through the crystal, so the cavity peaks become shorter and sharper. The 1^{st} transmission peak (at 478 MHz) drops more quickly than the 2^{nd} peak, due to the enhanced band-gap effect in the center of the band-gap region, and eventually disappears after N_{PnC} exceeds 7. On the other hand, insufficient crystal size (N_{PnC} below 4) results in the blunt peaks, i.e., insufficient to filter out waves in the band-gap range other than the cavity frequencies.

The changes in quality factors (Qs) of the two peaks are shown in Fig 5.8(b). As N_{PnC} augments, the Qs have a tendency to increase and then decrease. The Q of the 1^{st} resonant mode decreases earlier due to its rapidly shortened peak. The Q of the 2^{nd} peak reaches a maximum (1100) at $N_{PnC} = 7$, where a highly confined cavity mode appears at

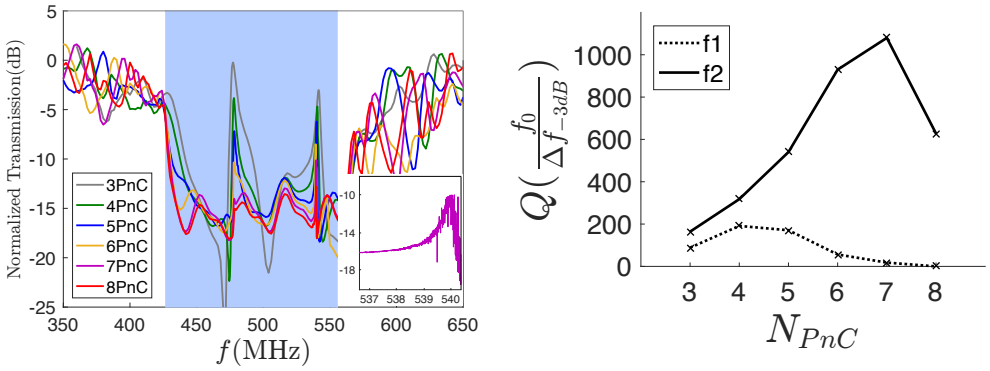

Figure 5.8 – (a)Transmission spectra of the PnC containing the defect, with the number of PnC holes on each side of the cavity varies from 3 to 8. Blue zone is the predicted band gap of the perfect PnC. Inset shows the zoomed peak at 540 MHz for $N_{PnC} = 7$; (b) Quality factors of the defect modes as a function of the number of PnC holes on each side of the cavity. $W = 5a$, $r = 0.2a$, $H = 0.6a$, $a = 4\mu$m.

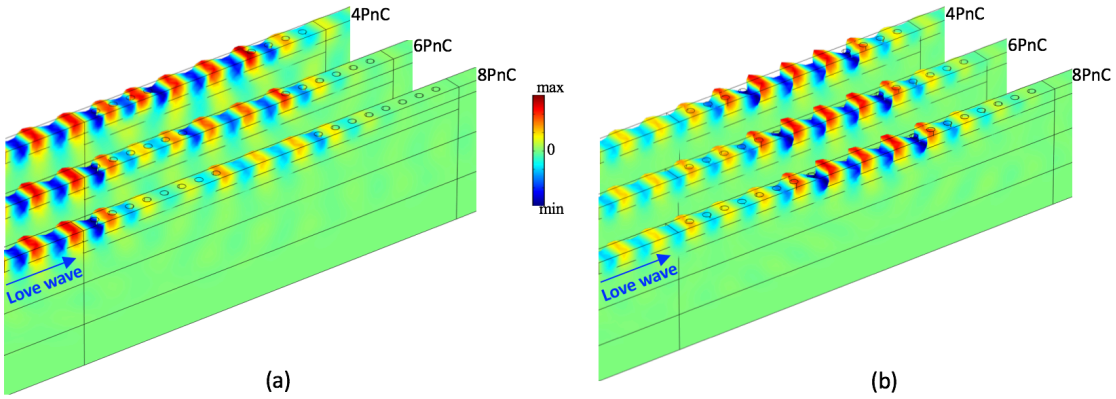

Figure 5.9 – Displacement field u_y of the (a) 1^{st} cavity mode (around 478 MHz) and (b) 2^{nd} cavity modes (around 540 MHz) with $N_{PnC} = 4$, 6 and 8. $W = 5a$, $r = 0.2a$, $H = 0.6a$, $a = 4\mu$m.

540 MHz, shown in the inset of Fig 5.8(a). It begins to decrease at $N_{PnC} = 8$, owing to the shortened peak. For this reason, the crystal size should be properly chosen to keep a good quality factor as well as an isolation of the cavity modes. It is further confirmed that in our range of measurement ($3 \leq N_{PnC} \leq 8$), the eigenfrequencies of cavity modes are independent of the crystal size, with only slight frequency shifts on the transmission peaks, which is mainly due to the mesh construction of the FEM.

5.4 Cavity modes by different lattices

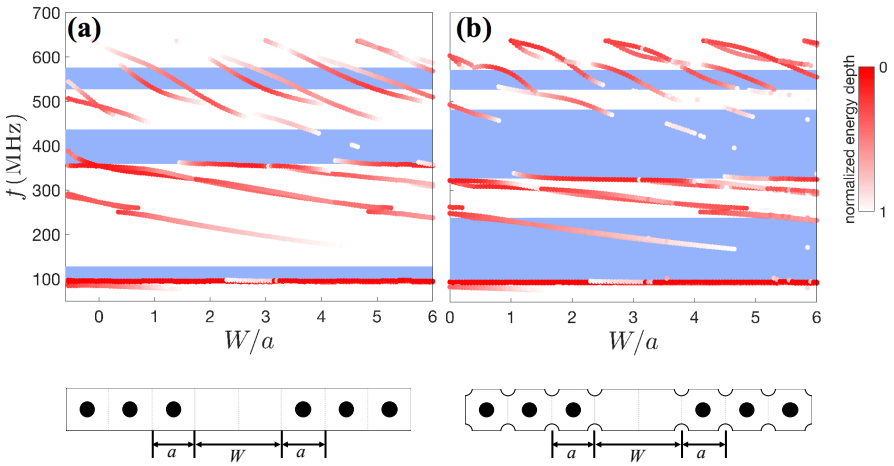

FIGURE 5.10 – Love modes eigenfrequencies as a function of the cavity width based on (a) pillared PnC and (b) D-PnC. Blue zone is the corresponding predicted band gap of the two perfect PnCs. $r_h = r_p = 0.2a$, $h = 0.6a$, $H = 0.6a$, $a = 4\mu$m, $N_{PnC} = 3$

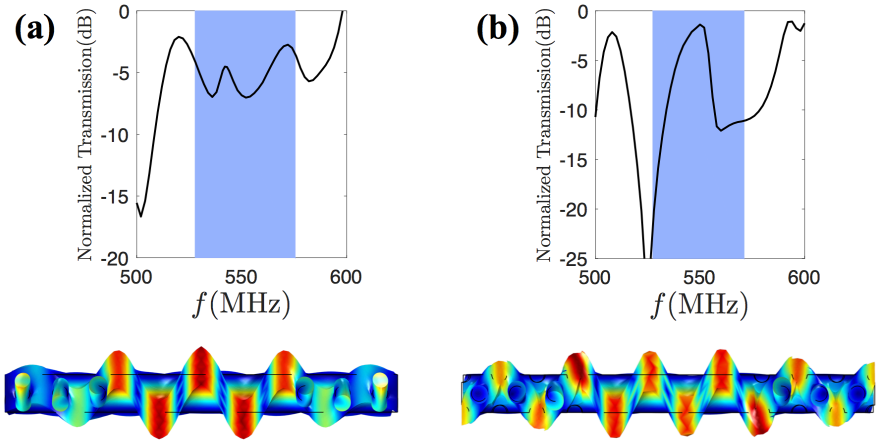

FIGURE 5.11 – Transmission spectra for the defect-included (a) pillared PnC with $W = 4.5a$ and (b) D-PnC with $W = 5a$. Corresponding displacement fields are shown aside. Blue zones denote the corresponding band gap of the two perfect PnCs. $r_h = r_p = 0.2a$, $h = 0.6a$, $H = 0.6a$, $a = 4\mu$m, $N_{PnC} = 4$.

Cavity modes are also demonstrated for the other PnCs (based on pillars and mixed holes/pillars). Since the cavity mode frequency is related to the cavity width W, Fig 5.10

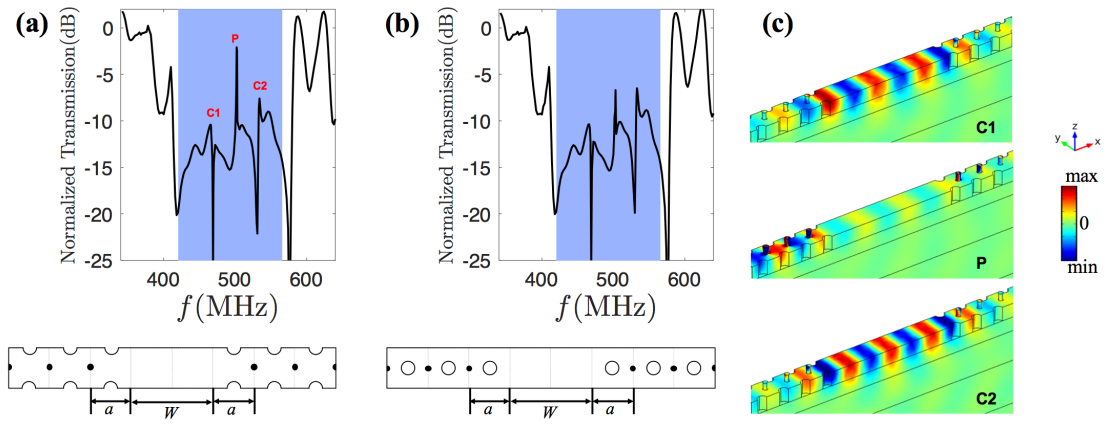

Figure 5.12 – Transmission spectra for the defect-included (a) Ds-PnC and (b) Ls-PnC with $W = 5a$. Blue zones denote the corresponding band gap of the two perfect PnCs. (c) Displacement fields U_y of the cavity modes C1, C2 and pillar mode P for the defect-included Ds-PnC. $r_h = 0.2a$, $r_p = 0.1a$, $h = 0.3a$, $H = 0.6a$, $a = 4\mu$m, $N_{PnC} = 4$.

shows the eigenfrequency-W relation of the supercells of the pillared PnC and D-PnC with $r_h = r_p = 0.2a$, calculated at point X. It can be seen that the cavity modes are well confined in the Bragg band gap region (at higher frequency range), which means the cavity modes require a periodicity of the crystals. Corresponding transmission spectrum and displacement field are shown in Fig 5.11, calculated on the cavity widths close to the previous case for the holey PnC. However, the transmission peaks are less confined.

The cavity modes of the Ds-PnC and Ls-PnC with the same cavity width as the holey PnC are demonstrated and are shown in Fig 5.12(a) and (b), respectively. It can be seen that they are combinations of the cavity modes of the defect-containing holey PnC and the local resonant mode of the pillar. However, the intensity of the cavity modes are decreased compared with those of the defect-containing holey PnC. The displacement field of these three modes for the defect-included Ds-PnC are shown in Fig 5.12(c). We shown the SH component U_y that is more adequate to present the pillar torsional mode as well as the SH waves. It can be seen that the cavity modes (C1 and C2) are similar as that of the defect-containing holey PnC. As for the pillar mode P, the waves are highly confined in pillars, instead of in the cavity. No coupling is found between the cavity

modes and the pillar mode. However, when the pillar mode frequency becomes close to a cavity mode frequency, these two modes can be coupled to show different behaviors. The details of this phenomenon will be discussed in the following section.

5.5 Coupling between defect states and local resonance

5.5.1 single pillar line in cavity

The goal of this section is to provide in a comprehensive way a numerical study of the coupling effects of a single pillar line introduced into a cavity interacting with Love waves. We profit from the cavity based on holey PnC that has been introduced above, where the cavity modes has been predicted for every different cavity width.

Since our pillar (same pillar as Chapter 4) works around 500 MHz, we set the cavity width W to $4.5a$ as a cavity mode is predicted near 500 MHz, where $a = 4\mu$m is the lattice constant of the holey PnC. In this way, the pillar is likely to be coupled to the cavity mode. The normaliezed transmission spectrum is presented in Fig!5.13(a). As we can see, two cavity modes are in the band-gap region of the perfect holey PnC that is denoted in blue. The seconde cavity mode, which has a shorter peak than the first cavity mode, is at 507.5 MHz. To well match this frequency, we adjusted out pillar radius to $0.18a_p$, with the pillar height unchanged : $h = 0.6a_p$ with $a_p = 2\mu$m. The guiding layer thickness is fixed at 2.4μm.

The displacement field of this cavity mode is shown in Fig 5.13(b). This cavity mode is symmetric with respect to the center of the cavity. Here we divide the cavity into two parts according to the displacement field : red parts where the center is marked as M, is a max/min displacement ; gray parts where the center is marked as N is a zero displacement, as indicated in in Fig 5.13(c). Then, the pillar will be placed in different parts in the cavity.

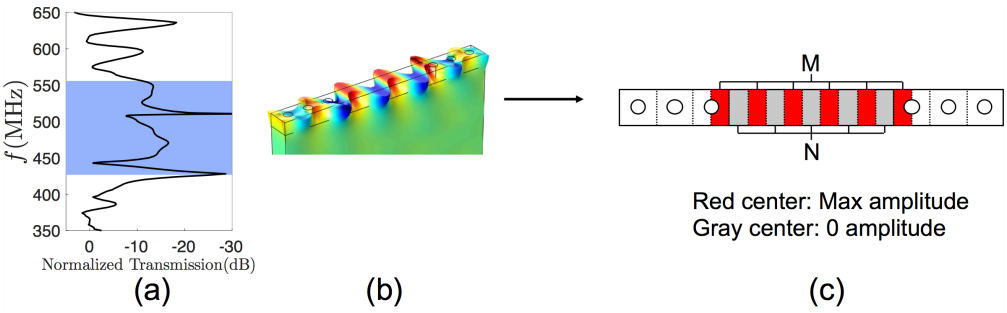

FIGURE 5.13 – (a) Transmission curve of Love waves for cavity with $W = 4.5a$; (b) u_y of the cavity mode at 507.5 MHz; (c) Schematic division of cavity according to the amplitude of displacement. The centers of red/gray parts, marked as M/N, denote the max/zero amplitude. $r_h = 0.2a$. $H = 0.6a$, $a = 4\mu$m.

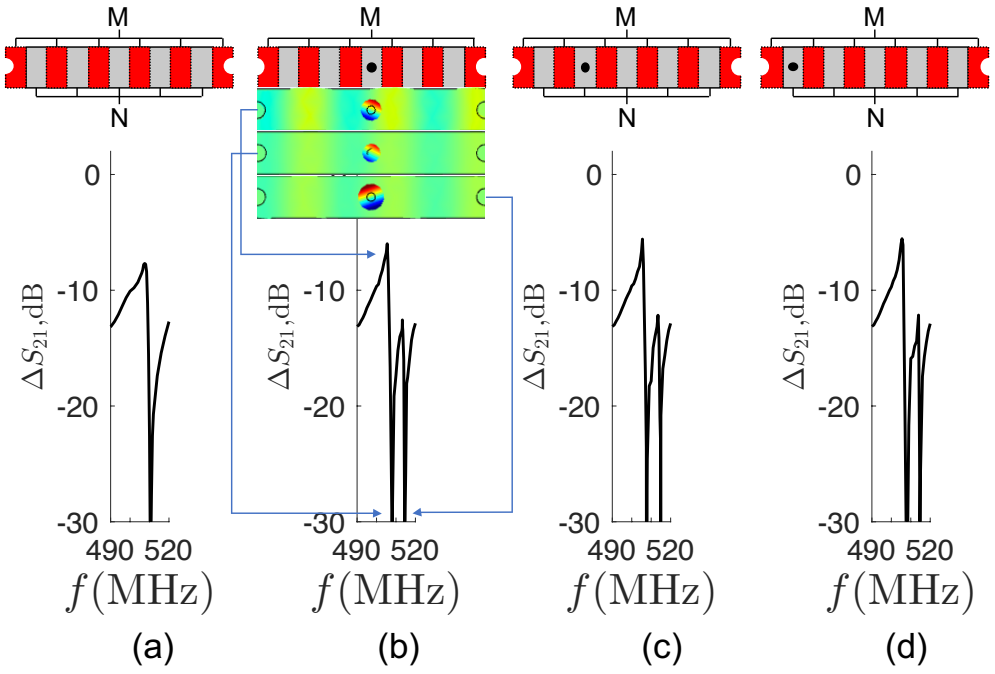

FIGURE 5.14 – (a) Zoom of the transmission curve of Love waves for the cavity mode at 507.5 MHz. (b)(c)(d) Transmission spectra when a pillar is added at three different N. Pillar position is presented by the cavity division diagram on top of the transmission spectra. u_y of the corresponding peak/dips are shown for the first position r_h=0.2a, r_p=0.18a_p, H=2.4μm, $h = 0.6a_p$, $a = 4\mu$m, $a_p = 2\mu$m

Firstly, the pillar is placed in the center of the gray parts. The normalized transmission spectra are shown in Fig 5.14. Since the cavity mode is symmetric, we only study the

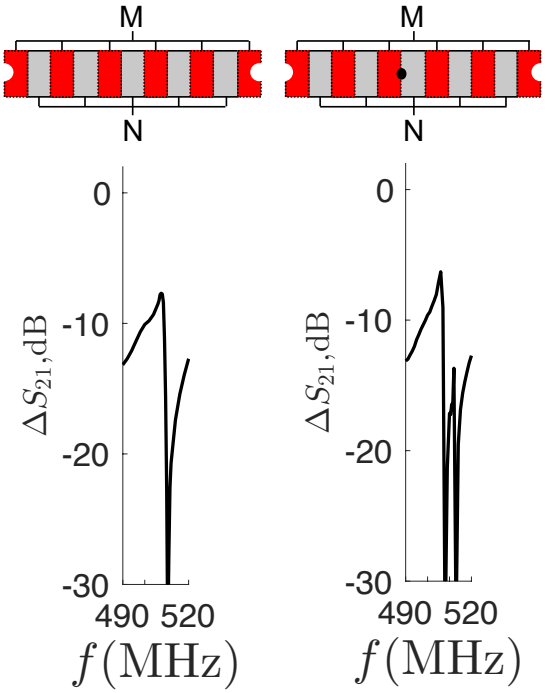

FIGURE 5.15 – Transmission spectrum when a pillar is added in the center of a N and M. Transmission without pillar is shown aside as reference.

first three positions. Corresponding pillar positions are shown above the transmission spectra.

It can be seen that the inserted pillar has given rise to an additional dip on the side of the cavity mode, with a small improvement on the cavity mode peak. The cavity mode frequency has decreased a little due to the added mass as well as a degeneracy of the cavity mode. For the three different N, the transmission curves are almost the same. u_y of the peak and two dips are shown for the first case. It is found that the cavity mode are coupled to the pillar mode for both peak and dips, and the displacement fields are quite similar, only with different amplitude in pillar and in guiding layer : for the peak of cavity mode, both the pillar and guiding layer present a large amplitude, while the dip of the cavity mode has only a small amplitude, which is reasonable for the waves propagation. Whereas at the dip of the pillar mode, great amplitude is found in the

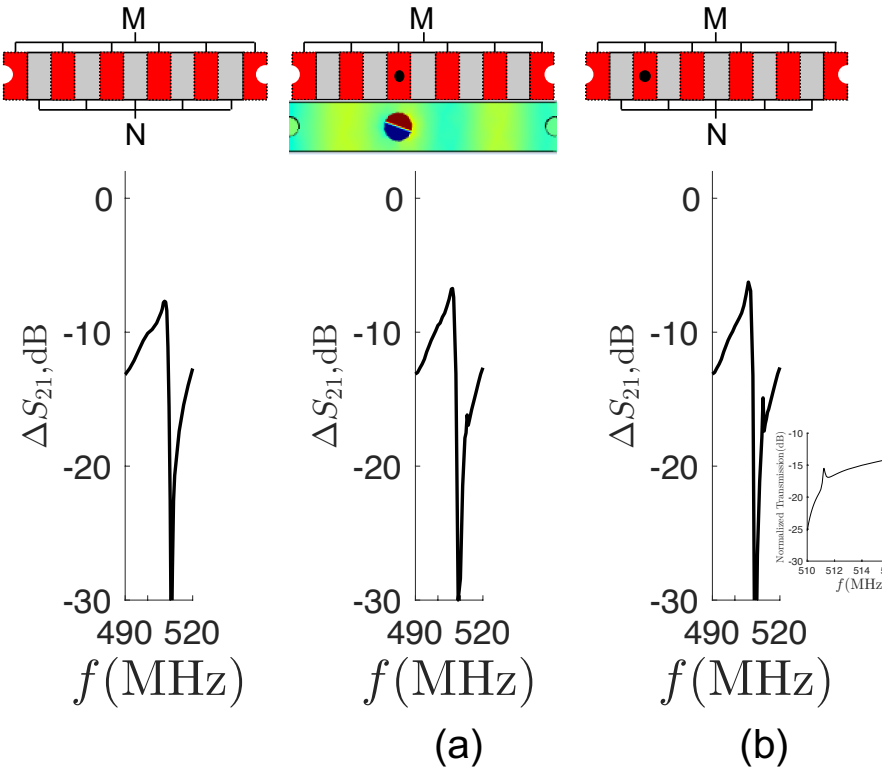

FIGURE 5.16 – (a)(b) Transmission spectra when a pillar is added at two different M. u_y of the pillar induced peak is shown for the first position. Transmission without pillar is shown on the left as reference.

pillar while the displacement in the guiding layer is as weak as for the cavity mode dip. This pillar mode appears like the case that we found for the single pillar line in Chapter 4.

The position of the pillar is then changed to the center of N and M, noted as C. Since the different cases for C position give almost the same results, we only present one center position, as shown in Fig 5.15. This structure also arouses an additional dip beside the cavity mode, since the torsion mode can still be excited. However, it is found that the pillar mode has moved closer to the cavity mode.

Next, the pillar is placed at M positions, where the torsional mode is unlikely to be excited, since they are positions where there is no displacement difference on the two

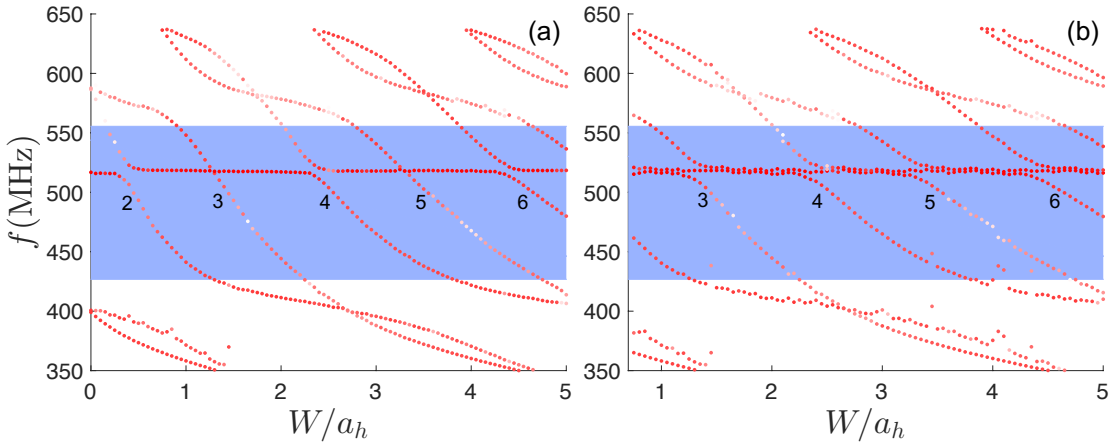

FIGURE 5.17 – Love modes eigenfrequencies as a function of the cavity width when (a) a pillar is placed in the center of the cavity; (b) two pillars are inserted respectively at the two edges of the cavity. Blue zone is the predicted band gap of the perfect holey PnC. The numbers denote the order of the fundamental cavity modes. r_h=0.2a, r_p=0.18a_p, H=2.4μm, h = 0.6a_p, a = 4μm, a_p = 2μm. Holey PnC size is three on each side of the cavity.

sides of the pillar. Same as the cases for N positions, we only study the left two parts due to the symmetry. The red part next to the hole is not studied since the pillar would be superimposed on the hole. Fig 5.16 shows the corresponding transmission curves. The dip for the pillar mode has disappeared as we predicted. However, it is remarkable that a small peak appears at the torsional mode frequency. The zoom of this peak are shown aside as well as the corresponding displacement field. It can be seen that the torsional mode is excited for the peak, except that the waves in the guiding layer has changed its phase after passing through the pillar. As a result, the displacement in the guiding layer has become totally different from the cavity mode. This phenomenon can be explicated as an effect of the pillar which acts as a second source and emits another wave. That means the pillar can resonate even if the outside excitation is not favorable for its resonance. Additionally, the M position near the edge of the cavity appears to be more favorable for the peak excitation.

These pillar-cavity coupling effects can be understood from an overview diagram

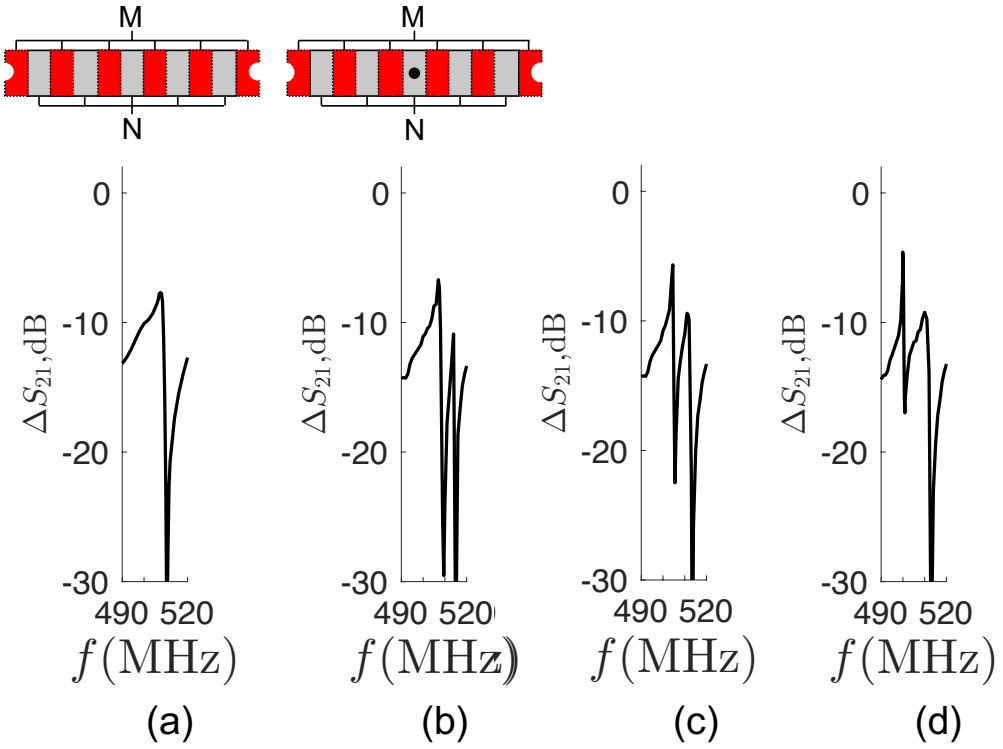

FIGURE 5.18 – Transmission spectra of Love waves when the pillar is at N. The pillar radius is (b) $0.18a_p$, (c) $0.19a_p$, (d) $0.2a_p$. FIgure (a) serves as reference.

presented by Fig 5.17, where we found exactly the same cavity modes as we showed by Fig 5.10 in Chapter 5, except that the pillar intrinsic mode appear at its resonant frequency (the straight line around 500 MHz) and become coupled to the cavity modes. The fundamental cavity mode orders are indicated by the numbers. Fig 5.17(a) shows the case of one pillar placed in the center of the cavity. Since the symmetry of cavity modes alternates with the increase of mode order (asymmetric for the 2^{nd}, 4^{th} and 6^{th} cavity modes ; symmetric for the 3^{rd} and 5^{th} cavity modes), the pillar position (of N or M) is alternative, i.e. the pillar is at N position for the 2^{nd}, 4^{th} and 6^{th} cavity modes while is at M position for the 3^{rd} and 5^{th} cavity modes. Therefore, the pillar is excited and coupled to the even cavity modes but not to the odd ones. These coupling has induced the avoided crossing and one cavity mode splits into two. This can explicate the same

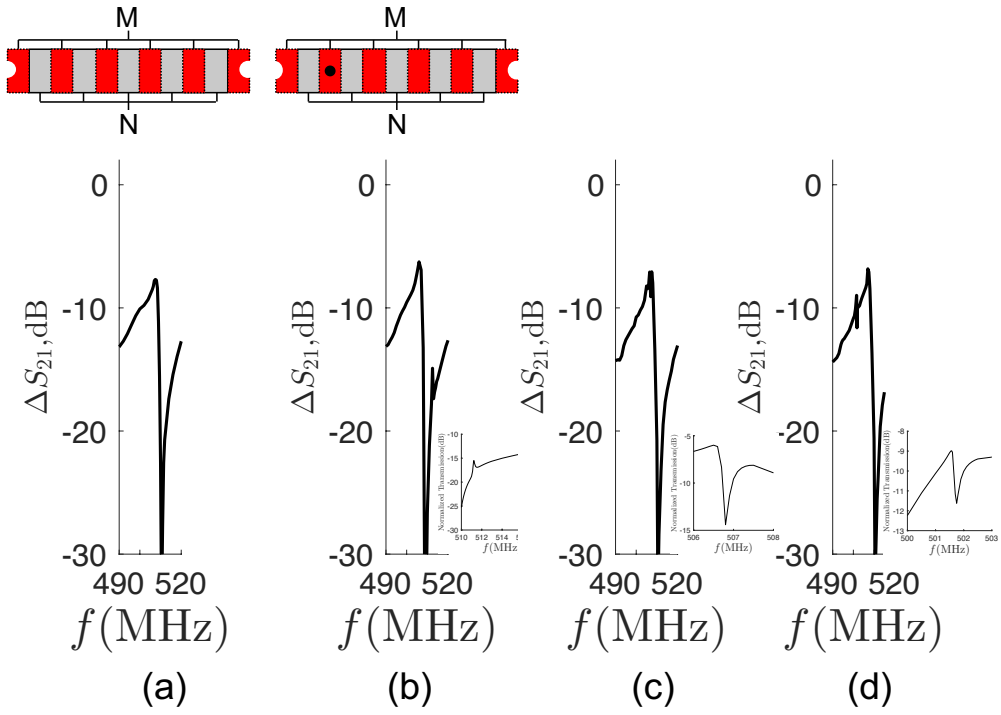

FIGURE 5.19 – Transmission spectra of Love waves when the pillar is at M. The pillar radius is (b) $0.18a_p$, (c) $0.19a_p$, (d) $0.2a_p$. FIgure (a) serves as reference.

displacement field between the two resonances in Fig 5.14(b). Fig 5.17(b) is the case of two pillars inserted at the two edges of the cavity, which means both the pillars are at N positions of the cavity modes. Therefore, the pillars are excited and coupled to every cavity modes. The cavity mode splits into two modes with a pure pillar mode in the center of the two modes.

If we gradually change the pillar size, for example the radius, this pillar mode can be displaced so as to see more clearly how it is coupled to the cavity mode. Fig 5.18/5.19 shows the transmission spectra of the coupled cavity modes for r_p equals to $0.18a_p$, $0.19a_p$ and $0.2a_p$, respectively, when the pillar is at N/M position. It can be seen that when the pillar is at N position, the pillar mode is gradually displaced around the cavity mode. By comparing these three cases in Fig 5.18, we can see that when the pillar mode is on the side of the cavity anti-resonance (case for $r_p = 0.18a$), the pillar mode not only

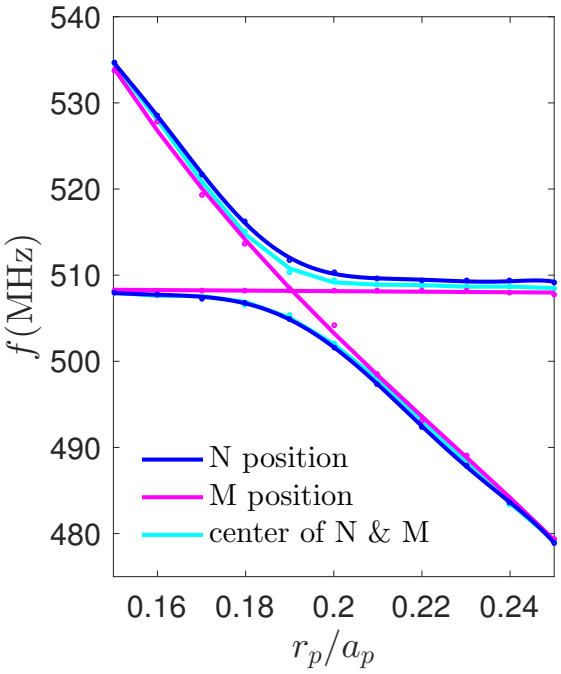

FIGURE 5.20 – Anti-crossing / crossing lines for a pillar coupled / uncoupled to the cavity mode. Love modes eigenfrequencies as a function of the pillar radius when a pillar is inserted at an N position (blue lines), a M position (rose lines), or in the center of N and M positions (cyan lines).

gives rise to a transmission dip, but also a small peak, as the cases for $r_p = 0.19a_p$ and $r_p = 0.2a_p$. This pillar induced resonance is like a vertical disturbance on the cavity mode, leaving the cavity mode line-shape to continue after this interruption. One interesting point is that when the pillar mode matches well the cavity peak, we come to dig a dip in the center of the peak (case for $r_p = 0.19a_p$). When the pillar is at M position (Fig 5.19), the small peak is also displaced accordingly. Additionally, in the insets of the zoomed transmission curves, we found that an anti-resonance appears for the cases $r_p = 0.19a$ and $r_p = 0.2a$. These behaviors can be grouped and represented by Fig 5.20. When the pillar is at N position, the cavity mode is coupled to the pillar mode and we obtain the blue anti-crossing lines, which correspond to the two resonances in the transmission spectra (see Fig 5.18). When the pillar is at M position, the cavity mode is uncoupled to the pillar mode and crosses each other. Thus we obtain the rose crossing lines, where

the horizontal straight line represents the cavity mode and the declined line denotes the pillar intrinsic mode. When the pillar is in the center of N and M, we also obtain two resonances with a slightly smaller frequency difference compared with that for the case of a pillar at N position.

5.5.2 Multiples pillar lines in cavity

In this section the number of pillars will be gradually increased to find more efficient coupling performance.

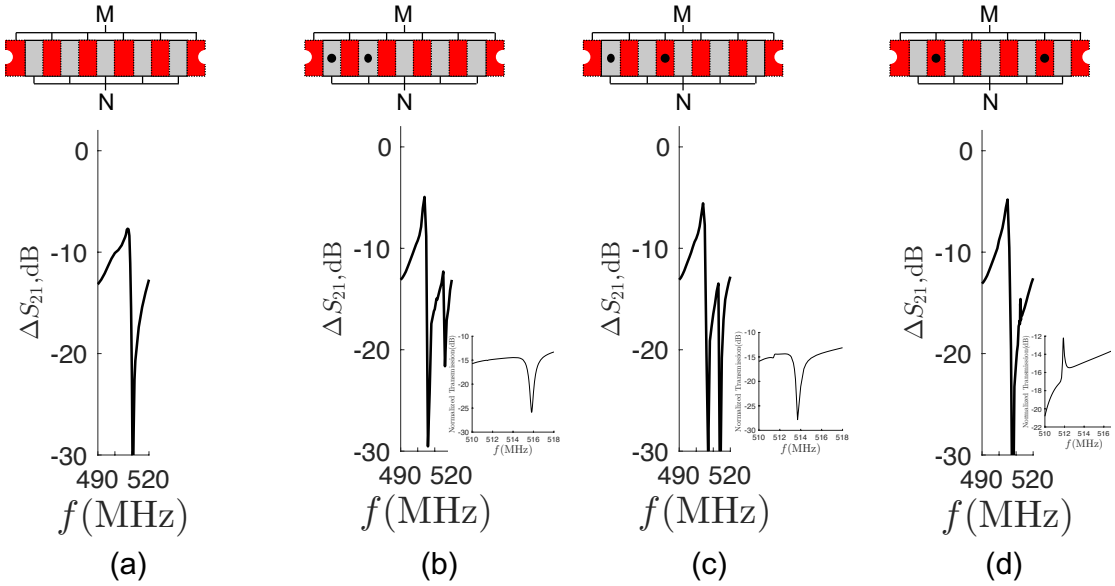

FIGURE 5.21 – (a)Transmission curve of Love waves for the cavity mode at 507.5 MHz. (b)(c)(d) Transmission spectra when two pillar is at (b) NN, (c) NM, (d) MM, respectively. Pillar position is presented by the cavity division diagram on top of the transmission curves. r_h=0.2a, r_p=0.18a_p, a = 4μm, a_p = 2μm

First, we consider two pillars at different positions, where three kinds of combinations are possible : NN, NM and MM. Since one pillar in all the N(or M) position gives almost the same transmission results, we present only one result for each combination. Fig 5.21 shows the transmission spectra of the three cases. It can be seen that two pillars

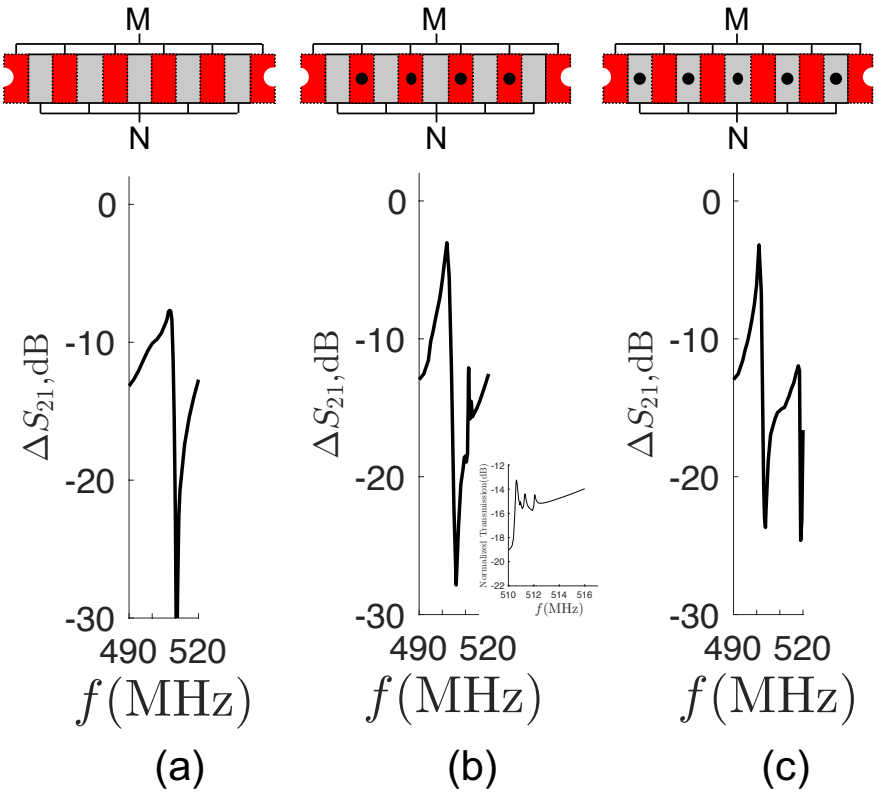

FIGURE 5.22 – Transmission spectra when all the (b) M (c) N positions hold a pillar. Figure (a) serves as reference.

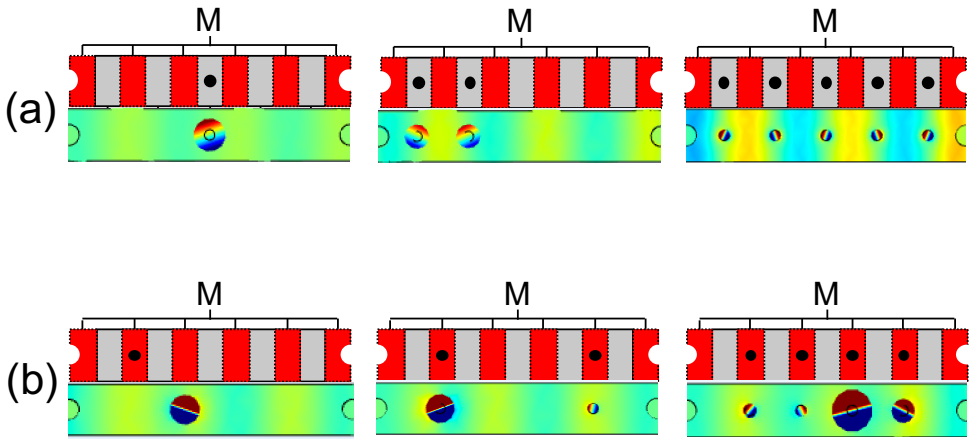

FIGURE 5.23 – u_y for the pillar induced dips or peaks when pillars are at (a)N or (b)M.

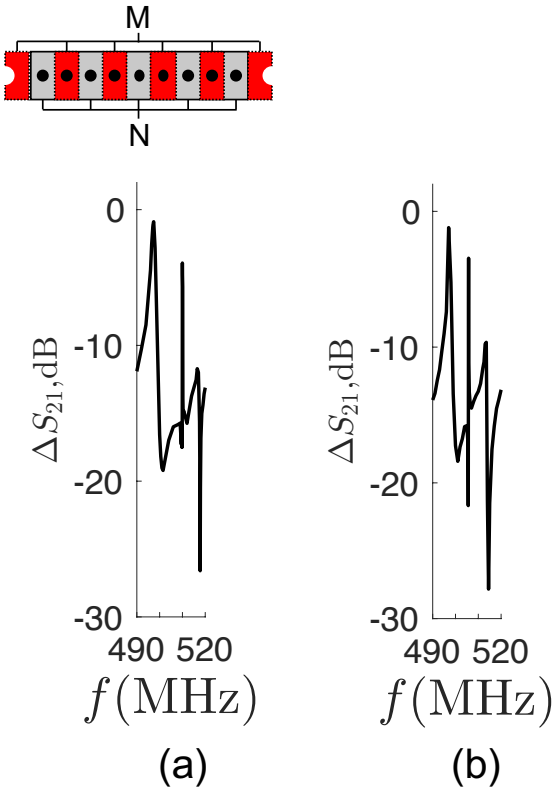

FIGURE 5.24 – Transmission spectra of Love waves when all N and M are occupied by a pillars. The pillar radius is (a) $0.18a_p$ and (b)$0.19a_p$. $a_p = 2\mu$m

at N position still arouse a dip beside the cavity mode. This dip is shorter than that for a single pillar at N position, since the pillar-induced dip becomes shorter with the increase of pillar's number, see 4.1. Two pillars at M position induce a small peak that is closer to the cavity mode, while the combination of N and M position gives rise to a dip with a small disturbance beside the dip. The resonant frequency of the dip for the case NM is between that for the cases NN and MM, like the way of a single pillar in the center of N and M position. Additionally, the difference between the cavity mode frequency and the pillar resonant frequencies have been enlarged, the cavity mode is displaced to a lower frequency, and the transmission of the two peaks (of cavity mode and pillar mode) have been slightly improved, compared with the cases for a single pillar.

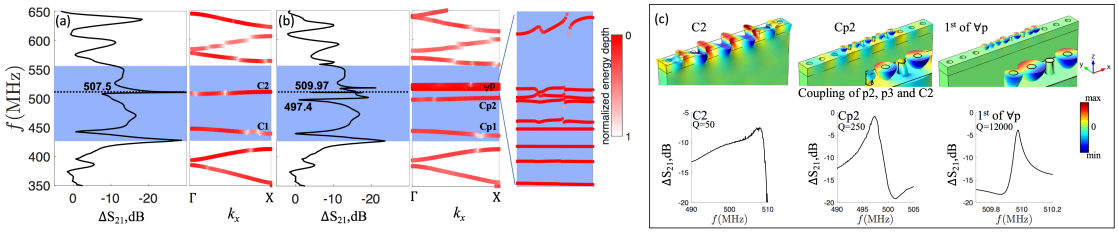

FIGURE 5.25 – Normalized transmission spectra and band structures of SH surface modes for the cavity-containing h-PnCs (a)without and (b)with pillars. Blue zones are the band-gap region of the perfect holey PnC. Dotted line is the pillar torsional mode frequency f_{p2} ; (c) u_y and enlarged transmission peaks of C2, Cp2 and 1^{st} of ∀p. Insets : zoomed pillars.

Since the NM case gives a synthetic result of the case N and M, we can study separately the effect of the number of pillars placed at N or M position. Fig 5.22 shows the transmission curves calculated when all M/N positions hold a pillar. It is found that, compared with the above results, the pillar induced peak (in Fig 5.22(b)) is enhanced by increasing the pillar number. The cavity mode transmission has been ameliorated in both cases and the frequency difference between the two resonances has been enlarged. The frequency of cavity mode has a tendency to decrease and the distance between the cavity mode and the peak/dip becomes larger. One should notice that the antiresonance of the cavity mode becomes less deeper when we increase the pillar number, and the Fano resonance line-shape (asymmetric profile) tends to become a Lorentzian resonance (symmetric profile).

Fig 5.23 gives an overview of u_y for the pillar modes when pillars are at N or M positions. One can see that when pillars are at N positions, they are coupled to the cavity mode and the amplitude in the guiding layer corresponds well to the bare cavity mode. There are 2.5 wave periods in the cavity which indicating a wavelength $\lambda = 2a$ However, when pillars are at M positions, as we have stated above, the pillars generate a wave which interfere with the waves in background, so as to change the amplitude in the guiding layer. It is interesting that when we change the number of pillars at M position, there are always 6 zero displacement along the propagating direction in

the cavity (agaist 5 for the position N cases), as if the wavelength has been changed. Additionally, when pilllars are at N position, the amplitude in pillars are uniform, while when pillars are at M position, the maximum amplitude is presented in a single pillar.

It is worth noting that when we combine the above two cases, that is, N and M positions are all occupied by a pillar, this structure gives rise to a synthetic performance of pillar induced peak and dip. Fig 5.24 shows the examples for $r_p = 0.18a_p$ and $r_p = 0.19a_p$. It is found that the pillar induced peak is significantly enhanced for both the transmission and confinement. This can be explicated by a stronger coupling effect between the adjacent pillars. Moreover, a smaller periodicity ensures that the Bragg band gap of the p-PnC does not appear in the frequency range of our interest.

Between the two transmission profiles, small frequency shifts are found for the pillar induced peaks and dips because of the different pillar radius. However, the transmission line-shapes are almost the same despite the different results for the single pillar cases (in Fig 5.18 and 5.19). Additionally, the transmission peak of the cavity mode has also been increased by increasing the pillar number.

The Love waves normalized transmission spectra and band structures around the whole band-gap region for the cavity without and with pillars are shown in Fig 5.25(a) and (b), respectively, in the case $r_p = 0.18a_p$. The fundamental cavity modes C1 and C2 are coupled to the pillars and become two new modes Cp1 and Cp2, while multiple pillar modes $\forall p$ appear around the pillar intrinsic torsional mode frequency (f_{p2}). It can be seen that due to the inserted pillars mass, Cp1 at 433.4 MHz has a slight down frequency shift compared with C1, whereas Cp2 has shifted down to 490.5 MHz as has been noticed above. The frequency shift of Cp2 results from both the mass loading and the peak splitting effect that is attributed to a degeneracy of the cavity mode [171], that is, a coupling of cavity mode with pillar mode as shown in Fig 5.17.

Compared with mode Cp1, the transmission peak of Cp2 is significantly sharper than that of the mode C2, as a result of the matched frequencies between f_{C2} and f_{p2}.

The pillar modes $\forall p$ are different combinations of pillars vibrating in torsional mode, with the maximum displacements existing in different pillars. The number of pillar modes equals to the number of pillars, i.e., 9 pillar modes with adjacent frequencies around f_{p2}, which can be adjusted by the pillar's parameters. The dispersion curves of $\forall p$ are zoomed on the right of Fig 5.25(b). The first pillar mode gives rise to the sharp transmission peak at 507.3MHz. The last mode, with a less smoothing and homogeneous dispersion curve, only arouses a small resonance at 517.5 MHz. Other pillar modes disappear in the transmission spectrum because they are not well coupled to the SH waves, as shown in the inset of the transmission curve. This transmission spectrum results from a coupling between the p-PnC and the bare cavity-containing h-PnC.

The differences in sharpness of the transmission peaks for modes C2, Cp2 and the 1^{st} of $\forall p$ could be explained after observing their displacement fields shown in Fig 5.25(c). When Love waves propagate through the cavity, the displacement of C2 is concentrated in the center of the model and is confined in the silica guiding film. For the mode Cp2 as we investigated above, the maximum displacement amplitude is in the pillars, leading to an energy more confined to the surface (a smaller NED). This is proved by the dispersion curve of Cp2 whose red color is more intense than that of C2. Note that the pillars at position N and M is alternating along the propagating direction. The torsional mode can be excited for the pillars at N, while the pillars at M are moved according to the layer's displacement. As for the 1^{st} collective pillar mode of $\forall p$, only tiny displacement exists in the guiding layer, leading to the most confined energy and the sharpest transmission peak. The magnification of these three peaks is shown aside. The quality factor (Q) of the mode Cp2 is 5 times greater than that of the mode C2. The Q of the sharpest peak is 240 times greater than that of C2, with a transmission peak at almost the same frequency. This means that the efficiency of the cavity could be significantly enhanced by introducing the optimally sized pillars.

5.6 Conclusion

In this chapter, cavity modes in the phononic band gap for Love waves are first demonstrated by removing lines of holes from the guiding film of the holey PnC. The transmission peaks of cavity modes in the original band gap of the perfect holey PnC is attributed to the appearance of new flat modes in the band structure. The transmission spectra are proved to be consistent with the band structure predictions. The holes radius has a strong effect on the waves confinement and the transmission performance. The resonant frequencies of cavity modes are related to the cavity width. The symmetrical and asymmetrical cavity modes appear alternatively with the increase of cavity width. The quality factor can be enhanced by increasing the crystal size, the transmission, however, will be decreased due to an energy loss. A well confined and flat cavity mode, as well as a properly chosen PnC size, is essential for obtaining sharp transmission peaks. Cavity modes have also been demonstrated in pillared and mixed PnCs.

An optimally sized cavity is then chosen to match the pillar torsional mode frequency. Pillar-containing cavity for Love waves is first demonstrated by introducing the pillars into the cavity. By dividing the cavity into two parts (N/M) according to the displacement amplitude, we systematically studied the coupling effect between the pillar and the cavity mode. The pillar at position N can be excited and is coupled to the cavity mode, leading the cavity mode peak to split into two peaks. Whereas the pillar at M position is not coupled to the cavity mode but can still give rise to a peak by emitting an additional wave. Peak splitting effect is explained as an avoided crossing when the cavity mode is coupled to the pillar intrinsic mode. The cavity mode efficiency can be improved when it is coupled to the pillar mode. The pillar's resonant performance as well as the cavity efficiency can be enhanced by increasing the pillar number. The sharpest transmission peak created at the original cavity mode frequency has a 240 times greater quality factor. Compared with the holey PnC based bare cavity, the coupled cavity provides a method

to significantly ameliorate the Q factor while maintaining a high transmission level. This study could be used for potential applications of Love wave-based PnC devices such as meta-materials and bio-sensors.

Conclusion

Phononic crystals are objects that appeared in the 1990s and offer unlimited means of controlling acoustic/elastic waves. Among the models that appeared in the literature, their sturctures and materials, interactions with different waves, their performances for different waves interacting with defects states and the interaction between different resonators were discussed. In this thesis, the investigation of micro and nano structured materials for acoustic band gaps engineering in electro-acoustic devices was presented, especially for the study of two-dimensional holey and/or pillared phononic crystals interacting with Love waves and the interaction between different resonators.

The theoretical background introduced in Chapter 2 is the fundamental knowledge accumulation for this work. We systematically talked about different surface acoustic waves propagating in piezoelectric materials by considering the elasticity, the lattice and band theories, as well as two mechanisms (Bragg scattering and local resonance) of phononic band gaps.

In Chapter 3, the theoretical modeling of the band structures was computed on COMSOL Multiphysics, a finite element simulation software. Firstly We studied the effect of the different square lattices (holey or/and Ni pillared) built on a guiding layer of SiO_2 deposited on the 90ST quartz substrate. Love waves are selected from bulk waves. The different polarizations of the modes within different lattices have been observed and explained. The effects of geometrical and elastic parameters on the band structures were proposed and analyzed. Then, a SAW device module is built to calculate the Love

wave transmissions through the different PnCs. The effect of the band gaps gave rise to the attenuation intervals in the transmission spectra. The transmissions are compatible with the band structures of the different PnCs. By combining and adjusting the holey and pillared PnC, we demonstrated that the mixed PnC has a capacity to enlarge the band gap or to generate isolated mode in the band gap.

In Chapter 4, we investigate the interaction of Love waves with one- or two-line pillared meta-surface. The pillar lines are perpendicular to the waves propagation direction. Acoustic analogue of Autler-Townes Splitting (ATS) and cavity modes are first demonstrated in two lines of identical pillars by varying the distance between the pillar lines. ATS appears when the distance is smaller than the half wavelength and a strong coupling is aroused between the pillar lines. Fabry-Perot resonance exists at the positions where the distance between the pillar lines is a multiple of half wavelength. The proximity of Fabry-Perot resonance with pillar intrinsic mode gives rise to the cavity modes. Then, the radius of one line of pillars is modified to detune the pillar resonant frequencies. In the pillar coupling region, the coupling effect decreases with the increase of radius mismatch. When the distance between the pillar lines is a multiple of half wavelength, Fabry-Perot resonance along with the two different pillar resonances give rise to the acoustic analogue of Electromagnetically Induced Transparency (AIT). ATS and AIT formula models are used to fit the transmission spectra, showing good agreements with numerical results. The quality of the fit models is quantitatively evaluated by resorting to the Akaike information criterion (AIC). ATS and AIT are theoretically and analytically discriminated. Fano resonance is demonstrated for two dissimilar pillars that alternate in a single line. This resonance can be increasingly confined by reducing the geometrical mismatch between the two pillars or by reducing the periodicity along the direction perpendicular to the propagation direction.

In Chapter 5, the defect or cavity modes for Love waves are demonstrated for the first time by removing lines of holes perpendicularly to the direction of propagation, for

the holey PnC. The transmission peaks of cavity modes in the band gap are attributed to the appearance of new flat modes in the band structure. The transmission spectra are in agreement with the band structure predictions. A smaller hole radius promotes the confinement of the cavity modes. Cavity resonant frequencies are related to the cavity width. The confinement of the dispersion curves plays a role in the behavior of the resonances. The crystal size on each side of the cavity has an effect on the quality factor. Cavity modes are also demonstrated in the other 2 PnCs (pillared & mixed). After the studies of the cavity and the pure pillars, pillar-containing cavity is first demonstrated by introducing the pillars into the bare cavity. The pillar torsional mode is capable of being coupled to the cavity mode when these two modes fall at close frequencies. The position and number of pillars in the cavity can affect the frequency, transmission, and quality factor of the coupled cavity modes as well as the pillar mode. Pillars at the max / min amplitude positions (anti-nodes) would give rise to a sharp transmission peak. The displacement field for this peak is different from that of the cavity modes that sandwich it, because of the waves generated by the pillars. A full coupling of the cavity mode to the pillar mode is then created with significant improvement on the cavity efficiency.

Publications during the thesis

International peer-reviewed journal articles

[1] Yuxin Liu, Abdelkrim Talbi, Philippe Pernod and Olivier Bou Matar, Highly Confined Love Waves Modes by Defect States in a Holey SiO_2/Quartz Phononic Crystal, *Journal of Applied Physics*, **124**, 145102, 2018.

[2] Yuxin Liu, Abdelkrim Talbi, Bahram Djafari-Rouhani, El Houssaine El Boudouti, Lucie Drbohlavova, Vincent Mortet, Olivier Bou Matar and Philippe Pernod, Interaction of Love Waves with Coupled Cavity Modes in a 2D Holey Phononic Crystal, *Physics Letters A*, **383**, 1502-1505, 2019.

[3] Yuxin Liu, Abdelkrim Talbi, El Houssaine El Boudouti, Olivier Bou Matar and Philippe Pernod, Bahram Djafari-Rouhani, Autler-Townes Splitting and Acoustically Induced Transparency based on Love Waves Interacting with Pillared Meta-surface, *Physical Review Applied*, **11**, 064066, 2019.

[4] Lucie Drbohlavova, Ladislav Fekete, Viktor Bovtun, Martin Kempa, Andrew Taylor, Yuxin Liu, Olivier Bou Matar, Abdelkrim Talbi, Vincent Mortet, Love-Wave Devices with Continuous and Discrete Nanocrystalline Diamond Coating for Biosensing Applications, *Sensors & Actuators : A. Physical*, **298**, 111584, 2019.

Articles of international conferences with reviewing committee and published proceedings

[5] Yu-Xin Liu, Abdelkrim Talbi, Philippe Pernod and Olivier Bou Matar, Highly Confined Love Waves Modes by Defects States in a Phononic Crystal Based on Holey-SiO_2/ST-Cut Quartz Structure, *Proceedings*, 2, 729, 2018.

[6] Yuxin Liu, Abdelkrim Talbi, El Houssaine El Boudouti, Olivier Bou Matar, Philippe Pernod, Bahram Djafari-Rouhani, Hybridization of Love surface acoustic waves in SiO_2/ST-Quartz structure with resonant pillars grafted on the meta-surface. accepted by *2019 International Congress on Ultrasonics*.

Bibliographie

[1] A. Khelif, A. Choujaa, B. Djafari-Rouhani, M. Wilm, S. Ballandras et V. Laude, « Trapping and guiding of acoustic waves by defect modes in a full-band-gap ultrasonic crystal », *Physical Review B*, t. 68, n° 21, déc. 2003.

[2] A. Khelif, A. Choujaa, S. Benchabane, B. Djafari-Rouhani et V. Laude, « Experimental study of guiding and filtering of acoustic waves in a two dimensional ultrasonic crystal », *Zeitschrift für Kristallographie - Crystalline Materials*, t. 220, n° 9-10, p. 836–840, 2005.

[3] T.-C. Wu, T.-T. Wu et J.-C. Hsu, « Waveguiding and frequency selection of Lamb waves in a plate with a periodic stubbed surface », *Physical Review B*, t. 79, n° 10, mar. 2009.

[4] R. H. Olsson, S. X. Griego, I. El-Kady, M. Su, Y. Soliman, D. Goettler et Z. Leseman, « Ultra high frequency (UHF) phononic crystal devices operating in mobile communication bands », in *IEEE International Ultrasonics Symposium*, IEEE, 2009, p. 1150–1153.

[5] Y. Pennec, J. O. Vasseur, B. Djafari-Rouhani, L. Dobrzyński et P. A. Deymier, « Two-dimensional phononic crystals : Examples and applications », *Surface Science Reports*, t. 65, n° 8, p. 229–291, août 2010.

[6] B. Liang, X. S. Guo, J. Tu, D. Zhang et J. C. Cheng, « An acoustic rectifier », *Nature Materials*, t. 9, n° 12, p. 989–992, déc. 2010.

[7] D. Feng, W. Jiang, D. Xu, B. Xiong et Y. Wang, « Micro-silicon phononic crystal with locally resonant theory », *Applied Physics Letters*, t. 110, n° 17, p. 171 902, avr. 2017.

[8] F. Meseguer, M. Holgado, D. Caballero, N. Benaches, J. Sánchez-Dehesa, C. López et J. Llinares, « Rayleigh-wave attenuation by a semi-infinite two-dimensional elastic-band-gap crystal », *Physical Review B*, t. 59, n° 19, p. 12 169–12 172, mai 1999.

[9] T. T. Wu, W. S. Wang et J. H. Sun, « A layered SAW device using phononic-crystal reflective gratings », in *IEEE International Ultrasonics Symposium*, nov. 2008, p. 709–712.

[10] R. H. Olsson III et I. El-Kady, « Microfabricated phononic crystal devices and applications », *Measurement Science and Technology*, t. 20, n° 1, p. 012 002, jan. 2009.

[11] M. Ziaei-Moayyed, M. F. Su, C. Reinke, I. F. El-Kady et R. H. Olsson, « Silicon carbide phononic crystal cavities for micromechanical resonators », in *IEEE 24th International Conference*, IEEE, 2011, p. 1377–1381.

[12] T.-W. Liu, Y.-C. Tsai, Y.-C. Lin, T. Ono, S. Tanaka et T.-T. Wu, « Design and fabrication of a phononic-crystal-based Love wave resonator in GHz range », *AIP Advances*, t. 4, n° 12, p. 124 201, déc. 2014.

[13] L. Binci, C. Tu, H. Zhu et J. E.-Y. Lee, « Planar ring-shaped phononic crystal anchoring boundaries for enhancing the quality factor of Lamb mode resonators », *Applied Physics Letters*, t. 109, n° 20, p. 203 501, nov. 2016.

[14] A. Talbi, F. Sarry, M. Elhakiki, L. L. Brizoual, O. Elmazria, P. Nicolay et P. Alnot, « ZnO/quartz structure potentiality for surface acoustic wave pressure sensor », *Sensors and Actuators A : Physical*, t. 128, n° 1, p. 78–83, mar. 2006.

[15] R. Lucklum et J. Li, « Phononic crystals for liquid sensor applications », *Measurement Science and Technology*, t. 20, n° 12, p. 124 014, déc. 2009.

[16] M. Ke, M. Zubtsov et R. Lucklum, « Sub-wavelength phononic crystal liquid sensor », *Journal of Applied Physics*, t. 110, n° 2, p. 026 101, juil. 2011.

[17] M. Zubtsov, R. Lucklum, M. Ke, A. Oseev, R. Grundmann, B. Henning et U. Hempel, « 2D phononic crystal sensor with normal incidence of sound », *Sensors and Actuators A : Physical*, t. 186, p. 118–124, oct. 2012.

[18] A. Salman, O. A. Kaya, A. Cicek et B. Ulug, « Low-concentration liquid sensing by an acoustic Mach–Zehnder interferometer in a two-dimensional phononic crystal », *Journal of Physics D : Applied Physics*, t. 48, n° 25, p. 255 301, juin 2015.

[19] Z. Xu et Y. J. Yuan, « Implementation of guiding layers of surface acoustic wave devices : A review », *Biosensors and Bioelectronics*, t. 99, p. 500–512, jan. 2018.

[20] B. Kim, J. Nguyen, C. Reinke, E. Shaner, C. T. Harris, I. El-Kady et R. H. Olsson III, « Thermal conductivity manipulation in lithographically patterned single crystal silicon phononic crystal structures », in *IEEE International Ultrasonics Symposium*, oct. 2011, p. 1308–1311.

[21] J.-K. Yu, S. Mitrovic, D. Tham, J. Varghese et J. R. Heath, « Reduction of thermal conductivity in phononic nanomesh structures », *Nature Nanotechnology*, t. 5, n° 10, p. 718–721, oct. 2010.

[22] L. Yang, N. Yang et B. Li, « Extreme low thermal conductivity in nanoscale 3D Si phononic crystal with spherical pores », *Nano Letters*, t. 14, n° 4, p. 1734–1738, avr. 2014.

[23] N. Zen, T. A. Puurtinen, T. J. Isotalo, S. Chaudhuri et I. J. Maasilta, « Engineering thermal conductance using a two-dimensional phononic crystal », *Nature Communications*, t. 5, mar. 2014.

[24] X. Zhang et Z. Liu, « Negative refraction of acoustic waves in two-dimensional phononic crystals », *Applied Physics Letters*, t. 85, n° 2, p. 341–343, juil. 2004.

[25] D. M. Profunser, E. Muramoto, O. Matsuda, O. B. Wright et U. Lang, « Dynamic visualization of surface acoustic waves on a two-dimensional phononic crystal », *Physical Review B*, t. 80, n° 1, juil. 2009.

[26] J. Zhu, J. Christensen, J. Jung, L. Martin-Moreno, X. Yin, L. Fok, X. Zhang et F. J. Garcia-Vidal, « A holey-structured metamaterial for acoustic deep-subwavelength imaging », *Nature Physics*, t. 7, n° 1, p. 52–55, jan. 2011.

[27] S. Narayana et Y. Sato, « Heat flux manipulation with engineered thermal materials », *Physical Review Letters*, t. 108, n° 21, mai 2012.

[28] J. Zhao, B. Bonello, R. Marchal et O. Boyko, « Beam path and focusing of flexural Lamb waves within phononic crystal-based acoustic lenses », *New Journal of Physics*, t. 16, n° 6, p. 063 031, juin 2014.

[29] J. Li, F. Wu, H. Zhong, Y. Yao et X. Zhang, « Acoustic beam splitting in two-dimensional phononic crystals using self-collimation effect », *Journal of Applied Physics*, t. 118, n° 14, p. 144 903, oct. 2015.

[30] C.-N. Tsai et L.-W. Chen, « The manipulation of self-collimated beam in phononic crystals composed of orientated rectangular inclusions », *Applied Physics A*, t. 122, n° 7, juil. 2016.

[31] J. H. Page, « Focusing of ultrasonic waves by negative refraction in phononic crystals », *AIP Advances*, t. 6, n° 12, p. 121 606, déc. 2016.

[32] Y. Guo, D. Brick, M. Grossmann, M. Hettich et T. Dekorsy, « Acoustic beam splitting at low GHz frequencies in a defect-free phononic crystal », *Applied Physics Letters*, t. 110, n° 3, p. 031 904, jan. 2017.

[33] S. Degraeve, C. Granger, B. Dubus, J. O. Vasseur, M. P. Thi et A.-C. Hladky-Hennion, « Bragg band gaps tunability in an homogeneous piezoelectric rod with periodic electrical boundary conditions », *Journal of Applied Physics*, t. 115, p. 194 508, 2014.

[34] Y.-F. Wang, A. Maznev et V. Laude, « Formation of Bragg Band Gaps in Anisotropic Phononic Crystals Analyzed With the Empty Lattice Model », *Crystals*, t. 6, n° 5, p. 52, 2016.

[35] Z. Liu, X. Zhang, Y. Mao, Y. Y. Zhu, Z. Yang, C. T. Chan et P. Sheng, « Locally resonant sonic materials », *Science*, t. 289, n° 5485, p. 1734–1736, sept. 2000.

[36] G. Wang, X. Wen, J. Wen, L. Shao et Y. Liu, « Two-Dimensional Locally Resonant Phononic Crystals with Binary Structures », *Physical Review Letters*, t. 93, p. 154 302, 2004.

[37] J.-C. Hsu et T.-T. Wu, « Lamb waves in binary locally resonant phononic plates with two-dimensional lattices », *Applied Physics Letters*, t. 90, p. 201 904, 2007.

[38] M. Oudich, M. B. Assouar et Z. Hou, « Propagation of acoustic waves and waveguiding in a two-dimensional locally resonant phononic crystal plate », *Applied Physics Letters*, t. 97, p. 193 503, 2010.

[39] M. Oudich, Y. Li, B. M. Assouar et Z. Hou, « A sonic band gap based on the locally resonant phononic plates with stubs », *New Journal of Physics*, t. 12, n° 8, p. 083 049, août 2010.

[40] M. Oudich, M. Senesi, M. B. Assouar, M. Ruzenne, J.-H. Sun, B. Vincent, Z. Hou et T.-T. Wu, « Experimental evidence of locally resonant sonic band gap in two-dimensional phononic stubbed plates », *Physical Review B*, t. 84, p. 165 136, 2011.

[41] M. B. Assouar et M. Oudich, « Dispersion curves of surface acoustic waves in a two-dimensional phononic crystal », *Applied Physics Letters*, t. 99, p. 123 505, 2011.

[42] ——, « Enlargement of a locally resonant sonic band gap by using double-sides stubbed phononic plates », *Applied Physics Letters*, t. 100, p. 123 506, 2012.

[43] Y. Chen et L. Wang, « Periodic co-continuous acoustic metamaterials with overlapping locally resonant and Bragg band gaps », *Applied Physics Letters*, t. 105, p. 191 907, 2014.

[44] A. O. Krushynska, M. Miniaci, F. Bosia et N. M. Pugno, « Coupling local resonance with Bragg band gaps in single-phase mechanical metamaterials », *Extreme Mechanics Letters*, t. 12, p. 30–36, 2017.

[45] M. B. Assouar, J.-H. Sun, F.-S. Lin et J.-C. Hsu, « Hybrid phononic crystal plates for lowering and widening acoustic band gaps », *Ultrasonics*, t. 54, p. 2159–2164, 2014.

[46] E. Coffy, S. Euphrasie, M. Addouche, P. Vairac et A. Khelif, « Evidence of a broadband gap in a phononic crystal strip », *Ultrasonics*, t. 78, p. 51–56, juil. 2017.

[47] E. Coffy, T. Lavergne, M. Addouche, S. Euphrasie, P. Vairac et A. Khelif, « Ultra-wide acoustic band gaps in pillar-based phononic crystal strips », *Journal of Applied Physics*, t. 118, p. 214 902, 2015.

[48] D. Midtvedt, A. Isacsson et A. Croy, « Nonlinear phononics using atomically thin membranes », *Nature Communications*, t. 5, p. 4838, 2014.

[49] B. Graczykowski, M. Sledzinska, F. Alzina, J. Gomis-Bresco, J. S. Reparaz, M. R. Wagner et C. M. Sotomayor Torres, « Phonon dispersion in hypersonic two-dimensional phononic crystal membranes », *Physical Review B*, t. 91, n° 7, fév. 2015.

[50] M. M. Sigalas et E. N. Economou, « Elastic and acoustic wave band structure », *Journal of sound and vibration*, t. 158, n° 2, p. 377–382, 1992.

[51] J. P. Dowling, « Sonic band structure in fluids with periodic density variations », *The Journal of the Acoustical Society of America*, t. 91, n° 5, p. 2539–2543, 1992.

[52] M. S. Kushwaha, P. Halevi, L. Dobrzynski et B. Djafari Rouhani, « Acoustic band structure of periodic elastic composites », *Physical Review Letters*, t. 71, n° 13, p. 2022–2025, sept. 1993.

[53] S. Benchabane, O. Gaiffe, G. Ulliac, R. Salut, Y. Achaoui et V. Laude, « Observation of surface-guided waves in holey hypersonic phononic crystal », *Applied Physics Letters*, t. 98, n° 17, p. 171 908, avr. 2011.

[54] S. Benchabane, O. Gaiffe, R. Salut, G. Ulliac, V. Laude et K. Kokkonen, « Guidance of surface waves in a micron-scale phononic crystal line-defect waveguide », *Applied Physics Letters*, t. 106, n° 8, p. 081 903, fév. 2015.

[55] S. Mohammadi, A. A. Eftekhar, W. D. Hunt et A. Adibi, « High-Q micromechanical resonators in a two-dimensional phononic crystal slab », *Applied Physics Letters*, t. 94, n° 5, p. 051 906, fév. 2009.

[56] C. Cassella, J. Segovia-Fernandez, G. Piazza, M. Cremonesi et A. Frangi, « Reduction of anchor losses by etched slots in aluminum nitride contour mode resonators », eng, in *2013 Joint European Frequency and Time Forum International Frequency Control Symposium (EFTF/IFC)*, IEEE, 2013, p. 926–929.

[57] C.-M. Lin, Y.-J. Lai, J.-C. Hsu, Y.-Y. Chen, D. G. Senesky et A. P. Pisano, « High- Q aluminum nitride Lamb wave resonators with biconvex edges », *Applied Physics Letters*, t. 99, n° 14, 2011.

[58] C.-M. Lin, J.-C. Hsu, D. G. Senesky et A. P. Pisano, « Anchor loss reduction in ALN Lamb wave resonators using phononic crystal strip tethers », *2014 IEEE International Frequency Control Symposium*, p. 1–5, mai 2014.

[59] G. Floquet, « Sur les équations différentielles linéaires à coefficients périodiques », *Annales Scientifiques de l'Ecole Normale Supérieure*, t. 12, p. 47–88, 1883.

[60] L. Rayleigh, « On the maintenance of vibrations by forces of double frequency, and on the propagation of waves through a medium endowed with a periodic structure », *Philosophical Magazine Series 5*, t. 24, n° 147, p. 145–159, août 1887.

[61] L. Brillouin, *Wave propagation in periodic structures*, 2nd edition. New Yorkl : Dover Publications, 1953.

[62] W. E. Newell, « Face-mounted piezoelectric resonators », *Proceedings of the IEEE*, t. 53, n° 6, p. 575–581, 1965.

[63] E. Yablonovitch, « Inhibited spontaneous emission in solid-state physics and electronics », *Physical review letters*, t. 58, n° 20, p. 2059, 1987.

[64] S. John, « Strong localization of photons in certain disordered dielectric superlattices », *Physical review letters*, t. 58, n° 23, p. 2486, 1987.

[65] M. S. Kushwaha et P. Halevi, « Band-gap engineering in periodic elastic composites », *Applied Physics Letters*, t. 64, n° 9, p. 1085–1087, fév. 1994.

[66] R. Martínez-Sala, J. Sancho, J. V. Sánchez, V. Gómez, J. Llinares et F. Meseguer, « Sound attenuation by sculpture », *Nature*, t. 378, n° 6554, p. 241–241, nov. 1995.

[67] J. O. Vasseur, P. A. Deymier, G. Frantziskonis, G. Hong, B. Djafari-Rouhani et L. Dobrzynski, « Experimental evidence for the existence of absolute acoustic band gaps in two-dimensional periodic composite media », *Journal of Physics : Condensed Matter*, t. 10, n° 27, p. 6051, 1998.

[68] J. V. Sánchez-Pérez, D. Caballero, R. Martinez-Sala, C. Rubio, J. Sánchez-Dehesa, F. Meseguer, J. Llinares et F. Gálvez, « Sound attenuation by a two-dimensional array of rigid cylinders », *Physical Review Letters*, t. 80, n° 24, p. 5325, 1998.

[69] R. Sprik et G. H. Wegdam, « Acoustic band gaps in composites of solids and viscous liquids », *Solid state communications*, t. 106, n° 2, p. 77–81, 1998.

[70] J. O. Vasseur, P. A. Deymier, B. Chenni, B. Djafari-Rouhani, L. Dobrzynski et D. Prevost, « Experimental and theoretical evidence for the existence of absolute acoustic band gaps in two-dimensional solid phononic crystals », *Physical Review Letters*, t. 86, n° 14, p. 3012–3015, avr. 2001.

[71] W. M. Robertson et J. F. Rudy III, « Measurement of acoustic stop bands in two-dimensional periodic scattering arrays », *The Journal of the Acoustical Society of America*, t. 104, n° 2, p. 694–699, 1998.

[72] T. Miyashita, « Sonic crystals and sonic wave-guides », *Measurement Science and Technology*, t. 16, n° 5, R47–R63, mai 2005.

[73] F.-L. Hsiao, A. Khelif, H. Moubchir, A. Choujaa, C.-C. Chen et V. Laude, « Complete band gaps and deaf bands of triangular and honeycomb water-steel phononic crystals », *Journal of Applied Physics*, t. 101, n° 4, p. 044 903, fév. 2007.

[74] S. Yang, J. H. Page, Z. Liu, M. L. Cowan, C. T. Chan et P. Sheng, « Ultrasound tunneling through 3D phononic crystals », *Physical Review Letters*, t. 88, n° 10, fév. 2002.

[75] A. Khelif, P. A. Deymier, B. Djafari-Rouhani, J. O. Vasseur et L. Dobrzynski, « Two-dimensional phononic crystal with tunable narrow pass band : Application to a waveguide with selective frequency », *Journal of Applied Physics*, t. 94, n° 3, p. 1308–1311, août 2003.

[76] S. Benchabane, A. Khelif, A. Choujaa, B. Djafari-Rouhani et V. Laude, « Interaction of waveguide and localized modes in a phononic crystal », *Europhysics Letters*, t. 71, n° 4, p. 570, 2005.

[77] F. V. D. Biest, A. Sukhovich, A. Tourin, J. H. Page, B. A. v. Tiggelen, Z. Liu et M. Fink, « Resonant tunneling of acoustic waves through a double barrier consisting of two phononic crystals », *Europhysics Letters*, t. 71, n° 1, p. 63–69, juil. 2005.

[78] S. Yang, J. H. Page, Z. Liu, M. L. Cowan, C. T. Chan et P. Sheng, « Focusing of sound in a 3D phononic crystal », *Physical review letters*, t. 93, n° 2, p. 024 301, 2004.

[79] M. Ke, Z. Liu, C. Qiu, W. Wang, J. Shi, W. Wen et P. Sheng, « Negative-refraction imaging with two-dimensional phononic crystals », *Physical Review B*, t. 72, n° 6, août 2005.

[80] L. Dhar et J. A. Rogers, « High frequency one-dimensional phononic crystal characterized with a picosecond transient grating photoacoustic technique », *Applied Physics Letters*, t. 77, n° 9, p. 1402, 2000.

[81] T.-T. Wu, L.-C. Wu et Z.-G. Huang, « Frequency band-gap measurement of two-dimensional air/silicon phononic crystals using layered slanted finger interdigital transducers », *Journal of Applied Physics*, t. 97, n° 9, p. 094 916, mai 2005.

[82] W. Cheng, J. Wang, U. Jonas, G. Fytas et N. Stefanou, « Observation and tuning of hypersonic bandgaps in colloidal crystals », *Nature Materials*, t. 5, p. 830–836, 2006.

[83] T. Gorishnyy, C. K. Ullal, M. Maldovan, G. Fytas et E. L. Thomas, « Hypersonic phononic crystals », *Physical Review Letters*, t. 94, n° 11, mar. 2005.

[84] S. Mohammadi, A. A. Eftekhar, A. Khelif, W. D. Hunt et A. Adibi, « Evidence of large high frequency complete phononic band gaps in silicon phononic crystal plates », *Applied Physics Letters*, t. 92, n° 22, p. 221 905, juin 2008.

[85] P. E. Hopkins, C. M. Reinke, M. F. Su, R. H. Olsson, E. A. Shaner, Z. C. Leseman, J. R. Serrano, L. M. Phinney et I. El-Kady, « Reduction in the thermal conductivity of single crystalline silicon by phononic crystal patterning », *Nano Letters*, t. 11, n° 1, p. 107–112, jan. 2011.

[86] S. Mohammadi, A. A. Eftekhar, A. Khelif, W. D. Hunt et A. Adibi, « Evidence of the existence of complete phononic band gaps in phononic crystal plates », in *NSTI-Nanotech*, t. 3, 2008.

[87] S. Hemon, A. Akjouj, A. Soltani, Y. Pennec, Y. El Hassouani, A. Talbi, V. Mortet et B. Djafari-Rouhani, « Hypersonic band gap in an AlN-TiN bilayer phononic crystal slab », *Applied Physics Letters*, t. 104, n° 6, p. 063 101, fév. 2014.

[88] S. Benchabane, A. Khelif, J.-Y. Rauch, L. Robert et V. Laude, « Evidence for complete surface wave band gap in a piezoelectric phononic crystal », *Physical Review E*, t. 73, n° 6, juin 2006.

[89] K. Kokkonen, M. Kaivola, S. Benchabane, A. Khelif et V. Laude, « Scattering of surface acoustic waves by a phononic crystal revealed by heterodyne interferometry », *Applied Physics Letters*, t. 91, n° 8, p. 083 517, août 2007.

[90] S. Benchabane, L. Robert, G. Ulliac, S. Queste, A. Khelif et V. Laude, « Lithium niobate surface structuration for phononic crystal fabrication », in *IEEE International Ultrasonics Symposium*, IEEE, 2008, p. 2201–2204.

[91] Y. M. Soliman, M. F. Su, Z. C. Leseman, C. M. Reinke, I. El-Kady et R. H. Olsson, « Phononic crystals operating in the gigahertz range with extremely wide band gaps », *Applied Physics Letters*, t. 97, n° 19, p. 193 502, nov. 2010.

[92] I. El-Kady, R. H. Olsson et J. G. Fleming, « Phononic band-gap crystals for radio frequency communications », *Applied Physics Letters*, t. 92, n° 23, p. 233 504, juin 2008.

[93] R. H. Olsson, I. F. El-Kady, M. F. Su, M. R. Tuck et J. G. Fleming, « Microfabricated VHF acoustic crystals and waveguides », *Sensors and Actuators A : Physical*, t. 145-146, p. 87–93, juil. 2008.

[94] R. H. Olsson, J. G. Fleming, I. F. El-Kady, M. R. Tuck et F. B. McCormick, « Micromachined bulk wave acoustic bandgap devices », in *Transducers and Eurosensors*, IEEE, 2007, p. 317–321.

[95] Y. Soliman, D. Goettler, Z. Leseman, I. El-Kady et I. Olsson, « Effects of release hole size on microscale phononic crystals », in *SEM Annual Conference*, t. 4, Society for Experimental Mechanics, 2009, p. 2562–2570.

[96] M. F. Su, R. H. Olsson, Z. C. Leseman et I. El-Kady, « Realization of a phononic crystal operating at gigahertz frequencies », *Applied Physics Letters*, t. 96, n° 5, p. 053 111, fév. 2010.

[97] C. M. Reinke, M. F. Su, R. H. Olsson et I. El-Kady, « Realization of optimal bandgaps in solid-solid, solid-air, and hybrid solid-air-solid phononic crystal slabs », *Applied Physics Letters*, t. 98, n° 6, p. 061 912, fév. 2011.

[98] B. Wu, A. Kumar et S. Pamarthy, « High aspect ratio silicon etch : A review », *Journal of Applied Physics*, t. 108, n° 5, p. 051 101, sept. 2010.

[99] Y. Tanaka et S.-i. Tamura, « Surface acoustic waves in two-dimensional periodic elastic structures », *Physical Review B*, t. 58, n° 12, p. 7958, 1998.

[100] B. Manzanares-Martínez et F. Ramos-Mendieta, « Surface elastic waves in solid composites of two-dimensional periodicity », *Physical Review B*, t. 68, n° 13, oct. 2003.

[101] X. Zhang, T. Jackson, E. Lafond, P. Deymier et J. Vasseur, « Evidence of surface acoustic wave band gaps in the phononic crystals created on thin plates », *Applied Physics Letters*, t. 88, n° 4, p. 041 911, jan. 2006.

[102] V. Laude, M. Wilm, S. Benchabane et A. Khelif, « Full band gap for surface acoustic waves in a piezoelectric phononic crystal », *Physical Review E*, t. 71, n° 3, mar. 2005.

[103] Y. Achaoui, A. Khelif, S. Benchabane, L. Robert et V. Laude, « Experimental observation of locally-resonant and Bragg band gaps for surface guided waves in a phononic crystal of pillars », *Physical Review B*, t. 83, n° 10, mar. 2011.

[104] Y. Achaoui, V. Laude, S. Benchabane et A. Khelif, « Local resonances in phononic crystals and in random arrangements of pillars on a surface », *Journal of Applied Physics*, t. 114, n° 10, p. 104 503, sept. 2013.

[105] A. Khelif, Y. Achaoui et B. Aoubiza, « Locally resonant structures for low frequency surface acoustic band gap applications », in *Acoustic Metamaterials*, t. 166, Dordrecht : Springer Netherlands, 2013, p. 43–59.

[106] S. Yankin, A. Talbi, Y. Du, J.-C. Gerbedoen, V. Preobrazhensky, P. Pernod et O. Bou Matar, « Finite element analysis and experimental study of surface acoustic wave propagation through two-dimensional pillar-based surface phononic crystal », *Journal of Applied Physics*, t. 115, n° 24, p. 244 508, juin 2014.

[107] A. Khelif, Y. Achaoui et B. Aoubiza, « Surface acoustic waves in pillars-based two-dimensional phononic structures with different lattice symmetries », *Journal of Applied Physics*, t. 112, n° 3, p. 033 511, août 2012.

[108] R. Pourabolghasem, A. Khelif, S. Mohammadi, A. A. Eftekhar et A. Adibi, « Physics of band-gap formation and its evolution in the pillar-based phononic crystal structures », *Journal of Applied Physics*, t. 116, n° 1, p. 013 514, juil. 2014.

[109] R. Pourabolghasem, S. Mohammadi, A. A. Eftekhar, A. Khelif et A. Adibi, « Experimental evidence of high-frequency complete elastic bandgap in pillar-based phononic slabs », *Applied Physics Letters*, t. 105, n° 23, p. 231 908, déc. 2014.

[110] A.-C. Hladky-Hennion, J. O. Vasseur, G. Haw, C. Croënne, L. Haumesser et A. N. Norris, « Negative refraction of acoustic waves using a foam-like metallic structure », *Applied Physics Letters*, t. 102, n° 14, p. 144 103, avr. 2013.

[111] O. Oltulu, A. M. Mamedov et E. Ozbay, « Band gap structure of elliptic rods in water for a 2D phononic crystal », *Applied Physics A*, t. 123, n° 3, mar. 2017.

[112] H. Larabi, Y. Pennec, B. Djafari Rouhani et J. O. Vasseur, « Multicoaxial cylindrical inclusions in locally resonant phononic crystals », *Physical Review E*, t. 75, p. 066 601, 2007.

[113] Y. Chen et L. Wang, « Harnessing structural hierarchy to design stiff and lightweight phononic crystals », *Extreme Mechanics Letters*, t. 9, p. 91–96, déc. 2016.

[114] M. Torres, F. R. Montero de Espinosa et J. L. Aragón, « Ultrasonic wedges for elastic wave bending and splitting without requiring a full band gap », *Physical Review Letters*, t. 86, n° 19, p. 4282–4285, mai 2001.

[115] Y. Jin, N. Fernez, Y. Pennec, B. Bonello, R. P. Moiseyenko, S. Hémon, Y. Pan et B. Djafari-Rouhani, « Tunable waveguide and cavity in a phononic crystal plate by controlling whispering-gallery modes in hollow pillars », *Physical Review B*, t. 93, n° 5, fév. 2016.

[116] Y. Pennec, B. Djafari-Rouhani, J. O. Vasseur, H. Larabi, A. Khelif, A. Choujaa, S. Benchabane et V. Laude, « Acoustic channel drop tunneling in a phononic crystal », *Applied Physics Letters*, t. 87, n° 26, p. 261 912, déc. 2005.

[117] M. Maldovan et E. L. Thomas, « Simultanous localization of photons and phonons in two-dimensional periodic structures », *Applied Physics Letters*, t. 88, p. 251 907, 2006.

[118] S. Mohammadi, A. A. Eftekhar, A. Khelif et A. Adibi, « Simultaneous two-dimensional phononic and photonic band gaps in opto-mechanical crystal slabs », *Optics Express*, t. 18, p. 9164, 2010.

[119] Y. Pennec, B. Djafari Rouhani, E. H. El Boudouti, C. Li, Y. El Hassouani, J. O. Vasseur, N. Papanikolaou, S. Benchabane, V. Laude et A. Martinez, « Simultaneous existence of phononic and photonic band gaps in periodic crystal slabs », *Optics Express*, t. 18, p. 14 301, 2010.

[120] R. Lucklum, M. Zubtsov et A. Oseev, « Phoxonic crystals–a new platform for chemical and biochemical sensors », *Analytical and Bioanalytical Chemistry*, t. 405, p. 6497–6509, 2013.

[121] S. Amoudache, Y. Pennec, B. Djafari-Rouhani, A. Khater, R. Lucklum et T. Rachid, « Simultaneous sensing of light and sound velocities of fluids in a two-dimensional phoXonic crystal with defects », *Journal of Applied Physics*, t. 115, p. 134 503, 2014.

[122] K. Imamura et S. Tamura, « Negative refraction of phonons and acoustic lensing effect of a crystalline slab », *Physical Review B*, t. 70, p. 174 308, 2004.

[123] A. Sukhovich, L. Jing et J. H. Page, « Negative refraction and focusing of ultrasound in two- dimensional phononic crystals », *Physical Review B*, t. 77, p. 014 301, 2008.

[124] A. Sukhovich, B. Merheb, K. Muralidharan, J. O. Vasseur, Y. Pennec, P. A. Deymier et J. H. Page, « Experimental and theoretical evidence for subwavelength imaging in phononic crystals », *Physical Review Letters*, t. 102, p. 154 301, 2009.

[125] J. Bucay, E. Roussel, J. O. Vasseur, P. A. Deymier, A.-C. Hladky-Hennion, Y. Pennec, K. Muralidharan, B. Djafari Rouhani et B. Dubus, « Positive, negative, zero refraction, and beam splitting in a solid/air phononic crystal : theoretical and experimental study », *Physical Review B*, t. 79, p. 214 305, 2009.

[126] L.-Y. Zheng, Y. Wu, X. Ni, Z.-G. Chen, M.-H. Lu et Y.-F. Chen, « Acoustic cloaking by a near-zero-index phononic crystal », *Applied Physics Letters*, t. 104, n° 16, p. 161 904, avr. 2014.

[127] J. Zhao, B. Bonello, L. Becerra, O. Boyko et R. Marchal, « Focusing of Rayleigh waves with gradient-index phononic crystals », *Applied Physics Letters*, t. 108, n° 22, p. 221 905, mai 2016.

[128] S.-C. S. Lin et T. J. Huang, « Gradient-index phononic crystals », *Physical Review B*, t. 79, p. 094 302, 2009.

[129] A. Khelif, B. Aoubiza, S. Mohammadi, A. Adibi et V. Laude, « Complete band gaps in two-dimensional phononic crystal slabs », *Physical Review E*, t. 74, n° 4, oct. 2006.

[130] C. Goffaux et J. P. Vigneron, « Spatial trapping of acoustic waves in bubbly liquids », *Physica B : Condensed Matter*, t. 296, n° 1, p. 195–200, 2001.

[131] T.-W. Liu, Y.-C. Lin, Y.-C. Tsai, T. Ono, S. Tanaka et T.-T. Wu, « Evidence of a Love wave bandgap in a quartz substrate coated with a phononic thin layer », *Applied Physics Letters*, t. 104, n° 18, p. 181 905, mai 2014.

[132] Y. Liu, A. Talbi, P. Pernod et O. Bou Matar, « Highly confined Love waves modes by defect states in a holey SiO /quartz phononic crystal », *Journal of Applied Physics*, t. 124, p. 145 012, 2018.

[133] Y. Liu, A. Talbi, B. Djafari-Rouhani, E. H. El Boudouti, L. Drbohlavova, V. Mortet, O. Bou Matar et P. Pernod, « Interaction of Love waves with coupled cavity modes in a 2D holey phononic crystal », *Physics Letters A*, t. 383, p. 1502–1505, 2019.

[134] A. Khelif et A. Adibi, éds., *Phononic Crystals*. New York, NY : Springer New York, 2016.

[135] B. Bonello, C. Charles et F. Ganot, « Velocity of a SAW propagating in a 2D phononic crystal », *Ultrasonics*, t. 44, e1259–e1263, déc. 2006.

[136] M. Oudich, B. Djafari-Rouhani, B. Bonello, Y. Pennec, S. Hemaidia, F. Sarry et D. Beyssen, « Rayleigh Waves in Phononic Crystal Made of Multilayered Pillars : Con ned Modes, Fano Resonances, and Acoustically Induced Transparency », *Physical Review Applied*, t. 9, n° 3, p. 034 014, 2018.

[137] A. Khelif, Y. Achaoui et B. Aoubiza, « In-plane confinement and waveguiding of surface acoustic waves through line defects in pillars-based phononic crystal », *AIP Advances*, t. 1, n° 4, p. 041 404, déc. 2011.

[138] B. J. Ash, S. R. Worsfold, P. Vukusic et G. R. Nash, « A highly attenuating and frequency tailorable annular hole phononic crystal for surface acoustic waves », *Nature Communications*, t. 8, n° 1, déc. 2017.

[139] N. K. Kuo et P. G., « 1 GHZ phononic band gap structure in air/aluminum nitride for symmetric lamb waves », *2011 IEEE 24th International Conference on MEMS*, p. 740–743, 2011.

[140] ——, « Fractal phononic crystals in aluminum nitride : An approach to ultra high frequency bandgaps », *Applied Physics Letters*, t. 99, p. 163 501, 2011.

[141] N. K. Kuo, C. Zuo et P. G., « Microscale inverse acoustic band gap structure in aluminum nitride », *Applied Physics Letters*, t. 99, p. 093 501, 2009.

[142] Y. Pennec, B. Djafari-Rouhani, H. Larabi, J. O. Vasseur et A. C. Hladky-Hennion, « Low-frequency gaps in a phononic crystal constituted of cylindrical dots deposited on a thin homogeneous plate », *Physical Review B*, t. 78, p. 104 105, 2008.

[143] T.-T. Wu, T.-C. Huang et T.-C. Wu, « Evidence of complete band gap and resonances in a plate with periodic stubbed surface », *Applied Physics Letters*, t. 93, p. 111 902, 2008.

[144] O. R. Bilal et M. I. Hussein, « Trampoline metamaterial : Local resonance enhancement by springboards », *Applied Physics Letters*, t. 103, p. 111 901, 2013.

[145] T.-T. Wu, Y.-T. Chen, J.-H. Sun, S.-C. S. Lin et T. J. Huang, « Focusing of the lowest antisymmetric Lamb wave in a gradient-index phononic crystal plate », *Applied Physics Letters*, t. 98, n° 17, p. 171 911, avr. 2011.

[146] J. Zhao, B. Bonello et O. Boyko, « Focusing of the lowest-order antisymmetric Lamb mode behind a gradient-index acoustic metalens with local resonators », *Physical Review B*, t. 93, n° 17, mai 2016.

[147] G. Kovacs, G. W. Lubking, M. J. Vellekoop et A. Venema, « Love waves for *bio*chemical sensing in liquids », *IEEE 1992 Ultrasonics Symposium Proceedings*, p. 20–23, 1992.

[148] A. Kittmann, P. Durdaut, S. Zabel, J. Reermann, J. Schmalz, B. Spetzler, D. Meyners, N. Sun, J. McCord, M. Gerken, G. Schmidt, M. Höft, R. Knöchel, F. Faupel et E. Quandt, « Wide Band Low Noise Love Wave Magnetic Field Sensor System », *Scientific Reports*, t. 8, n° 1, p. 278–278, 2018.

[149] E. Gizeli, N. J. Goddard, C. R. Lowe et A. C. Stevenson, « A Love plate biosensor utilising a polymer layer », *Sensors and Actuators B*, t. 6, p. 131–137, 1992.

[150] M. Puiu, A.-M. Gurban, L. Rotariu, S. Brajnicov, C. Viespe et C. Bala, « Enhanced Sensitive Love Wave Surface Acoustic Wave Sensor Designed for Immunoassay Formats », *Ultrasonics*, t. 15, n° 5, p. 10 511–10 525, 2015.

[151] S.-Y. Chu, W. Water et J.-T. Liaw, « An investigation of the dependence of ZnO film on the sensitivity of Love mode sensor in ZnO/quartz structure », *Ultrasonics*, t. 41, p. 133–139, 2003.

[152] S. Trivedi et H. B. Nemade, « Simulation of a Love wave device with ZnO nanorods for high mass sensitivity », *Ultrasonics*, t. 84, p. 150–161, 2018.

[153] F.-M. Zhou, Z. Li, L. Fan, S.-Y. Zhang et X.-J. Shui, « Experimental study of Love-wave immunosensors based on ZnO/LiTaO3 structures », *Ultrasonics*, t. 50, n° 3, p. 411–415, 2010.

[154] J. C. Andle et J. F. Vetelino, *Sensors and Actuators A*, t. 44, p. 167–176, 1994.

[155] B. Jakoby, « Properties of love waves : applications in sensors », *Smart Materials and Structures*, t. 6, n° 6, p. 668–679, 1997.

[156] M. E. Korotyaeva, A. A. Kutsenko, A. L. Shuvalov et O. Poncelet, « Love waves in two-dimensional phononic crystals with depth-dependent properties », *Applied Physics Letters*, t. 103, n° 11, p. 111 902, sept. 2013.

[157] J. Bonhomme, M. Oudich, B. Djafari-Rouhani, F. Sarry, Y. Pennec, B. Bonello, D. Beyssen et P. G. Charette, « Love waves dispersion by phononic pillars for nano-particle mass sensing », *Applied Physics Letters*, t. 114, p. 013 501, 2019.

[158] Y. Ota, M. Shirane, M. Nomura, N. Kumagai, S. Ishida, S. Iwamoto, S. Yorozu et Y. Arakawa, « Vacuum Rabi splitting with a single quantum dot embedded in a photonic crystal nanocavity », *Applied Physics Letters*, t. 94, p. 033 102, 2009.

[159] Z. Wang, L. Shen, X. Zhang, Y. Wang, Z. Yu et X. Zheng, « Photonic crystal cavity with one-way rotating state and its coupling with photonic crystal waveguide », *Journal of Applied Physics*, t. 110, p. 043 106, 2011.

[160] R. Ohta, Y. Ota, M. Nomura, N. Kumagai, S. Ishida, S. Iwamoto et Y. Arakawa, « Strong coupling between a photonic crystal nanobeam cavity and a single quantum dot », *Applied Physics Letters*, t. 98, p. 173 104, 2011.

[161] M. A. Dundar, J. A. M. Voorbraak, R. Notzel, F. Andrea et R. W. van der Heijden, « Multimodal strong coupling of photonic crystal cavities of dissimilar size », *Applied Physics Letters*, t. 100, p. 081 107, 2012.

[162] J. H. Li, R. Yu et X. X. Yang, « Achieving slow and fast light with high transmission by nanodiamond nitrogen- vacancy center coupling to photonic crystal cavity », *Journal of Applied Physics*, t. 114, p. 124 312, 2013.

[163] Z. Shuang, D. A. Genov, Y. Wang, M. Liu et Z. Xiang, *Physical Review Letters*, t. 101, p. 047 401, 2008.

[164] N. Liu, L. Langguth, T. Weiss, J. Kastel, M. Fleischhauer, T. Pfau et H. Giessen, *Nature Materials*, t. 8, p. 758–762, 2009.

[165] Z. Han et S. I. Bozhevolnyi, *Opt. Express*, t. 19, n° 4, p. 3251–3257, fév. 2011.

[166] T. Faust, J. Rieger, M. J. Seitner, J. P. Kotthaus et E. M. Weig, « Coherent control of a classical nanomechanical two-level system », *Nature Physics*, t. 9, p. 485–488, 2013.

[167] H. Okamoto, A. Gourgout, C.-Y. Chang, K. Onomitsu, I. Mahboob, E. Y. Chang et H. Ymaguchi, « Coherent phonon manipulation in coupled mechanical resonantors », *Nature Physics*, t. 9, p. 480–484, 2013.

[168] A. Khelif, B. Djafari-Rouhani, J. O. Vasseur, P. A. Deymier, P. Lambin et L. Dobrzynski, « Transmittivity through straight and stublike waveguides in a two-dimensional phononic crystal », *Physical Review B*, t. 65, p. 174 308, 2002.

[169] J. H. Sun et T.-T. Wu, « Analyses of mode coupling in joined parallel phononic crystal waveguides », *Physical Review B*, t. 71, p. 174 303, 2005.

[170] Y.-F. Wang, V. Laude et Y.-S. Wang, « Coupling of evanescent and propagating guided modes in locally resonant phononic crystals », *Journal of Physics D : Applied Physics*, t. 47, p. 475 502, 2014.

[171] A. V. Korovin, Y. Pennec et B. Djafari Rouhani, « Strong coupling of phononic cavity modes in one-dimensional corrugated nanobeam structures », *Physical Review B*, t. 96, p. 184 302, 2017.

[172] T. Bagci, A. Simonsen, S. Schmid, L. G. Villanueva, E. Zeuthen, J. Appel, J. M. Taylor, A. Sorensen, K. Usami, A. Schliesser et E. S. Polzik, « Optical detection of radio waves through a nanomechanical transducer », *Nature*, t. 507, p. 81–85, 2014.

[173] I. Mahboob, N. Perrissin, K. Nishiguchi, D. Hatanaka, Y. Okazaki, A. Fujiwara et H. Yamaguchi, « Dispersive and dissipative coupling in a micromechanical resonator embedded with a nanomechanical resonator », *Nano Letters*, t. 15, n° 4, p. 2312–2317, 2015.

[174] H. J. R. Westra, M. Poot, H. S. J. van der Zant et W. J. Venstra, « Nonlinear modal interactions in clamped-clamped mechanical resonators », *Physical Review Letters*, t. 105, p. 117 205, 2010.

[175] J. Moser, A. Eichler, J. Guttinger, M. I. Dykman et A. Bachtold, « Nanotube mechanical resonators with quality factors of up to 5 million », *Nature Nanotechnology*, t. 24, n° 39, p. 395 702, 2014.

[176] I. Khivrich et S. Ilani, « Nanotubes resound better », *Nature Nanotechnology*, t. 9, p. 963–964, 2014.

[177] H. G. Craighead, « Nanoelectromechanical systems », *Science*, t. 290, n° 5496, p. 1532–1535, 2000.

[178] J. D. Teufel, T. Donner, D. Li, J. W. Harlow, M. S. Allman, K. Cicak, A. J. Sirois, J. D. Whittaker, K. W. Lehnert et R. W. Simmonds, « Sideband cooling of micromechanical motion to the quantum ground state », *Nature*, t. 475, p. 359–363, 2011.

[179] D. Hatanaka, I. Mahboob, K. Onomitsu et H. Yamaguchi, « Phonon waveguides for electromechanical circuits », *Nature Nanotechnology*, t. 9, p. 520–524, 2014.

[180] R. A. Jahdali et Y. Wu, « Coupled resonantors for sound trapping and absorption », *Science Report*, t. 8, p. 13 855, 2018.

[181] T. Faust, J. Rieher, M. J. Seitner, P. Krenn, J. P. Kotthaus et E. M. Weig, « Nanodiabatic dynamics of two strongly coupled nanomechanical resonator modes », *Physical Review Letters*, t. 109, p. 037 205, 2012.

[182] A. M. Eriksson, D. Midtvedt, A. Croy et A. Isacsson, « Frequency tuning, nonlinearities and mode coupling in circular mechanical graphene resonators », *Nanotechnology*, t. 105, 2013.

[183] Y. Jin, Y. Pennec et B. Djafari-Rouhani, *Journal of Physical D : Applied Physics*, t. 51, p. 494 004, 2018.

[184] J. Cha et C. Daraio, « Electrical tuning of elastic wave propagation in nanomechanical lattices at MHz frequencies », *Nature Nanotechnology*, t. 13, p. 1016–1020, 2018.

[185] G.-W. Deng, D. Zhu, X.-H. Wang, C.-l. Zou, J.-T. Wang, H.-O. Li, G. Cao, D. Liu, Y. Li, M. Xiao, G.-C. Guo, K.-L. Jiang, X.-C. Dai et G.-P. Guo, « Strongly coupled nanotube electormechanical resonators », *Nano Letters*, t. 16, n° 9, p. 5456–5462, 2016.

[186] G. Luo, Z.-Z. Zhang, G.-W. Deng, H.-O. Li, G. Cao, M. Xiao, G.-C. Guo, L. Tian et G.-P. Guo, « Strong indirect coupling between graphene-based mechanical resonators via a phonon cavity », *Nature Communications*, t. 9, p. 383, 2018.

[187] Y. Jin, E. H. El Boudouti, Y. Pennec et B. Djafari-Rouhani, « Tunable Fano resonances of Lamb modes in a pillared metasurface », *Journal of Physics D : Applied Physics*, t. 50, p. 425 304, 2017.

[188] M. Zhang, G. S. Wiederhecker, S. Manipatruni, A. Barnard, P. McEuen et L. Michal, « Synchronization of micromechanical oscillators using light », *Physical Review Letters*, t. 109, p. 233 906, 2012.

[189] M. Zhang, S. Shah, J. Cardennas et L. Michal, « Synchronization and phase noise reduction in micromechanical scillator arrays coupled through light », *Physical Review Letters*, t. 115, p. 163 902, 2015.

[190] M. Maldovan, « Sound and heat revolutions in phononics », *Nature*, t. 503, n° 7475, p. 209–217, nov. 2013.

[191] B. Liang, B. Yuan et J.-c. Cheng, « Acoustic diode : rectification of acoustic energy flux in one-dimensional systems », *Physical Review Letters*, t. 103, n° 10, sept. 2009.

[192] B. Li, « Acoustics : Now you hear me, now you don't », *Nature materials*, t. 9, n° 12, p. 962–963, 2010.

[193] N. Stenger, M. Wilhelm et M. Wegener, « Experiments on elastic cloaking in thin plates », *Physical Review Letters*, t. 108, n° 1, 2012.

[194] W. H. Bragg et W. L. Bragg, « The reflection of X-rays by crystals », *Proceedings of the Royal Society A*, t. 88, n° 605, p. 428–438, juil. 1913.

[195] P.-C. Li, Y. Zhao, A. Alu et E. T. Yu, *Applied Physics Letters*, t. 99, p. 221 106, 2011.

[196] N. Yu et F. Capasso, *Nature Materials*, t. 13, p. 139–150, 2014.

[197] Y. Jin, B. Bonello, R. P. Moiseyenko, Y. Pennec, O. Boyko et B. Djafari-Rouhani, *Physical Review B*, t. 96, n° 10, p. 104 311, 2017.

[198] M. Fleischhauer, A. Imamoglu et J. P. Marangos, « Electromagnetically induced transparency : Optics in coherent media », *Review of Modern Physics*, t. 77, p. 633–673, 2005.

[199] L. V. Hau, S. E. Harris, Z. Dutton et C. H. Behroozi, « Light speed reduction to 17 metres per second in an ultracold atomic gas », *Nature*, t. 397, p. 594–598, 1999.

[200] H. M. M. Alotaibi et B. C. Sanders, « Enhanced nonlinear susceptibility via double-double electromagnetically induced transparency », *Physical Review A*, t. 94, p. 053 832, 2016.

[201] G. Heinze, C. Hubrich et T. Halfmann, « Stopped light and image storage by electromagnetically induced transparency up to the regime of one minute », *Physical Review Letters*, t. 111, p. 033 601, 2013.

[202] S. H. Autler et C. H. Townes, « Stark effect in rapidly varying fields », *Physical Review Journal Archive*, t. 100, n° 2, p. 703, 1955.

[203] T. Y. Abi-Salloum, « Electromagnetically induced transparency and Autler-Townes splitting : Two similar but distinct phenomena in two categories of three-level atomic systems », *Physical Review A*, t. 81, p. 053 836, 2010.

[204] K. J. Boller, A. Imamoglu et H. S. E., « Observation of electromagnetically induced transparency », *Physical Review Letters*, t. 66, n° 20, p. 2593, 1991.

[205] B. Peng, S. K. Ozdemir, W. Chen, F. Nori et L. Yang, « What is and what is not electromagnetically induced transparency in whispering-gallery microcavities », *Nature Communications*, t. 5, p. 5082, 2014.

[206] Y.-C. Liu, B.-B. Li et Y.-F. Xiao, « Electromagnetically induced transparency in optical microcavities », *Nanophotonics*, t. 6, n° 5, p. 789–811, 2017.

[207] B. Wei et S. Jian, « Objectively discriminating the optical analogy of electromagnetically induced transparency from Autler-Townes splitting in a side coupled graphene-based waveguide system », *Journal of optics*, t. 19, n° 11, p. 115 001, 2017.

[208] C. Dong, V. Fiore, M. C. Kuzyk et H. Wang, « Optomechanical dark mode », *Science*, t. 21, n° 3, p. 1609–1613, 2012.

[209] A. H. Safavi-Naeini, T. P. Mayer Alegre, J. Chan, M. Eichenfield, M. Winger, Q. Lin, J. T. Hill, D. E. Chang et O. Painter, *Nature*, t. 472, p. 69–73, 2011.

[210] S. Weis, R. Riviere, S. Deleglise, E. Gavartin, O. Arcizet, A. Schliesser et T. J. Kippenberg, *Science*, t. 330, n° 3, p. 1520–1523, 2010.

[211] N. Liu, T. Weiss, M. Mesch, L. Langguth, U. Eigenthaler, M. Hirscher, C. Sonnichsen et H. Giessen, *Nano Letters*, t. 10, n° 4, p. 1103–1107, 2010.

[212] J. Gu, R. Singh, X. Liu, X. Zhang, Y. Ma, S. Zhang, S. A. Maier, Z. Tian, A. K. Azad, H.-T. Chen, A. J. Taylor, J. Han et W. Zhang, *Nature Communications*, t. 3, p. 1151, 2012.

[213] N. Papasimakis, V. A. Fedotov, N. I. Zheludev et S. L. Prosvirnin, *Physical Review Letters*, t. 101, p. 253 903, 2008.

[214] P. M. Anisimov, J. P. Dowling et B. C. Sanders, *Physical Review Letters*, t. 107, p. 163 604, 2011.

[215] H.-C. Sun, Y.-x. Liu, H. Lan, J. Q. You, E. Il'ichev et F. Nori, *Physical Review A*, t. 89, p. 063 822, 2014.

[216] J. Liu, H. Yang, C. Wang, K. Xu et J. Xiao, *Scientific Reports*, t. 6, p. 19 040, 2016.

[217] L. Giner, L. Veissier, B. Sparkes, A. Sheremet, A. Nicolas, O. Mishina, M. Scherman, S. Burks, I. Shomroni, D. V. Kupriyanov, P. Lam, G. E. et J. Laurat, *American Physical Society*, t. 87, n° 1, p. 013 823, 2013.

[218] C. Zhu, C. Tan et G. Huang, *Physical Review A*, t. 87, p. 043 813, 2013.

[219] C. Tan et G. Huang, *Physical Review A*, t. 31, n° 4, p. 704–715, 2014.

[220] Y. V. Radeonychev, M. D. Tokman, A. G. Litvak et O. Kocharovskaya, *Physical Review Letters*, t. 96, p. 093 602, 2006.

[221] F. Liu, M. Ke, A. Zhang, w. Wen, J. Shi, Z. Liu et P. Sheng, *Physical Review E*, t. 82, p. 026 601, 2010.

[222] A. Santillan et S. I. Bozhevolnyi, *Physical Review B*, t. 84, p. 064 304, 2011.

[223] M. Amin, A. Elayouch, M. Farhat, M. Addouche, A. Khelif et H. Bagci, *Journal of Applied Physics*, t. 118, p. 093 602, 2015.

[224] I. Quotane, E. H. El Boudouti et B. Djafari-Rouhani, *Physical Review B*, t. 97, p. 024 304, 2018.

[225] K. P. Burnham et D. R. Anderson, éds., *Model Selection and Multimodel Inference*, 2nd edition. Springer-Verlag, New York, 2002.

Etude de cristaux phononiques à base des matériaux micro/nano structurés pour la manipulation des ondes de Love

RESUME

Le contrôle de la propagation des ondes élastiques repose principalement sur la conception de milieu artificiel à base de matériaux structurés pour obtenir une ingénierie avancée de la dispersion de la propagation. Au cours de la thèse, la dispersion du mode guidé de polarisation transverse horizontale (mode de Love) dans la structure multi-couche SiO_2/Quartz (Coupe ST-90°) a été numériquement investiguée et les applications qui en découlent explorées. Il a été étudié les propriétés des cristaux phononiques à base de trous micro-usinés dans la couche de SiO_2, et également les mécanismes d'interaction de ce mode avec des plots déposés à la surface de cette couche guidante. Dans le cas des cristaux phononiques à base de trous nous avons montré qu'il est possible d'ouvrir des bandes interdites, cette propriété a été exploitée pour le design d'un résonateur cavité. Les performances des modes de ce résonateur sont étudiées en fonction des paramètres géométriques caractérisant le cristal phononique. Il est également proposé d'étudier l'interaction des modes du résonateur cavité avec les modes de résonances de plots déposés à la surface de la cavité. Les paramètres géométriques des plots sont choisis de manière à faire coïncider les modes de résonances des plots et de la cavité. Cela a pour effet un meilleur confinement des modes et donc une amélioration drastique du facteur de qualité des différents modes. On s'est intéressé aussi à l'interaction entre le mode Love et des méta-surfaces à base de plots déposés à la surface de SiO_2. Les couplages entre des plots de géométries identiques ou différentes ont donné lieu aux phénomènes divers comme analogue acoustique de Autler-Townes Splitting (ATS), résonance Fabry-Perot, modes de cavité, transparence induite acoustiquement (AIT) et résonance Fano. Les résultats présentés dans cette étude pourraient être utilisés pour des applications acoustiques potentielles telles que le traitement du signal, le contrôle des ondes, les méta-matériaux et les biocapteurs.

Mots-Clés:

- Ondes acoustiques de surface
- Cristaux phononiques
- Capteur
- Méta-surface
- MEMS
- Ondes de Love

Artificial micro-nano structured materials based phononic crystals for Love waves manipulation

ABSTRACT

The control of the propagation of elastic waves relies mainly on the design of artificial medium based on structured materials to obtain an advanced engineering of the dispersion of the propagation. During the thesis, the dispersion of the shear horizontal polarised guided mode (Love mode) in the multilayer SiO_2/Quartz structure (90ST-cut) was numerically investigated and the resulting applications were explored. The properties of phononic crystals based on micro-machined holes in the SiO_2 layer, as well as the interaction mechanisms of this mode with pillars deposited on the surface of this guiding layer, have been studied. In the case of hole-based phononic crystals we have shown that it is possible to open band gaps, this property has been exploited for the design of a cavity resonator. The performances of the modes of this resonator are studied according to the geometrical parameters characterizing the phononic crystal. It is also proposed to study the interaction of the modes of the cavity resonator with the resonance modes of pillars deposited on the surface of the cavity. The geometric parameters of the pillars are chosen so as to match the resonance modes of the pillars and the cavity. This has the effect of a better confinement of the modes and thus a drastic improvement of the quality factor of the different modes. We also investigated the interaction between the Love mode and meta-surfaces based on pillars deposited on the surface of SiO_2. The couplings between pillars of identical or different geometries gave rise to various phenomena like acoustic analogue of Autler-Townes Splitting (ATS), Fabry-Perot resonance, cavity modes, acoustically induced transparency (AIT) and Fano resonance. The results presented in this study could be used for potential acoustic applications such as signal processing, wave control, meta-materials and biosensors.

Keywords:

- Surface acoustic waves
- Phononic crystals
- Sensor
- Meta-surface
- MEMS
- Love waves